UNIVERSITÀ DEGLI STUDI DI PADOVA
Dipartimento di Fisica e Astronomia "Galileo Galilei"
Master Degree in Astrophysics and Cosmology

Final dissertation

How planetesimal accretion affects the composition of gas giants

External supervisor:
Dr. Bertram Bitsch
Internal supervisor:
Prof. Francesco Marzari

Candidate:
Claudia Danti
id: 1243539

Academic Year 2021/22

Contents

Abstract

The debate between the methods of pebble and planetesimal accretion for the formation of planets has yet to be resolved. Both of these scenarios have been looked into individually as a means for explaining planet formation, and now this work looks to combine them along with investigating distinguishing parameters between the scenarios.

The main aim of this work is to investigate the effect of planetesimal formation and accretion on the composition of gas giants, and possibly answer the question of whether the composition of a planet can constrain its formation pathway.

To do so, we perform semi-analytical 1D simulations of protoplanetary disks, including the treatment of viscous evolution and heating, pebble drift, and simple chemistry to simulate the growth of planets from planetary embryos to gas giants through pebble, planetesimal, and gas accretion as they migrate through the disk. The chemical composition of the planet's atmosphere is traced in order to look for parameters that may constrain its formation scenario.

Our simulation confirms, as presented in Schneider, Bitsch (2021), that the composition of the planetary gas atmosphere is dominated by the accretion of gas vapor that is enriched by inward drifting evaporating pebbles. Including planetesimal formation hinders this enhancement, as many pebbles are locked into planetesimals and cannot evaporate. This results in a dramatic drop of the accreted heavy elements both in the planetesimal formation and accretion case, demonstrating that planetesimal accretion needs to be inefficient in order to explain planets with high heavy element content. The pebble accretion scenario can explain super-solar C/H and O/H abundances, while the planetesimal formation and accretion scenarios present a general depletion of most of the elemental species. We observe a remarkable drop in the volatile-to-refractory ratio in the planetesimal accretion case, due to a large number of refractories being accreted through planetesimals, which may constrain the formation pathway of the planet.

In order to create planets with large heavy element contents, we need an inefficient planetesimal formation. The planetesimal accretion scenario shows a dramatic drop in the volatile-to-refractory ratio that can be used as a parameter to constrain the formation pathway. The C/O ratio of the planet's envelope alone cannot tell the scenarios apart.

Introduction

"Scientists are interested in the formation of planetary systems and so on, but for most, the majority of people, what is behind is the question of life. At the present time, this is the most exciting question we have facing us."

These are the words of Michel Mayor during his interview (Mayor, 2019) after being awarded the Nobel Prize in Physics on the 8 October 2019, for the discovery of the first exoplanet (Mayor, Queloz, 1995): 51 Pegasi b, a planet of $0.5 M_{\mathrm{J}}$ that orbits a solar-type star at 0.05 AU.

After more than 27 years since the first exoplanet's discovery, the interest in the field has only increased, as Queloz says (Queloz, 2019):

"There's something amazing in the field. The excitement for the field has never decreased from the beginning."

Indeed, as Mayor points out, the discovery of new worlds has always fascinated mankind,

"Greek philosophers were discussing the plurality of worlds and the possibility to have some of them inhabited 2000 years ago."

Despite having discovered more than 4000 exoplanets, the research field is now more active than ever, because, as Queloz affirms, we only scratched the surface when it comes to understanding the underlying physics behind planetary formation processes. In his Nobel Prize interview, he says

" [...]*we've still so much to learn. I mean, they're very little planets that look like the Earth right now and we're just barely trying to understand the planetary formation as a whole. And tomorrow there will be people addressing the question of the possible atmosphere content and evolution of the atmosphere, and one day, eventually, we'll be talking about life. And all this is as much exciting as detecting the first planet. And the detection of the first planet was the trigger of all this."*

The state-of-art theories on planet formation are divided into two main currents: Planet formation via pebble accretion and via planetesimal accretion.

Both the existence of pebbles and planetesimals are observation supported, the first were seen in protoplanetary disks by millimeter and centimeter wavelengths observations that show that micrometer-sized dust grains grow to pebble sizes around virtually all young stars (Tazzari, M. et al., 2016). The latter can be inferred by simply looking at our Solar System: the asteroids and Kuiper belt objects, and their debris disk counterparts around other stars (Wyatt, 2008), are all remnants of the planetesimals that are the starting seeds of planetary bodies.

Despite knowing that the solid dust particles dominate planet formation, we still lack a strong theoretical model able to explain it and its properties, such as the heavy element content or the C/O ratio. A large debate about whether all the possible types of observed planets can be formed using just one of the two formation scenarios (pebble or planetesimal accretion) is still ongoing.

The Planetesimal accretion scenario is based on the idea that the cores of the planet form by accretion of planetesimals and then subsequently undergo runaway gas accretion. This scenario has successfully been able to infer the core masses of the giant planets in the Solar System, but presents some main concerns that will prevent it to be able to reproduce other planets.

The Pebble accretion scenario, on the other hand, revolves around millimeter-to-centimeter-sized pebbles as the fundamental drivers of planetary growth. Pebbles are accreted by growing protoplanets much faster than planetesimals, resulting in planetary growth rates that are several orders of magnitude higher than even the most optimistic planetesimal accretion rates (Lambrechts, M., Johansen, A., 2012). The presence of pebbles in protoplanetary disks can also explain planetesimal formation, matching the 100-km-scale birth sizes of asteroids.

In order to try to solve this debate, several methods to constrain the planet formation based on the atmospheric composition have been developed (e.g., Mordasini et al. (2016) and Madhusudhan et al. (2017)). Of particular interest is the atmospheric C/O ratio, which seems to depend strongly on the formation pathway of the planet. Furthermore, if the mass and radius of the planet are known, one can also constrain the amount of heavy elements in the planet, if provided with an adequate interior model, such as the Thorngren et al. (2016) non-inflated model.

The up-to-date models for planetary formation generally include either planetesimal accretion (Mordasini, C. et al., 2012; Emsenhuber et al., 2021) or pebble accretion (Lambrechts, M., Johansen, A., 2012; Bitsch, Bertram et al., 2015), but usually lack a proper treatment of the chemical composition of the planet and the disk. These are the starting point of this work, whose aim is to try to contribute to the ongoing debate on the planet formation scenarios, by looking for a way to further constrain the formation pathway of a planet based on its composition.

Scope of the work

The scope of this work is to analyse the effects of planetesimal formation and accretion on the atmospheric composition of gas giants and possibly answer whether the atmospheric composition of a planet can constrain its formation pathway.

The work is divided as follows: The first chapter (c.f. Chapter 1) is devoted to providing a theoretical background about protoplanetary disks and planet formation while the second chapter (c.f. Chapter 2) presents the model used in this work and explains the operating principle behind the CHEMCOMP code used to preform the simulations. In the third chapter (c.f. Chapter 3), we present and comment our results, while in the fourth chapter (c.f. Chapter 4) we discuss the limitation of the model and possible future extensions. Finally, we end with conclusions, while in the appendices we discuss some of the parameters investigated during the work and we explain our choices.

Chapter 1

Theoretical background

This first chapter of this thesis is devoted to providing a theoretical background describing the environment in which planets form, i.e. protoplanetary disks, and the physical processes that lead to planet formation.

Planet formation occurs inside the protoplanetary disks, disks of gas and dust revolving around newly formed stars, during their first million years of life.

Star formation occurs inside giant molecular clouds, where clumps of cold material (mostly hydrogen and dust) gravitationally collapse into cores of typical dimensions of 0.1 pc and density $10^5 \mathrm{cm}^{-3}$. At the moment of collapse, these cores possess a rotational velocity, therefore the surrounding material has initial non-zero angular momentum and will fall into the core in a spiral motion that will result in the formation of a protoplanetary disk.

During the disk evolution, the angular momentum is redistributed outward on a longer timescale than the dynamical one, allowing the disk to survive. Protoplanetary disks inherit their mass and initial composition from the environment in which they are formed, whilst the evolution may also depend on external factors, such as radiation from close or passing by stars.

We will provide a theoretical overview of the gas and dust dynamics of the protoplanetary disk (Section 1.1) and then describe the mechanism of planet formation in the next Section 1.2.

1.1 Protoplanetary disk

Protoplanetary disks are made up of gas and dust in a ratio, called dust-to-gas ratio (ε) which is usually around $\approx 1/100$. Therefore, to describe the dynamical evolution of the disk we need to model the dynamical evolution of both the gas and the dust components. Figure 1.1 (Semenov, D. et al., 2010) depicts a section of a protoplanetary disk, showing the physical and chemical structure of the disk. The left section shows the dust in the

disk settling on the midplane, growing in size, and drifting towards the central star. The right section shows the temperature gradient increasing from the innermost part of the disk, which contains ice, to the outer part, that harbours complex molecules and rich chemistry.

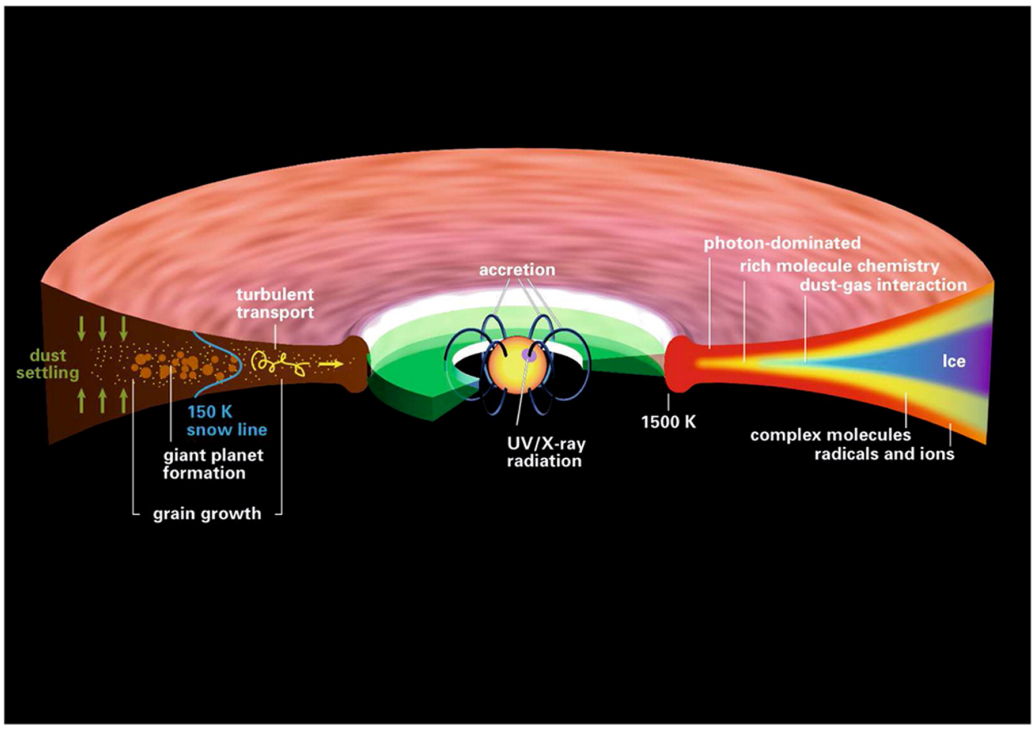

Figure 1.1: Sketch of the chemical and physical structure of a protoplanetary disk around a solar-type star (Henning, Semenov, 2013). The left section shows the physics of the dust settling, growth, and migration as well as the gas turbulent transport. The right side shows the increasing temperature gradient. The outer surfaces of the disk, irradiated by the star, has the highest temperature and harbours complex molecules and rich chemistry.

We will start discussing the gas evolution in this Subsection and move on to the dust evolution in the next Subsection.

1.1.1 Gas dynamics

The gas dynamics in the disk are described by means of Navier-Stokes equations, with some initial assumptions:

- **Thin disk**: the radius of the disk to be much bigger than its height $R/h \ll 1$, that allows us to consider the surface density Σ_{gas} instead of the volume density ρ_{gas} in

all our equations. The two quantities are related by:

$$\Sigma_{\text{gas}} = \int \rho_{\text{gas}} dz \tag{1.1}$$

- **Axis-symmetry**: symmetry under the rotation around the z-axis, this allows us to consider all the quantities as independent from the azimuthal coordinate ϕ. This leads to a natural choice of cylindrical coordinates (R, ϕ, z) centered in the newly formed star.

- **Evolution timescale is much bigger than dynamical timescale**: this implies that the radial velocity is much less than the azimuthal one ($v_{\text{gas,R}} \ll v_{\text{gas},\phi}$).

- **Disks are not self-gravitating**: namely, in the first evolutionary stages the mass of the disk is considered to be negligible with respect to the star's mass ($M_{\text{disk}} \ll M_*$), implying that the material in the disk is subjected to the stellar gravitational potential only.

By means of these assumptions we can write the continuity equation (1.2) and the Navier-Stokes equation (1.3), which becomes the Euler equation (1.4) in the case of a non-viscous fluid:

$$\frac{\partial \rho}{\partial t} + \nabla \cdot (\rho \mathbf{v}) = 0, \tag{1.2}$$

$$\frac{\partial \mathbf{v}}{\partial t} + (\mathbf{v} \cdot \nabla)\, \mathbf{v} = -\frac{1}{\rho}(\nabla P - \nabla \cdot \hat{\boldsymbol{\sigma}}) - \nabla \Phi, \tag{1.3}$$

$$\frac{\partial \mathbf{v}}{\partial t} + (\mathbf{v} \cdot \nabla)\, \mathbf{v} = -\frac{1}{\rho}\nabla P - \nabla \Phi, \tag{1.4}$$

with ρ volume density, $\mathbf{v}$ fluid velocity, P pressure, σ stress tensor and Φ gravitational potential given by Poisson equation:

$$\nabla^2 \Phi = 4\pi G \rho. \tag{1.5}$$

Disks are characterized by differential rotation, due to the fact that each fluid element has its own rotational velocity depending on its distance from the central star. When these rings interact with each other (e.g., thermal chaotic motion of molecules or turbulent motion) the viscous stress generates an exchange of angular momentum between the faster and the slower rotating material.

Analysing the Navier-Stokes equations per component we can gain information about the dynamical evolution of the disk, therefore we will proceed to separately study the vertical, azimuthal, and radial components of the equations.

Vertical component: hydrostatical equilibrium

When we only consider the vertical component of the Euler equation (1.4), the only non-zero component reduces to the hydrostatic equilibrium equation between the gravitational attraction provided by the star and the pressure gradient of the gas in the vertical direction:

$$\frac{1}{\rho}\frac{\partial P}{\partial z} = -\frac{\partial \Phi}{\partial z}. \tag{1.6}$$

If we consider a thin disk, calling h the height of the disk, we can rewrite equation (1.6) as:

$$\frac{\partial \Phi}{\partial z} = g_z = g\sin\theta = \frac{GM_* z}{(R^2+z^2)\,(R^2+z^2)^{\frac{1}{2}}}, \tag{1.7}$$

with R distance between the gas element and the star, z vertical distance of the gas element from the midplane and θ the angle between these two directions, as sketched in Figure 1.2

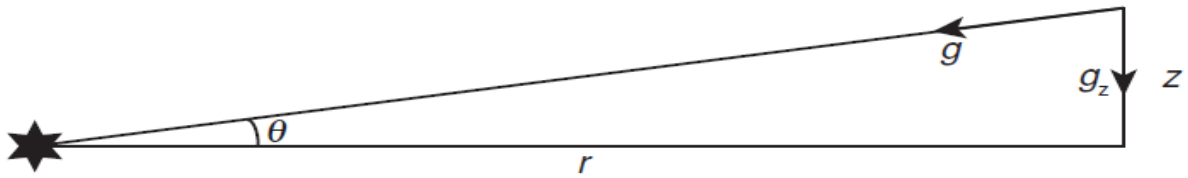

Figure 1.2: Sketch of the gravitational attraction exerted by the star on a gas element in the disk (Armitage, 2013).

Radial component: azimuthal velocity

In this case, we are going to assume the radial velocity to be much smaller than the azimuthal one ($v_{\mathrm{gas},R} \ll v_{\mathrm{gas},\Phi}$), due to the differences in the evolutionary and dynamical timescales. We can estimate the azimuthal velocity of the gas starting from the radial component of the Euler equation (1.4) considering axisymmetry and the gravitational potential to be dominated by the star's gravity:

$$\frac{v^2_{\mathrm{gas},\Phi}}{R} = \frac{\partial \Phi}{\partial R} + \frac{1}{\rho}\frac{\partial P}{\partial R} = \frac{GM_*}{R^2} + \frac{1}{\rho}\frac{dP}{dR}. \tag{1.8}$$

We observe that the term $\mathrm{d}P/\mathrm{d}R < 0$, because the pressure decreases going outward, thus the actual value of the azimuthal velocity of the gas will be sub-Keplerian. By assuming a power-law to describe the pressure gradient:

$$P = P_0\left(\frac{R}{R_0}\right)^{-n} = \rho_0 c_s^2\left(\frac{R}{R_0}\right)^{-n}, \tag{1.9}$$

where P_0 is the pressure at a fixed distance R_0, we can express the azimuthal velocity as:

$$v_{\mathrm{gas},\Phi} = v_k \left(1 - \frac{nc_s^2}{v_k^2}\right)^{1/2} = v_k \left(1 - \frac{nh^2}{R^2}\right)^{1/2}. \tag{1.10}$$

Equation (1.10) clearly shows that the azimuthal velocity is sub-Keplerian up to an order $O(h/R)^2$, which turns out to be a small quantity for thin disks. The reason for this is that the orbit of the gas is pressure supported, thus it does not need Keplerian speed in order to maintain a stable orbit. This difference in velocity is negligible when considering just the gas dynamics, but becomes fundamental when analysing the motion of solid bodies inside the disk.

Azimuthal component: conservation of angular momentum

The azimuthal component of Navier-Stokes equation contains information about the conservation of angular momentum. Neglecting the vertical component of the velocity, we can rewrite the continuity equation (1.2) as:

$$\frac{\partial \Sigma}{\partial t} + \frac{1}{R}\frac{\partial \left(R\Sigma v_{\mathrm{gas},R}\right)}{\partial R} = 0, \tag{1.11}$$

with $v_{\mathrm{gas},R}$ radial velocity of the gas. By defining the mean kinematic viscosity as the integral in the vertical direction of the viscosity coefficient η:

$$\nu\Sigma \equiv \int_{-\infty}^{+\infty} \eta \, dz, \tag{1.12}$$

we can evaluate the stress-energy tensor of Navier-Stokes equation (1.3), whose only non-zero component is:

$$T_{R,\Phi} = \nu\Sigma R \frac{\partial \Omega}{\partial R}. \tag{1.13}$$

Pressure and gravitational potential do not give contributions to the Navier-Stokes equation due to the symmetry of the problem, thus, the azimuthal component of equation (1.3) integrated in the vertical direction is given by:

$$\Sigma \left(\frac{\partial v_{\mathrm{gas},\Phi}}{\partial t} + v_{\mathrm{gas},R}\left(\frac{v_{\mathrm{gas},\Phi}}{R} + \frac{\partial v_{\mathrm{gas},\Phi}}{\partial R}\right)\right) = \nabla \cdot T|_{\Phi}. \tag{1.14}$$

Multiplying both sides by R and using the continuity equation (1.2) we obtain the conservation of angular momentum:

$$\frac{\partial \left(\Sigma R v_{\mathrm{gas},\Phi}\right)}{\partial t} + \frac{1}{R}\frac{\partial \left(v_{\mathrm{gas},R}\Sigma R^2 v_{\mathrm{gas},\Phi}\right)}{\partial R} = \frac{1}{R}\frac{\partial \left(\nu\Sigma R^3 \frac{\partial \Omega}{\partial R}\right)}{\partial R}. \tag{1.15}$$

We observe that the left-hand side of the equation represents the Lagrangian derivative of the angular momentum per unit area $\Sigma R v_{\mathrm{gas},\Phi}$ of a ring at distance R from the protostar. In particular, the second term of the left-hand side accounts for the loss of angular momentum due to the material accreting onto the star. The right-hand side represents, instead, the mechanical moment due to viscous forces. If we multiply this term by $2\pi R dR$ we obtain the torque of a ring dR. Thus, the flux of angular momentum from a ring at distance R is given by:

$$G(R) = 2\pi R^2 T_{R,\Phi} = 2\pi\nu\Sigma R^3 \frac{\partial\Omega}{\partial R}, \tag{1.16}$$

where the positive sign of the torque $G(R)$ is a convention to describe the flux towards the inner part of the disk. For solids, $G(R) = 0$ since the shear viscosity does not act on rotating solids. If the flowing material orbits with Keplerian velocity, the angular momentum is transported from the inside towards the outside part of the disk, with a torque given by:

$$G\left(R\right) = -3\pi\nu\Sigma R^2\Omega_k. \tag{1.17}$$

Surface density evolution

By combining the continuity equation[1] (1.2) expressed as a function of the surface density Σ with the Navier-Stokes equation[2] (1.3) we get an equation that describes the temporal evolution of the surface density (Armitage, 2013; Pringle, 1981):

$$\frac{\partial\Sigma_{\mathrm{gas,Y}}}{\partial t} - \frac{3}{R}\frac{\partial}{\partial R}\left(\sqrt{R}\frac{\partial}{\partial R}\left(\nu\Sigma\sqrt{R}\right)\right) = \dot{\Sigma}_{\mathrm{Y}}. \tag{1.18}$$

where with Y we denote all the possible chemical species present in the disk[3] and $\dot{\Sigma}_{\mathrm{Y}}$ is a source term for each species Y. If we define the following quantities:

$$X = 2R^{1/2}, \tag{1.19}$$

$$f = \frac{3}{2}\Sigma X, \tag{1.20}$$

we can rewrite equation (1.18) as:

$$\frac{\partial f}{\partial t} = D\frac{\partial^2 f}{\partial X^2} + \dot{\Sigma}_{\mathrm{Y}}, \tag{1.21}$$

with the diffusion coefficient $D = 12\nu/X^2$, this clearly shows that equation (1.18) is a diffusion equation.

[1] That expresses the mass conservation.
[2] That expresses the conservation of angular momentum.
[3] We will treat this aspect in more detail in the next chapter.

Without the source term[4] there are different possible analytical solutions, such as the *self-similar solution*, found by Lynden-Bell, Pringle (1974), that is the one used in our modeling to initialize the simulations. The analytical expression of the self-similar solution according to Lodato et al. (2017), is:

$$\Sigma_{\rm gas}(R,t) = \frac{M_0}{2\pi R_0^2}(2-\psi)\left(\frac{R}{R_0}\right)^{-\psi} \xi^{-(5/2-\psi)/(2-\psi)} \exp\left[-\frac{\left(\frac{R}{R_0}\right)^{2-\psi}}{\xi}\right], \tag{1.22}$$

with $\psi = \left(\frac{d\ln\nu}{d\ln R}\right)_{R=R_{\rm in}} \approx 1.08$, and $\xi = 1 + \frac{t}{\tau_\nu}$, where the viscous time is given by:

$$\tau_\nu = \frac{1}{3\,(2-\psi)^2}\frac{R_0^2}{\nu(R_0)} \tag{1.23}$$

This solution is particularly suited to get the disk viscosity and the viscous timescale τ_ν.

Figure 1.3 shows the gas surface density as a function of radius for different time snapshot in the case of the self-similar solution.

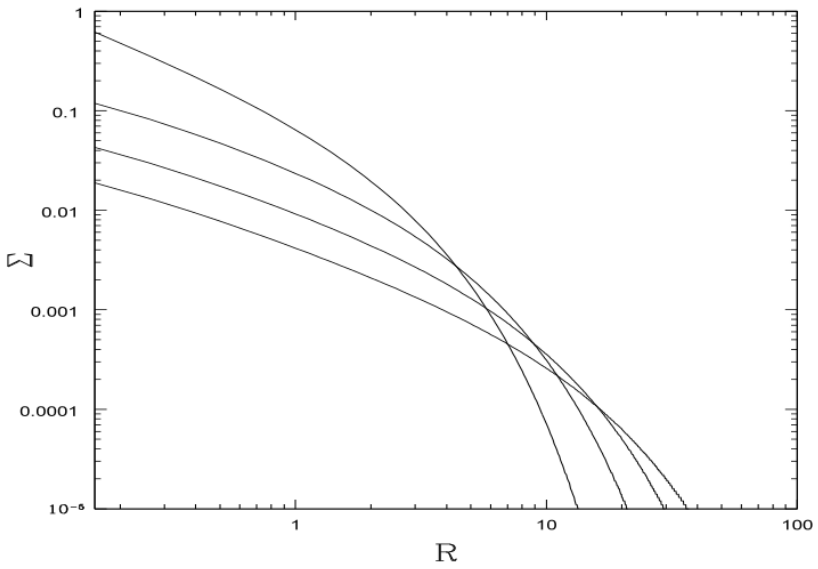

Figure 1.3: Time evolution of the gas surface density Σ as a function of radius R for the *self-similar solution* (1.22) for b = 1 (Lodato, 2008). From the uppermost line to the bottom one the time steps are $T = 1, 2, 4, 7$ with arbitrary units.

[4]i.e. setting the RHS of the equation to zero

Viscosity

Viscosity is a very important parameter in disk evolution as it is responsible for the angular momentum distribution. We will describe the disk as an ensemble of molecules, thus it would be natural to assume that the viscosity is given by the molecular collisions, namely $\nu \approx \lambda c_s$, with λ mean free path of the molecule and c_s speed of sound. However, if we estimate the viscous timescale using this prescription, we obtain $\tau_\nu \approx 3 \cdot 10^{13}$, which is a value that is definitely bigger than the observed timescale. We must therefore conclude that the molecular viscosity is not responsible for the angular momentum distribution.

The *Reynolds number* for a fluid is defined as:

$$\mathrm{Re} = \frac{v_{\mathrm{rel}} L}{\nu}, \tag{1.24}$$

with v_{rel} relative velocity between the fluid and the object and L linear dimension of the object. This number is the ratio of inertial forces to viscous forces and gives an idea of the type of flow regime that the fluid is in. Low Reynolds numbers correspond to viscous forces dominating, and characterize a smooth, constant fluid motion (laminar flow), while high Reynolds number describe a motion dominated by inertial forces, which tend to produce chaotic eddies, vortices and other flow instabilities (turbulent flow).

A small molecular viscosity implies a high Reynolds number for the fluid, that is the description of a turbulent fluid, which is the actual mechanism that distributes angular momentum. In the case of an isotropically turbulent fluid, the turbulence spatial scale is the disk height h. The simplest way to model the turbulent viscosity is to use the alpha-viscosity prescription of Shakura, Sunyaev (1973), in which the viscosity is directly proportional to the vertical height of the disk h and the isothermal speed of sound c_s[5]:

$$\nu = \alpha_t c_s h \tag{1.26}$$

where α_t is the so-called Shakura-Sunyaev parameter, a dimensionless factor that describes the turbulence in the disk.

1.1.2 Dust dynamics

The dust accounts for only around 1% of the total mass of the disk, however, it is a key ingredient for planetary formation. Furthermore, it is responsible for most of the thermal

[5]The isothermal speed of sound can be linked to the midplane temperature by means of:

$$c_s = \sqrt{\frac{k_B T}{\mu m_p}}, \tag{1.25}$$

with μ mean molecular weight that can change due to the enrichment of the disk's gas with vapor and m_p proton mass

emission that we observe in the disk, and, being very sensitive to the changes in the gas dynamics, it can conveniently be used to trace gas dynamics.

Dust is mathematically described as a continuum, i.e. an ensemble of particles whose macroscopic properties can be obtained by averaging over a volume big enough to be statistically relevant but small enough for the fluid variations to be neglected. To treat dust as a continuum we need to assume that it is a pressure-less fluid, assumption which is supported by the fact that the collision frequency between dust particles is negligible with respect to the collisions between gas and dust particles. Furthermore, it will be treated as a fluid with zero viscosity since the collisions between particles are negligible in the Epstein regime (that is the dominant regime in protoplanetary disks). Finally we also add the homogeneous, non viscous, and charge-less hypotheses, and we specify that dust dynamics are regulated only by the gravitational field of the central star.

In this Section we will first describe the areodynamical coupling between gas and dust, then proceed to describe dust dynamics in the case of laminar flow and finally analyse the case of turbulent flows, as a correction to the previously treated laminar flow equations.

Aerodynamical dust-gas coupling

Let us start by describing the dynamics of a dust particle embedded in a gas disk. We will consider the particle to be a non-charged sphere with fixed radius a, density ρ_d and mass $m_\mathrm{d} = \frac{4}{3}\pi\rho_\mathrm{d}a^3$, that moves with a relative velocity:

$$v_\mathrm{rel} = v_\mathrm{dust} - v_\mathrm{gas}, \tag{1.27}$$

inside the disk. Aerodynamical forces will always try to damp the velocity difference between gas and dust and the timescale required to achieve this depends on the disk and fluid properties. To quantify the force that acts on the dust particles we need a way to describe how much dust and gas are coupled with each other. In particular we identify two different regimes:

- **Epstein regime**: a dust particle is in the Epstein regime when the particle dimension is smaller than the mean free path[6] of a gas element ($a < 9\lambda_\mathrm{mfp}/4$), meaning that the dust sees the gas as an ensemble of collisionless molecules with a Maxwellian velocity distribution, as sketched in the upper panel of Figure 1.4. In this case, we can compute the fluidodynamical force starting from the angular momentum transfer from the gas elements to the dust particles, obtaining:

$$F_D = -\frac{4}{3}\pi f a^2 \rho_\mathrm{gas} v_\mathrm{th} \mathbf{v}_\mathrm{rel}, \tag{1.29}$$

[6]We define the mean free path of the gas element as:

$$\lambda_\mathrm{mfp} = \frac{\mu m_p}{\rho_\mathrm{gas}\sigma_\mathrm{coll}}, \tag{1.28}$$

with μ mean molecular weight, ρ_gas gas volume density and σ_coll cross-section.

where $4\pi a^2 \mathbf{v}_{\rm rel}$ is the volume travelled per unit time and $\rho_{\rm gas} v_{\rm th}$ the momentum per unit volume. $f = \sqrt{1 + \frac{9\pi}{128}\left(\frac{v_{\rm rel}}{c_s}\right)^2}$ is a correction factor that is relevant if the relative motion between dust and gas is supersonic, otherwise is approximately 1 (as for in the protoplanetary disks).

- **Stokes regime**: a dust particle is in the Stokes regime when the particle's dimension is bigger than the gas mean free path ($a > 9\lambda_{\rm mfp}/4$), thus the gas flows around the dust as a continuum, as shown in the bottom panel of figure 1.4. This flow can be either laminar or turbulent. Depending on the value of the Reynolds number three different Stokes regimes are possible. In this case the aerodynamical drag will be expressed by:

$$F_D = \frac{C_D}{2}\pi a^2 \rho_{\rm gas} |v_{\rm rel}| v_{\rm rel}, \tag{1.30}$$

with C_D drag coefficient, that assumes different values[7] depending on the Stokes regime that is considered.

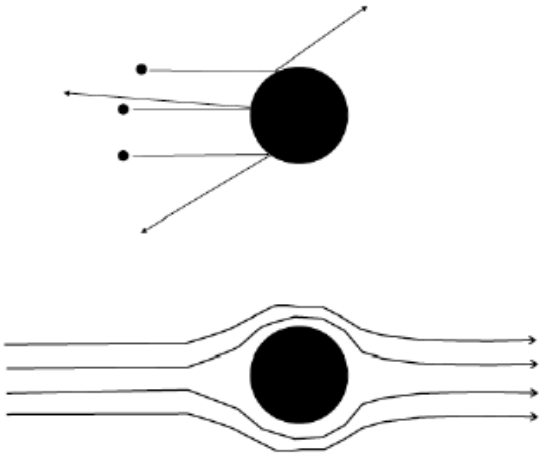

Figure 1.4: Areodynamical interaction between gas and dust in the Epstein (upper panel) and Stokes (lower panel) regime (Dipierro et al., 2016).

[7] $C_D = \begin{cases} 24\mathrm{Re}^{-1} & \text{per Re} < 1, \text{ Stokes I,} \\ 24\mathrm{Re}^{-0,6} & \text{per } 1 < \text{Re} < 800, \text{ Stokes II,} \\ 0,44 & \text{per Re} > 800, \text{ Stokes III.} \end{cases}$

Stokes number

A very important parameter to describe the dust dynamical evolution is the Stokes number, which quantifies the coupling between dust particles and gas, i.e., whether the dust dynamically evolves coupled, decoupled, or partially coupled with the gas.

To define the Stokes number we first need to describe two important timescales for dust dynamics:

- **Stopping timescale**: Describes the coupling of the dust particles with the non-perturbed orbital gas flow

$$\tau_s = t_s \Omega_k, \tag{1.31}$$

with Ω_k Keplerian frequency and

$$t_s = \frac{m_p \left|\mathbf{v}_{\mathrm{rel}}\right|}{\left|\mathbf{F}_D\right|} = \frac{m_p}{K}. \tag{1.32}$$

stopping time, that describes the timescale in which the areodynamical drag[8] significantly modifies the relative velocity between gas and dust. In other words how long does it take to the gas to remove angular momentum from the dust grain. in the Epstein and Stokes I regime, since the force scales $\propto v_{\mathrm{rel}}$ the stopping time is considered to be the time interval in which the velocities that scale exponentially are reduced by a factor e. It can be shown that, in every regime, the stopping time increases as the size of the particle increases $t_s \propto a^r$ with $1 \leq r \leq 2$, with the maximum in the Stokes I regime. This demonstrates that the bigger grains decouple from the gas.

- **Eddies evolution timescale**: describes the effect of the orbital shear on turbulent eddies

$$\tau_e = t_e \Omega_k, \tag{1.34}$$

with Ω_k Keplerian frequency and t_e eddy timescale (is the correlation time between the turbulent fluctuations).

We can finally define the Stokes number as:

$$\mathrm{St} = \frac{t_s}{t_e} = \frac{\tau_s}{\tau_e}, \tag{1.35}$$

[8] We used the most general expression for the areodynamical drag:

$$F_D = -K v_{\mathrm{rel}}, \tag{1.33}$$

where K is a parameter that in the Epstein e Stokes I regimes is v_{rel} independent, leaving a linear dependence of F_D on v_{rel}. In protoplanetary disks the density values involves make us fall in the Epstein or at maximum Stokes I regime.

Since the number entirely describes the areodynamical properties of dust, particles with different sizes, shapes or compositions that have the same Stokes number are areodynamically identical. Assuming $\tau_e = 1$ we can rewrite equation (1.35) as:

$$\mathrm{St} = \tau_s = t_s \Omega_k = \frac{\pi}{2} \frac{a \rho_\mathrm{d}}{\Sigma_\mathrm{gas}}, \tag{1.36}$$

with a and ρ_d radius and density of the dust particle. Small Stokes numbers ($\mathrm{St} \ll 1$) describe dust particles that are strongly coupled with the gas, whose dynamics becomes indistinguishable from the gas one, while bigger Stokes numbers ($\mathrm{St} \gg 1$) describe poorly coupled particles, whose dynamics is almost independent from the gas one. Finally, intermediate Stokes numbers 1 ($\mathrm{St} \approx 1$) describe the partially coupled particles, which is the regime in which the gas-dust interaction mostly modifies dust evolution.

Dust dynamics in laminar flows

Considering dust as a fluid, thus taking the two-fluid approach to describe the protoplanetary disk, we can model the dust dynamics in laminar flows using again Navier-Stokes equations. We will consider laminar flows, which are flows in which the motion of the fluid is described by layers that flow one over the other without mixing or causing turbulence, therefore viscosity-dominated flows.

The equations[9] that describe this two-fluid system are:

$$\frac{\partial \rho_\mathrm{dust}}{\partial t} + \nabla \cdot (\rho_\mathrm{dust} \mathbf{v}_\mathrm{dust}) = 0, \tag{1.37}$$

$$\frac{\partial \mathbf{v}_\mathrm{dust}}{\partial t} + (\mathbf{v}_\mathrm{dust} \cdot \nabla) \mathbf{v}_\mathrm{dust} = -\frac{1}{\rho_\mathrm{dust}} F_D^V - \nabla \Phi, \tag{1.38}$$

with

$$F_D^V = -K^V (\mathbf{v}_\mathrm{dust} - \mathbf{v}_\mathrm{gas}) = \frac{\rho_\mathrm{dust}}{m_p} K (\mathbf{v}_\mathrm{dust} - \mathbf{v}_\mathrm{gas}) \tag{1.39}$$

drag force.[10] We will now proceed as we did in the gas case and analyse separately the radial, azimuthal and vertical components of these equations.

[9] continuity and Navier-Stokes for dust

[10] the apex V shows that we are considering a force per unit volume:

$$F_D^V = K \frac{\rho_\mathrm{dust}}{m_p}. \tag{1.40}$$

Radial drift in laminar flows To analyse the radial component of equation (1.38) we first need the non-zero components of the stress-energy tensor $\hat{\boldsymbol{\sigma}}$, that will be the shear viscosity [11]. The radial component of equation (1.38), therefore, yields:

$$\frac{dv_{\mathrm{dust},R}}{dt} - \frac{v_{\mathrm{dust},\Phi}^2}{R} = -\frac{1}{t_\mathrm{s}}\left(v_{\mathrm{dust},R} - v_{\mathrm{gas},R}\right) - \Omega_k^2 R, \tag{1.41}$$

where Ω_k, non-perturbed gas Keplerian frequency, can be obtained from equation (1.10). We now perform a Taylor expansion of order one in the Keplerian velocity and consider only stationary solutions ($\partial/\partial t = 0$), getting as an expression for the perturbed radial velocity of the dust:

$$\frac{dv_{\mathrm{dust},R}}{dt} = -\frac{1}{t_\mathrm{s}}\left(v_{\mathrm{dust},R} - v_{\mathrm{gas},R}\right) + 2\Omega_k v_{\mathrm{dust},\Phi} = 0 \tag{1.42}$$

The time scale that the two-fluid system needs to reach stationary equilibrium, assuming the mass component of the dust is negligible with respect to the one of the gas, is $t_{\mathrm{s,mix}} \approx t_s$. This shows that t_s is a good approximation if one of the two fluids has a negligible density with respect to the other, but fails if the densities are of the same order. Therefore, considering the dust mass negligible with respect to the gas mass, the radial drift equation for the dust grains yields:

$$v_{\mathrm{dust},R} = \left(\frac{R v_{\mathrm{gas,R}}/v_k t_\mathrm{s} - n c_\mathrm{s}^2/v_k}{v_k t_\mathrm{s}/R + R t_\mathrm{s}/v_k}\right), \tag{1.43}$$

or, in terms of τ_s:

$$v_{\mathrm{dust,R}} = \left(\frac{v_{\mathrm{gas,R}}/\tau_s - n c_\mathrm{s}^2 v_k}{\tau_s + 1/\tau_s}\right). \tag{1.44}$$

Azimuthal drift in laminar flows The azimuthal component of equation (1.38) yields:

$$\frac{dv_{\mathrm{dust},\Phi}}{dt} + v_{\mathrm{dust},R}\left(\frac{v_{\mathrm{dust},\Phi}}{R} + \frac{dv_{\mathrm{dust},\Phi}}{dR}\right) = -\frac{R}{t_\mathrm{s}}\left(v_{\mathrm{dust},\phi} - v_{\mathrm{gas},\Phi}\right) \tag{1.45}$$

and again, Taylor expanding in the Keplerian velocity at order one and considering stationary solutions we obtain:

$$\frac{\partial v_{\mathrm{dust},\Phi}}{\partial t} = -\frac{K^V}{\rho_\mathrm{dust}}\left(v_{\mathrm{dust},\Phi} - v_{\mathrm{gas},\Phi}\right) - \frac{\Omega_k}{2} v_{\mathrm{dust},R} = 0, \tag{1.46}$$

that has a stationary solution:

$$v_{\mathrm{dust},\Phi} = -\frac{1}{2}\left(\frac{t_\mathrm{s} v_{\mathrm{dust,R}} v_k}{R} - v_{\mathrm{gas},\Phi}\right). \tag{1.47}$$

[11] $\sigma_{R,\phi} = \eta R \frac{\partial}{\partial R}\left(\frac{v_{\mathrm{gas},\phi}}{R}\right)$, where we approximate $v_{\mathrm{gas},\phi} = v_k$ since the correction is of the order $O\left(\frac{h}{R}\right)^2$.

Vertical settling in laminar flows There is a huge difference in the timescale of the radial and vertical motion for the dust, indeed the vertical timescale is much shorter and leads to dust settling on the midplane. Provided that, we can infer the vertical settling neglecting the radial drift (thus considering the two processes as independent):

$$\frac{t_{\text{settling}}}{t_{\text{drift}}} \cong \left(\frac{h_{\text{g}}}{R}\right)^2 \ll 1. \tag{1.48}$$

We expect the vertical settling to divide the grains based on their size (in particular the radius), due to the radius dependence of aerodynamical and gravitational forces. Assuming small dust-to-gas ratio $\varepsilon \ll 1$, the vertical settling is given by Langevin equation:

$$\frac{\partial v_{\text{dust},z}}{\partial t} = -\Omega_k^2 z + \frac{v_{\text{gas},z} - v_{\text{dust},z}}{t_s}. \tag{1.49}$$

This equation describes a stocastically damped forced oscillator, due to turbulences: stochasticity is included in the term $v_{\text{gas},z}/t_s$, where $v_{\text{gas},z}$ is the vertical component of the gas velocity that casually fluctuates due to turbulence. If we assume the flux to be stationary, ($v_{\text{gas},z} = 0$), the equation of motion of the dust becomes the damped harmonic oscillator:

$$\frac{\partial^2 z}{\partial t^2} + \frac{\Gamma \partial \text{z}}{\partial t} + \Omega_k^2 z = 0, \tag{1.50}$$

where we defined $v_{\text{dust},z} = \frac{\partial z}{\partial t}$, $\Gamma = \frac{1}{t_s} = \frac{\Omega_k}{\text{St}}$.

Close to the midplane, where the gas density can be assumed constant along the vertical direction, equation (1.50) has a solution of the type:

$$z\,(t) = e^{pt} \tag{1.51}$$

with the following values of p:

$$p^{\pm} = \frac{1}{2}\left(-\Gamma \pm \sqrt{\Gamma^2 - 4\Omega_k^2}\right). \tag{1.52}$$

where the term $\sqrt{\Gamma^2 - 4\Omega_k^2}$ can be either positive, negative or zero, depending on the value of the Stokes number. Therefore, dust grain have different settling times depending on the size:

- Small grains have settling times $\cong 1/\text{St}$.
- Big grains have settling times $\cong$ St The fastest settling time ($1/\Omega_k$) occurs for $\text{St} = 0.5$.

If we consider all the possible cases, we can summarize the settling time as:

$$\Omega_k t_{\text{settling}} \cong \text{St} + \frac{1}{\text{St}}, \tag{1.53}$$

If we assume the disk to be vertically in hydrostatic equilibrium, we can write the Stokes number as a function of z:

$$\text{St} = \frac{\rho_p a}{\Sigma_{\text{gas}}} \frac{\pi}{2} \sqrt{\psi} \ \exp\left[\frac{z^2}{2h_g^2}\right] = \text{St}_0 \ \exp\left[\frac{z^2}{2h_g^2}\right]. \tag{1.54}$$

with h_g gas scale height. From equation (1.54) we notice that highly coupled particles in the midplane are poorly coupled in the upper layers of the disk. As the dust settles down to the midplane its Stokes number decreases due to the higher value of gas density. For this reason, grains that do not grow during the settling are decelerate, whilst grains that are able to grow can partially counter-balance the higher gas density, potentially maintaining a big enough Stokes number that allows planetesimal formation.

The dynamics of dust

We now aim to summarize the dynamics of the dust component of the disk. We start comparing the azimuthal and radial velocities of gas and dust, which are different due to the different nature of the two fluids:

- The gas feels pressure and viscous forces that allow it to orbit at sub-Keplerian velocity around the protostar.
- The dust is not pressure supported, it only feels the gravitational attraction from the central star, thus the orbital motion is Keplerian.

The final effect is the dust feeling a "contrary gas wind" in the azimuthal direction[12], that causes the dust to lose angular momentum and spiral inward (this motion is known as *radial drift*) and a lateral wind in the radial direction caused by the gas that is spiraling towards the central star (this motion is known as *gas drag*). If we take a look at the equation (1.44) for the radial velocity of the dust, we can see that the gas drag makes small particles stick to the gas and move along with it: small grains have indeed $\tau_s \ll 1$, that leads to a radial velocity given by:

$$v_{\text{dust,R}} \approx v_{\text{gas,R}} - n \frac{c_{\text{s}}^2}{v_k^2} \tau_s v_k, \tag{1.55}$$

with v_k Keplerian velocity, that shows that highly coupled particles share the same motion as the gas, while poorly coupled ones have a velocity that decreases proportionally with

[12]Because the gas is rotating slower

the stopping time.
Both the drift and the drag cause the dust to spiral towards the central star, with a frequency that depends on the Stokes number and on the dust-to-gas ratio. The gas on the other hand, feels a headwind that pushes it towards external regions, allowing it to gather angular momentum. The two main sources responsible for the gas drifting outside are pressure, that generates the drag term:

$$|\Delta v| \approx \left(\frac{h_{\rm g}}{R}\right)^2 v_k, \tag{1.56}$$

with h_g gas scale height and v_k Keplerian velocity, and viscous forces responsible for the radial drift:

$$|v_\nu| \approx \alpha_{ss} \left(\frac{h_{\rm g}}{R}\right)^2 v_k, \tag{1.57}$$

The ratio between these two forces is approximately:

$$\Delta v/v_\nu \approx \alpha_{\rm ss}{-}1 \tag{1.58}$$

that for protoplanetary disks is in the range $[10^2 - 10^4]$, therefore we expect the radial drift to be the dominant component for most of the Stokes numbers.

Dynamics of coupled particles $\mathrm{St} \ll 1$: In this regime the stopping time (equation (1.32)) is less than the dynamical time and dust and gas have the same dynamics.
Radial velocity of small grains $\mathrm{St} \ll |v_\nu|/|\Delta v| \approx \alpha_{\rm ss}$ is mainly dominated by the gas drag induced by viscous forces. In the $\mathrm{St} = 0$ case, both gas and dust orbit with speed $v_\nu(1+(\rho_{\rm dust}/\rho_{\rm gas}))$, with small deviation due to differential rotation. The orbital velocity of small grains becomes sub-Keplerian on a stopping timescale: the centrifugal acceleration not being able to counterbalance the gravitational pull would bring the grains to spiral inward, while the gas drag acting against the gravitational pull make the grains reach a limit velocity in a couple of stopping times.
In the case of big grains, $\alpha_{\rm ss} \ll \mathrm{St} \ll 1$, the grain radial velocity is bigger than the gas velocity (that feels the counter wind) and increases linearly with St till a maximum value for $\mathrm{St} = 1$.
Dust influences gas motion in different ways, depending on the dust-to-gas ratio:

- If $\varepsilon > \alpha_{\rm ss}/\mathrm{St}$ the dust can dynamically influence the motion of the gas, pushing it towards lower pressure regions in order to conserve angular momentum.

- If $\varepsilon < \alpha_{\rm ss}/\mathrm{St}$ the dust action is negligible and the gas moves with unperturbed radial velocity v_ν reduced by a factor $(1 + \varepsilon)$.

Partially coupled particles $\mathrm{St} \approx 1$**:** This is the regime in which the dust-gas interaction mainly affects the dynamics of the two fluids. In this regime, dust particles exchange angular momentum with gas very efficiently and drift at the highest rate possible.
Since $|\Delta v| \gg |v_\nu|$, the radial velocity of the gas has its maximum deviation from the radial flux and leads to a drift towards external regions. This effects is relevant for $\varepsilon \gg 2\alpha_{\mathrm{ss}}/(1-\alpha_{\mathrm{ss}})\ 2\alpha_{\mathrm{ss}}$ and cannot be neglected. The orbital motion of the dust increases from a value of approximately half of the gases unperturbed velocity to the Keplerian value $v_{\mathrm{dust},\phi} = 0$, while the gas accelerates its orbital motion to near that of its unperturbed velocity as it gains angular momentum from the in-spiraling dust flux.

Poorly coupled particles $\mathrm{St} \gg 1$**:** In this regime the motion of the dust is decoupled from the gas one, which causes the gases velocity to approximately be the unperturbed Keplerian one, given by equation (1.10), while the dust's velocity is approximately zero,

$$v_{\mathrm{dust},R} \approx 0, \tag{1.59}$$

$$v_{\mathrm{dust},\phi} \approx 0. \tag{1.60}$$

In this regime the stopping time is much larger than the Keplerian dynamical timescale, therefore, gas and dust are decoupled and their velocities are dust-to-gas ratio independent. In this regime $\mathrm{St} \gg \varepsilon\alpha_{\mathrm{ss}}/(1+\varepsilon)$, thus the viscous term in the radial motion of the gas is negligible.
Since the dust grain radial velocity is almost Keplerian, grains do not migrate inward, while the gas radial motion is dominated by the viscous forces and its velocity is sub-Keplerian due to the pressure.
We can state that the radial drift produces a fast migration of big dust grains towards the innermost parts of the disk,

$$t_{\mathrm{drift}}\Omega_k = \frac{R\Omega_k}{|v_{\mathrm{dust},R}|} \approx (1+\varepsilon)\ \frac{1+\mathrm{St}^2}{\mathrm{St}}\ \left(\frac{h_{\mathrm{g}}}{R}\right)^{-2}. \tag{1.61}$$

Typical values for particles with $\mathrm{St} = 1$ are of the order of $10^2\Omega_k$ and depend on the local value of the disk proportion, therefore the radial velocity induced by the gas drag can be big enough to rapidly end uncoupled particles.

Dust dynamics in turbulent flows

The dust dynamics in turbulent flows is derived from the results of the laminar flows, by adding a correction due to the turbulence. We now proceed to analyse the contribution to the radial and vertical motion due to the stochastic turbulence of the gas. The gas in the disk shows oscillations in the velocity field that cause turbulence in the dust (the strength depends on how much the dust is coupled with the gas), preventing smaller grains

from settling down in the midplane. This process, however, does not alter the mean flow responsible for the radial drift, which still moves with Keplerian velocity.
The regime in which the turbulence is most relevant is the one of small and well-coupled particles, that can both diffuse in the turbulent flux and follow the mean motion of the gas. The aerodynamical dust-gas coupling generates a turbulent motion of the dust caused by the gas drag, which we can treat as a "correction term" to the case of laminar flows. The turbulent velocity has two different origins:

- **Vertical turbulent velocity:** Due to stochastic oscillations of the gas velocity around the midplane.
- **Radial and azimuthal turbulent velocity:** Due to epicyclic stochastic oscillations of the gas velocity field. In this case, the turbulence is anisotropic.

The radial and vertical diffusivities that we already defined in equation (1.21) of the gas near the midplane can be approximated through the cinematic viscosity $D_{\mathrm{gas},R} \approx D_{\mathrm{gas},z} \approx \nu$, while the ones of the dust can be approximated by,

$$D_{\mathrm{dust},R} \cong \nu \, \frac{1+\mathrm{St}}{1+2\mathrm{St}}, \tag{1.62}$$

$$D_{\mathrm{dust},z} \cong \nu \frac{1+4\mathrm{St}^2}{\left(1+\mathrm{St}^2\right)^2} \approx \frac{\nu}{1+\mathrm{St}^2}. \tag{1.63}$$

For highly coupled particles ($\mathrm{St} \ll 1$) the two diffusivities are almost identical, while poorly coupled particles ($\mathrm{St} \gg 1$) have $D_{\mathrm{dust},z} = \nu/2$ and $D_{\mathrm{dust},R} \ll \nu$. The main effect of diffusivity in a mix of two different fluids is to purify the concentrations. Let's consider a fluid in which the gas is the dominant component and the dust cannot influence the gas motion (i.e. the limit for $\varepsilon \ll 1$). The radial evolution of the dust surface density can be described by the sum of an advective term, due to the motion of the dust induced by the viscous and orbital motion of the gas, and a diffusive term, due to the radial gradient of the dust-to-gas ratio:

$$\frac{\partial \Sigma_{\mathrm{dust}}}{\partial t} + \frac{1}{R}\frac{\partial}{\partial R}\left(R\left(\Sigma_{\mathrm{dust}} v_{\mathrm{dust},R} - D_{\mathrm{dust},R}\Sigma_{\mathrm{gas}}\frac{\partial}{\partial R}\left(\frac{\Sigma_{\mathrm{dust}}}{\Sigma_{\mathrm{gas}}}\right)\right)\right) = 0. \tag{1.64}$$

This equation is obtained by combining the continuity equation (1.2) with the expression describing the dust flux, which is given by the sum of an advective and diffusive term:

$$\mathbf{F}_{\mathrm{dust}} = \Sigma_{\mathrm{dust}}\mathbf{v} - D\Sigma_{\mathrm{gas}}\nabla\frac{\Sigma_{\mathrm{dust}}}{\Sigma_{\mathrm{gas}}}, \tag{1.65}$$

with $\mathbf{v}$ average velocity of the gas in the disk and D diffusivity coefficient.

We can quantify the relevance of advection compared to diffusion through the Schmidt number:

$$\mathrm{Sc} \equiv \frac{\nu}{D}, \tag{1.66}$$

the smaller this number, the more important is diffusion over advection.

Dust settling The turbulence in the gas hinders the dust from settling on the midplane. Usually, dust particles in the disk are small and highly coupled to the gas, thus we can estimate for this scenario the condition under which the vertical settling is completely hindered. The dust surface density evolution caused by settling and diffusion can be expressed as (Fromang, Papaloizou, 2006):

$$\frac{\partial \rho_{\rm dust}}{\partial t} - \frac{\partial}{\partial z}\left(z\Omega_k St\ \rho_{\rm dust}\right) - \frac{\partial}{\partial z}\left(D_{{\rm dust},z}\rho_{\rm gas}\frac{\partial}{\partial z}\left(\frac{\rho_{\rm dust}}{\rho_{\rm gas}}\right)\right) = 0. \tag{1.67}$$

By integrating and rearranging equation (1.67), and assuming the diffusivity to be constant along z, we get as a solution of equation (1.67):

$$\rho_{\rm dust} = \rho_{\rm dust,0}\exp\left[-\frac{z^2}{2H_g^2} - \frac{St_0}{\alpha}\left(\exp\left[\frac{z^2}{2H_g^2}\right] - 1\right)\right], \tag{1.68}$$

where we used $\nu = \alpha_{\rm ss} h_{\rm g}^2 \Omega_k$. Non coupled particles that usually populate the outermost parts of the disk are more numerous on the midplane. Close to the midplane, solution (1.68) tends to a Gaussian profile with scale height given by:

$$h_{\rm d} = h_{\rm g}\sqrt{\frac{\alpha_{\rm ss}}{\alpha_{\rm ss} + St}}. \tag{1.69}$$

For $\mathrm{St}_0 \gg \alpha_{\rm ss}$, if we assume $\rho(z) = const$ and thus also $\mathrm{St} = const.$ we recover the relation $h_{\rm d} = h_{\rm g}\sqrt{\frac{\alpha_{\rm ss}}{St}}$.

We can therefore observe that the particles concentrate more if their Stokes number exceeds $\alpha_{\rm ss}$ by a lot, furthermore we can affirm that the settling process is more efficient in the external regions of the disk where Stokes numbers are higher, the gas drag is smaller.

1.2 Planet formation

The precise formation pathway of planets is still an open and debated question. The main idea is that they form by aggregation of dust particles into larger objects (called planetesimals) until they are big enough to dynamically evolve under the effect of mutual interactions rather than dust-gas coupling. These planetesimals gravitationally interact with the remaining material and accrete more mass until they form terrestrial planets and core of gas giants.
The newly formed planets may migrate inside the disk and accrete more solid material from different regions of the disk, while the cores of gas giants are also able to accrete gaseous envelopes.

In this work, we will consider different possible planetary formation scenarios and compare them. The most accredited models are divided into:

- Growth of planetary cores via planetesimal accretion (Mordasini, C. et al., 2012; Emsenhuber et al., 2021).

- Growth of planetary cores via pebble accretion (Lambrechts, M., Johansen, A., 2012; Bitsch, Bertram et al., 2015).

In the following Subsections, we will give an overview of the state of art theories about planetary formation, namely pebble and planetesimal formation and accretion.

1.2.1 Planetesimal formation

Planetesimal formation is a key point in the planet formation process, but still is a very uncertain one. Particularly, the formation of planetesimals presents some hindering barriers:

- **Bouncing barrier**: In order for two pebbles to accrete into a bigger size object, they need to stick together once they encounter each other. Compact particles are able to stick together only if their relative speed is below a certain threshold, that decreases as the mass of the particle increases. Generally, compact particles are more prone to bouncing rather than sticking. In the case of protoplanetary disks, the bouncing barrier is set when the turbulent collision speed[13] (v_c) is equal to the sticking speed (v_s):

$$v_\mathrm{s} = \sqrt{\frac{5\pi a_0 F_\mathrm{roll}}{m}}, \tag{1.71}$$

  with a_0 size of the particle, F_roll the force needed to roll a particle over the surface of another particle and m reduced mass of colliding dust aggregates (Güttler, C. et al., 2010). In terms of Stokes number we can express the bouncing barrier as:

$$\mathrm{St} = \left(\frac{15(2\pi)^{3/2} a_0 F_\mathrm{roll} \rho_\bullet^2}{6\alpha c_\mathrm{s}^2 \Sigma_\mathrm{g}^3}\right)^{1/4}, \tag{1.72}$$

  with material density $\rho_\bullet$ of the particle. The bouncing barrier is clearly very severe for compact silicate particles, while water ice has much higher surface energy than silicates and hence ice aggregates resist compression in collisions. Porous particles, instead, can form large aggregates because they have high sticky efficiencies.

[13] The Stokes number determines the turbulent collision speed of particles with $\mathrm{St} < 1$ (Ormel, C. W., Cuzzi, J. N., 2007):

$$v_\mathrm{c} = \sqrt{3}\sqrt{\alpha}\sqrt{\mathrm{St}} c_\mathrm{s} \tag{1.70}$$

- **Fragmentation barrier**: icy solids may not be affected by the bouncing barrier but their growth can be halted at larger sizes due to fragmentation as collision velocities increase. This barrier is obtained by setting the collision speed of particles v_c equals to a critical fragmentation speed v_f.

  It can be expressed in terms of Stokes number (Birnstiel, T. et al., 2012):

  $$\mathrm{St}_\mathrm{frag} = \frac{1}{3\alpha_\mathrm{t}} \left(\frac{v_\mathrm{f}}{c_\mathrm{s}} \right)^2 . \tag{1.73}$$

  The fragmentation threshold is, in reality, a complicated function of the porosity and relative size of impactor and target, but for simplicity, one can set v_f to be a constant to obtain an approximate expression for the fragmentation barrier.

- **Drift barrier**: Particles that can avoid bouncing and fragmentation barriers, like very fluffy ice particles, still face the radial drift barrier, that arises because the gas rotates with sub-Keplerian velocity, making the dust lose angular momentum and spiral towards the star with a rate that increases as its size grows. In particular, this barrier is encountered when the growth timescale $\mathrm{St}/\dot{\mathrm{St}}$ equals the radial drift timescale $r/\dot{r}$ and can be expressed as,

  $$\mathrm{St}_\mathrm{drift} = \frac{\Sigma_\mathrm{d}}{\Sigma_\mathrm{g}} \left(\frac{v_\mathrm{K}}{c_\mathrm{s}} \right)^2 \left| \frac{\partial \ln P}{\partial \ln r} \right|^{-1} . \tag{1.74}$$

Streaming instability

One of the most accredited scenario for planetesimal formation is the streaming instability, i.e. the formation of denser filaments inside the disk that become gravitationally unstable and collapse into a planetesimal without having to pass through the growth barrier.
Streaming instability is driven by the difference in motion of the gas and solid particles in the disk. We already know that the gas rotates at a sub-Keplerian velocity because it is sustained by the radial pressure gradient created by the denser and hotter gas in the internal regions. In contrast to it, dust rotates faster, which causes it to slow down due to the interaction with the gas that triggers loss of angular momentum due to aerodynamical drag. The situation changes when solid particles start to cluster in the gas, as they feel less headwind from the gas and are allowed to rotate faster, reducing also the inward drift. At this point, the slower drifting cluster are joined by faster inward drifting particles, increasing the local density and further reducing the radial drift, triggering an exponential growth of the initial cluster. This is the mechanism that triggers the denser filaments formation, that can also overcome gas density by a factor of 1000, sufficient to start the direct gravitational collapse. The impacts' speed during these early stages are generally low, allowing the formation of porous planetesimals with low density.

The condition for the streaming instability are not necessarily found in a real disk, where, usually, the dust-to-gas ratio is around 1%, therefore, other planetesimal formation mechanisms are required. In the gas rich phase one possible mechanism to trigger streaming instability is the pebble pile-up, while a late stage trigger mechanism could be disk photoevaporation.

Laboratory experiments have shown that icy aggregate are significantly more sticky than silicate grains, leading to larger size aggregates, before they fragment, or even growing directly to planetesimal size if they are sufficiently porous.

In the following paragraph we will present the planetesimal formation method investigated by Lenz et al. (2019), while in Appendix 4 the Drążkowska, Alibert (2017) planetesimal formation is presented.

Lenz et al. (2019) method

This method of planetesimal formation is based on the idea presented in Lenz et al. (2019), that planetesimals form in "particle traps", which exist due to a local enhancement of the dust to gas ratio as a result of a sufficiently high local pebble flux. The location of these traps can emerge everywhere in the disk as a result of different types of instabilities (hydrodynamic- or magnetic instabilities). Their occurrence and lifetime is subject of ongoing research, thus they need to be implemented via free parameters in numerical simulations.

The model The important parameters for planetesimal formation are the lifetime of pebble traps $\tau_{\rm l}$ (such as vortices or zonal flows) and their radial separation d.

In order to pile up the particles there is no need for a pressure bump with a local maximum. In fact, a smaller pressure gradient implies a smaller drift speed, and conservation of mass flux leads to denser particle accumulation, therefore a flattened pressure profile without a local maximum still works. In this scenario, the density is increased leading to a higher dust-to-gas ratio ($\Sigma_{\rm d}/\Sigma_{\rm g}$), and the parameter d will be interpreted as the distance between such flat pressure structures.

Another important parameter for the model is the Stokes number of the particles, that quantifies the particle's coupling with the gas.

Finally, the last relevant parameter for the process is the efficiency parameter ε, that tells how much of the pebble flux can be trapped and converted into planetesimals.

The column density of drifting pebbles can be converted into column density of planetesimals with the following recipe,

$$\dot{\Sigma}_{\rm pla}(r) = \frac{\varepsilon}{d(r)} \frac{\dot{M}_{\rm peb}}{2\pi r}, \tag{1.75}$$

with

$$\dot{M}_{\rm peb} = 2\pi r \sum_{\rm St_{min} \leq St \leq St_{max}} |v_{\rm drift}(r, {\rm St})| \Sigma_{\rm d}(r, {\rm St}), \tag{1.76}$$

where $v_{\rm drift}$ is the radial drifting velocity of the particles, $\Sigma_{\rm d}(r, {\rm St})$ the column density in particles[14] that have the required Stokes number and $\rm St_{min}$ and $\rm St_{max}$ minimum and maximum Stokes number of particles able to participate in the streaming instability to facilitate gravitational collapse.

A conversion length is defined as follows:

$$l = \frac{d}{\varepsilon}. \tag{1.77}$$

To understand the meaning of this length, let us consider a one particle species scenario, with pebbles distributed according to $\Sigma_{\rm peb}$, drifting at speed $v_{\rm drift}$ in which we distribute the newly formed planetesimal column density over the trap distance d. The quantity $l/v_{\rm drift} = d/\varepsilon \cdot v_{\rm drift}$ represents the timescale of conversion of pebbles into planetesimals, therefore, $(v_{\rm drift}/l) \cdot \Sigma_{\rm peb}$ is the rate at which we trasform $\Sigma_{\rm peb}$ into $\Sigma_{\rm pla}$.

The spatial pressure structures, e.g. real pressure bumps traps like vortices, that here are assumed to be infinitesimals, move radially with the gas of the smooth profile. As a consequence of the assumption that $\alpha_{\rm t}$ has a non-zero value everywhere, turbulence structures can be formed everywhere in the disk.

The typical length scale of planetesimal formation is of the order of $0.01 h_g$ and it depends on particle diffusion and Stokes number. This is not resolved in numerical simulations, thus all the traps and planetesimal formation properties is embedded in the efficiency parameter ε.

Particles are assumed to be spherical objects with constant material density $\rho_{\rm s} = 1.2 {\rm g/cm^3}$, according to asteroid data (Carry, 2012). In this way, the mass of a planetesimal of 100 km diameter[15] is given by:

$$m_{\rm pla} = \frac{4\pi}{3} (50 {\rm km})^3 \rho_{\rm s} \approx 1.05 \cdot 10^{-7} M_{\oplus}. \tag{1.78}$$

According to the model, planetesimal can only form if enough mass can be accumulated inside a trap within its lifetime $\tau_{\rm l}$, expressed by the condition:

$$\varepsilon \tau_{\rm l} \dot{M}_{\rm peb} > m_{\rm pla}, \tag{1.79}$$

that leads to a critical flux for planetesimal formation of:

$$\dot{M}_{\rm cr} > \frac{m_{\rm pla}}{\varepsilon \tau_{\rm l}}. \tag{1.80}$$

[14] The unit of the column density is still $\rm g/cm^3$.

[15] Supported by data from our Solar System.

The physical processes involved in a particle trap are the following: turbulent particle diffusion tries to dissolve the particle overdensity, while the overdensity tries to gravitationally collapse. There is, therefore, a critical cloud diameter $l_{\rm c}$ that has to be reached in order for the gravity to win. This length is derived by equating the diffusion and collapse timescale, and leads to:

$$l_{\rm c} = \frac{2}{3}\sqrt{\frac{\delta}{\rm St}}h_{\rm g}, \tag{1.81}$$

with δ dimensionless diffusion parameter[16]. To build a planetesimal, the particles need to concentrate and reach Hill density ($\rho_{\rm Hill}$) in a volume $l_{\rm c}^3$. The condition on the pebble volume density to reach planetesimal formation will read:

$$\begin{aligned}\rho_{\rm Hill} \leq \rho_{\rm peb,l_c} \approx \frac{\varepsilon}{(4\pi 3) l_z l_r l_\phi / 2\pi} \sum_{\rm St_{min} \leq St \leq St_{max}} \\ \left(\int_{r-d_r/2}^{r+d_r/2} \Sigma_{\rm peb}(t_1, {\rm St}) dr + \int_{t_1}^{t} \Sigma_{\rm peb}(t, {\rm St}) |v_{\rm peb}(t, {\rm St})| dt \right),\end{aligned} \tag{1.82}$$

where it has been considered that particles are more likely to concentrate in spherical shapes (thus the addition of the $4\pi/3$ term). The resulting planetesimal mass will be given by:

$$\frac{4\pi}{3} l_{\rm c}^3 \rho_{\rm Hill} = m_{\rm pla}. \tag{1.83}$$

The second term in equation (1.82) is the dominant one. Neglecting the first one and using equation (1.83) we are able to recover the condition from equation (1.78).

Considering that the collapse leading to planetesimal formation occurs on a timescale equal to the lifetime of the trap $\tau = \tau_l$ and that the flux does not change significantly, even if it does, this will not affect the outcome of either forming or not forming planetesimals.

We consider the particle's drift speed $v_{\rm drift}$ as the relative velocity of the particles with respect to the turbulence causing the collapse. In principle, zonal flows can have their own speed that would change the relative velocity, but if this speed is much smaller than the drift speed itself, it can be neglected.

Additionally, ε is taken as a constant because we cannot quantify how it changes with radius and Stokes number.

Planetesimal formation This method for planetesimal formation is directly linked to the local pebble flux and not local dust-to-gas ratio or local density relying on parameters such as lifetime of pressure-bump structures, contributing particle Stokes numbers, the radial particle trap density ($1/l$) and an efficiency parameter describing the conversion from pebbles to planetesimals.

[16]Is the diffusion parameter divided by $c_{\rm s}h_{\rm g}$.

This model is the first model that is able to create planetesimal everywhere in the disk, therefore it has been chosen in this work to investigate the effects of planetesimal accretion.

We know that trapping and collapse to planetesimal works for particles with $\mathrm{St} = 10^{-2}$, whit a maximum Stokes number of $\mathrm{St}_{\max} \approx 10$ (Carrera, Daniel et al., 2015), while streaming instability is still possible for $\mathrm{St} = 10^{-3}$ but we are not sure if they also contribute to planetesimal formation.

As already mentioned, planetesimal forms in particles trap that origin from vortices or zonal flows, that would lead to a modified gas velocity with respect to the one that we have in smooth pressure structures. This difference is, however, smaller than the drift velocity and thus neglected.

Planetesimal formation itself is treated in numerical simulations as a sink term in the advection-diffusion equation (1.64) for the column density of a single particle species of mass m_i, given by:

$$\begin{aligned} \frac{\partial \Sigma_{\mathrm{d}}^i}{\partial t} + \frac{1}{r}\frac{\partial}{\partial r}\left[r\left(\Sigma_{\mathrm{d}}^i v_{\mathrm{r}}^i - D_{\mathrm{d}}^i \frac{\partial}{\partial r}\left(\frac{\Sigma_{\mathrm{d}}^i}{\Sigma_{\mathrm{g}}}\right)\Sigma_{\mathrm{g}}\right)\right] = \\ -\frac{\varepsilon}{d}\left|v_{\mathrm{drift}}^i\right| \Sigma_{\mathrm{d}}^i \cdot \Theta(\dot{M}_{\mathrm{peb}} - \dot{M}_{\mathrm{cr}})\Theta(\mathrm{St}_i - \mathrm{St}_{\min}) \cdot \Theta(\mathrm{St}_{\min} - \mathrm{St}_i), \end{aligned} \tag{1.84}$$

where $\Theta(\cdot)$ are Heaviside functions and represent the conditions that the pebble flux must be critical and that only a limited range of particles $\mathrm{St}_{\min} \leq \mathrm{St} \leq \mathrm{St}_{\max}$ are allowed to build planetesimals. Stronger turbulence levels provide higher fluxes of pebble for longer times, as we can see comparing the right and left panels of Figure 1.5, because they slow down the inward drift, leading to higher chances of planetesimal formation in the outer region.

In the low viscosity case, $\alpha_{\mathrm{t}} = 10^{-3}$ (left panel of Figure 1.5), at early stages, the flux for lower α_{t} is lower for the same reason, making it less probable to form planetesimals in the inner part of the disk at early stages. At later times (around 10^6 Myrs) the pebble to total mass flux ratio drops significantly, due to the drift barrier, which drops to smaller sized particles since Σ_{d} is decreasing. Since the mass reservoir for planetesimal formation is in the outer disk, where gas densities are very low, the pebble flux in the outer region around $\approx 200 - 400$ AU already reaches critical values at early times ($< 10^4$) yrs, as we can see in Figure 1.6. The grey area in Figure 1.6 marks the region where particles are too small to participate in planetesimal formation.

Column density formation rate We can summarize the effects of different turbulence of the disk as follows:

- $\alpha_{\mathrm{t}} = 10^{-2}$: Higher efficiencies lead to higher planetesimal formation rates, that, however, decline faster. This still ends in a more abundant planetesimal population for higher ε.

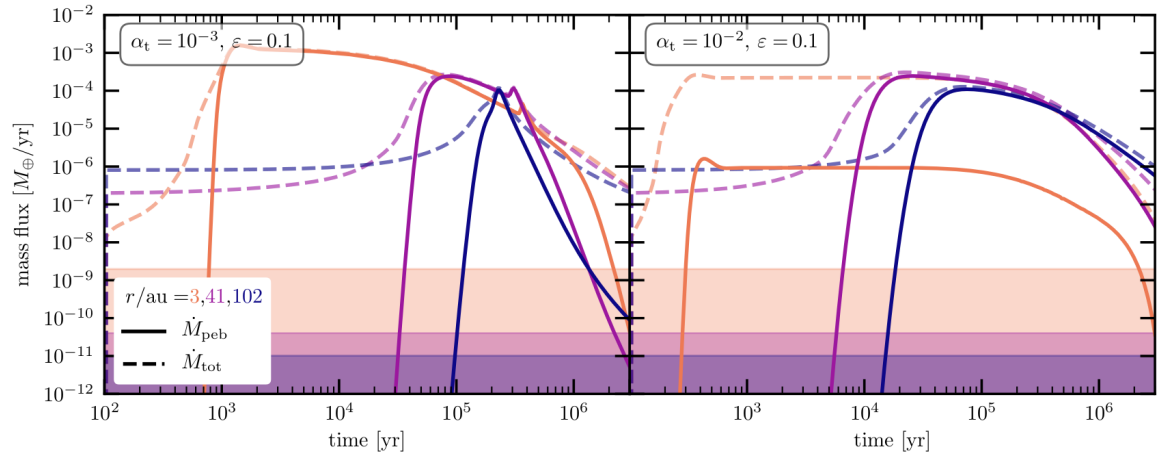

Figure 1.5: Evolution of mass flux as a function of time, for different turbulence parameter (left and right panel) for different radii: 3 au (orange), 41 au (purple), 102 au (dark blue). The shaded areas identify locations where the pebble flux is below the critical value required to form planetesimals. We can see that for stronger turbulences (right panel), the pebble flux stays at higher values for longer times, because particles grow smaller and thus drift slower, leading to higher chances to form planetesimal in the outer part of the disk. (Lenz et al., 2019).

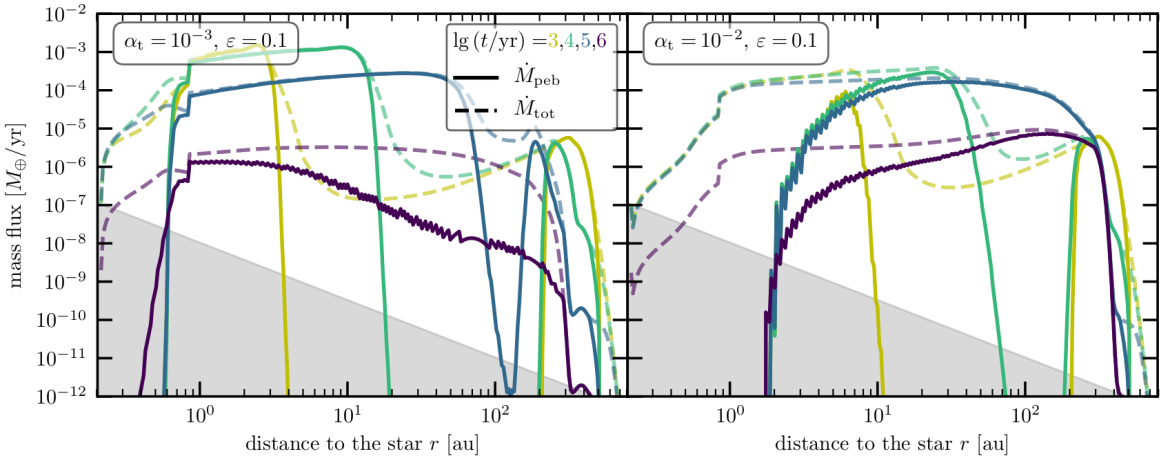

Figure 1.6: Local pebble flux $\dot{M}_{peb}$ of particles with $10^{-2} < \mathrm{St} < 10$ for two different values of disk turbulence (left and right panel) as a function of radius. The different colors represents respectively $t = 10^3$ (yellow) to $t = 10^6$ (purple) yrs in step of decades. The grey shaded area represents the mass flux below the critical value required to form planetesimals. We observe that the (Lenz et al., 2019).

- $\alpha_t = 10^{-3}$: In this case the formation rate is higher for larger efficiencies in the outer disk. Radial drift removes the largest particles of the top-heavy size distribution. If few particles are converted into planetesimals in the outer disk (as it happens for smaller ε), there is more material left available to form planetesimals inside, due to mass conservation, leading to more planetesimals in the inner disk for smaller efficiencies. this effect cannot be seen for higher values of turbulence because the fragmentation events slow down the radial motion and the feeding zones of planetesimals are much narrower.

Surface densities Figure 1.7 shows the gas, dust, and planetesimal surface densities as a function of distance from the central star (top panels) for some time snapshots and as a function of time (bottom panels) for some fixed positions. Right, and left panels show the two turbulence parameters. We can see that in the case of low turbulence (left panels of Figure 1.7), planetesimals form at $2-3$ AU already after a few thousand years and at $20-30$ AU after a few ten to hundred thousand years.

If turbulence is strong ($\alpha_t = 10^{-2}$, right panel), fragmentation will be the growth limiting process and the maximum size of the grains will be smaller (furthermore, there will also be more small grains in general). Hence, compared to the weaker turbulence case ($\alpha_t = 10^{-3}$, left panel), particles in the outer disk maintain their position for longer times and are more likely to form planetesimals. This results in a higher planetesimal surface density in the outer regions for the strong turbulence case.

Regarding the ratios between surface densities, we can notice that:

- The dust-to-gas ratio Σ_d/Σ_g is constantly decreasing and it decreases faster for smaller α_t because particles drift faster.

- The planetesimal-to-dust ratio Σ_p/Σ_d reaches, within 2 AU, values above unity after 10^4 yrs in the case of $\alpha_t = 10^{-3}$, while for $\alpha_t = 10^{-2}$ the values above unity are reached only at later times ($\geq 10^6$).

We can notice a kink in the surface densities of dust and planetesimal roughly around 0.8 AU in the low viscosity case (left panel of Figure 1.7). This is due to the presence of the water iceline, around which particles pile up.

In Appendix 4 we compare our pebble, planetesimal and gas surface density for different planetesimal formation efficiencies with the results obtained by Lenz et al. (2019). In our case, we observe the typical kink not only for the water evaporation line but for all the evaporation lines considered in the code.

We observe from Figure 1.7, as well as in our surface density plot in Figure 4, that the planetesimal surface density has a steeper profile than the gas and dust[17] surface density.

[17]Pebble in our case.

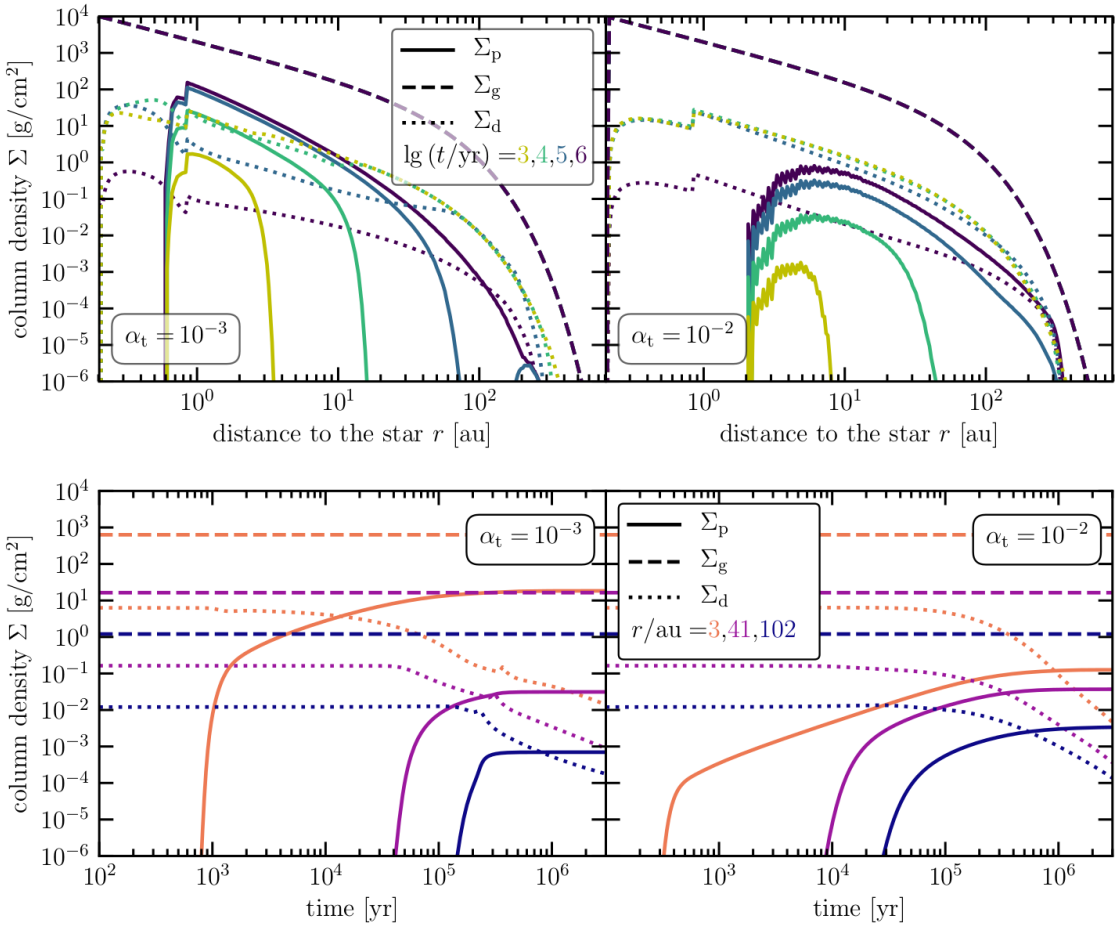

Figure 1.7: Dust, gas and planetesimal surface densities as a function of the distance from the central star for different snapshots (top panels) and as a function of time for fixed radii (bottom panels), for two values of turbulence. We notice the characteristic kink around 0.8 AU due to the water iceline. We observe the same kink in the planetesimal surface densities for every evaporation line that we consider in our study, as shown in the plot 4 in Appendix 4.

This is due to the r-dependency of the trap size $d \propto h_g$ as well as transport phenomena. In general we find the planetesimal surface density to be steeper than the gas one if the effective efficiency $1/l = \varepsilon/d$ is sufficiently small[18]. If this effective efficiency is large, the feeding zone of planetesimals is smaller and the slope resembles the initial dust density profile.

Model limitation This description of planetesimal formation is based on some key assumptions: The disk is not allowed to viscously evolve, nor the photoevaporation sink term is included. The temperature profile is kept constant and viscous heating is ignored, furthermore, the drift velocity is kept as in the case of a smooth gas profile, although pressure bumps would cause a loss of momenta[19].

Planetesimals, in this model, are not allowed to interact with each other (collisions are ignored) and cannot accrete through pebble accretion.

Conclusions Summarizing, we can say that the planetesimal distribution and the total mass of initial planetesimals obtained with the Lenz et al. (2019) method highly depend on the level of turbulence α_t, i.e. whether particle growth is limited by fragmentation or drift.

In the limited disk fragmentation case, higher ε/d lead to higher planetesimal formation rates that decline faster.

If the disk is drift limited, material drifts faster and particles that were not converted into planetesimals in the outer disk can build planetesimals in the inner part. This only happens if the turbulence is not too high and results in a slope of the planetesimal surface density that is steeper than the gas one. Generally, this profile equates to a power law in the inner part of the disk with an exponential cut-off in its outer regions.

1.2.2 Planetesimal accretion

Planetesimal accretion rate: Johansen, Bitsch (2019)

In this work, we will follow Johansen, Bitsch (2019) in the modeling approach of the planetesimal accretion rate. This model is developed using the constraints derived from those of our Solar System: Those being, total planetesimal mass, characteristic planetesimal size and the strength of inclination stirring by the turbulent gas.

The birth-sizes of planetesimals are well constrained in the Solar System. Indeed, the size distribution of asteroids in the main belt is consistent with the formation of bodies of a characteristic size of 100 km and subsequent growth of larger bodies (up to Ceres mass or even to the mass of protoplanets) by accretion of millimeter-sized pebbles.

[18] in our case $1/l = 0.02/h_g$ for $\varepsilon = 0.1$

[19] The effect is not considered due to lack of information on how vortices or zonal flows would affect v_{drift}.

The inclination of the planetesimal population is another important parameter in setting the efficiency of planetesimal accretion. Planetesimal inclinations are mainly stirred by mutual scattering and by gravitational torques from the turbulent gas.

Planetesimals that revolve around the protostar experience mutual gravitational scatterings and direct collisions through which they grow, finally, into planets. Mathematical descriptions of such processes (i.e., gravitational scattering and mutual collisions), have to be formulated, at least, as a three-body problem: the protostar and two interacting planetesimals. All the equations are normalized using the dynamics properties around the protoplanet orbiting at distance r, while the distances are normalized to the Hill radius.

Accretion rate The accretion rate, in the case of a single migrating protoplanet, is given by:

$$\dot{M} = \varepsilon \dot{M}_{\rm pla} = \varepsilon 2\pi r \dot{r} \Sigma_{\rm pla}, \tag{1.85}$$

where ε is the accretion efficiency and $\dot{M}_{\rm pla}$ is the flux of planetesimals that cross the orbit of the migrating protoplanet. The migration speed is computed using the inverse of the normalized migration timescale:

$$\dot{\tilde{b}}_{\rm p} = \tilde{\tau}_{\rm mig}^{-1}, \tag{1.86}$$

while the accretion rate is given by:

$$\varepsilon = \alpha_{\rm pla} \dot{\tilde{b}}_{\rm p}^{\beta_{\rm pla}-1}, \tag{1.87}$$

where $\alpha_{\rm pla}$ and $\beta_{\rm pla}$ are fits to numerical simulations given by (Tanaka, Ida, 1999):

$$\alpha_{\rm pla} = 2.5 \sqrt{\frac{\tilde{R}_{\rm p}}{1 + 0.37 \tilde{i}_0^2 / \tilde{R}_{\rm p}}}, \tag{1.88}$$

$$\beta_{\rm pla} = 0.79 (1 + 10 \tilde{i}_0^2)^{-0.17}, \tag{1.89}$$

with $\tilde{i}_0$ being the inclination of the planetesimal population.

The inclination of the planetesimal population is an important parameter for the accretion rate because the protoplanet induces the inclination of the planetesimals.

We mainly set the inclination from the balance between the stirring by the turbulent gas and damping by gas drag, but for experiments with a very or extremely weak turbulent stirring, the inclination excitation by mutual planetesimal scatterings must also be included.

Accretion efficiency First, we compute the accretion efficiency using Tanaka, Ida (1999)'s approach for two values of the turbulent stirring (weak $\gamma = 10^{-4}$ and very weak $\gamma = 10^{-5}$) as a function of the distance from the star and the mass of the protoplanet, taking into account only the turbulent stirring by the gas. We ignored viscous heating,

which would heat up the inner regions of the disk and therefore decrease the migration rate, making the planets more prone to shepherding. The accretion rates that we consider are an evolutionary sequence: The older the disk, the smaller the accretion rate. The stellar accretion rate affects planetesimal accretion mainly through the gas surface density, which is responsible for regulating the migration rate and the inclination of planetesimals that are in equilibrium between turbulent stirring and gas damping. Figure 1.8 shows the accretion efficiency of a protoplanet accreting planetesimals of radius 50 km for weak stirring ($\gamma = 10^{-4}$, left panel) and very weak stirring ($\gamma = 10^{-5}$, right panel), as a function of the distance from the star and as a function of the protoplanet mass. Each row represents a different mass accretion rate (increasing from top to bottom), while the red line marks the transition of the protoplanet from accreting predator (inside the red line) to non-accreting shepherd (outside the red line). We see that lowering the turbulent stirring increases the efficiency by a factor 3, mainly due to the α term in equation (1.88).

We also observe that lower stellar mass accretion rates lead to higher efficiencies because more slowly migrating planets[20] accrete a larger fraction of the planetesimal flux.

The transition of the planet between predator (accretes planetesimals) and shepherd (does not accrete), marked with a red line in Figure 1.8, depends on the gas drag timescale and on the migration speed. The transition to shepherding generally occurs at around 1 AU from the star in the final decade of core growth ($M \approx 1 - 10 M_{\oplus}$). Cores with lower mass transition to shepherding farther out.

Performing different simulations for different parameters it can be noticed that the final mass of the planets decreases for planets starting at late times, because they have less time to grow, while protoplanets that start their growth close to the star or late in the disk evolution migrate slowly enough to become planetesimal shepherds.

Capture radius: Valletta, Helled (2021)

In this work we will use the description of Valletta, Helled (2021) to model the capture radius for planetesimal accretion.

The standard model for giant planet formation, the core accretion model (Pollack et al., 1996), predicts that the growth of a giant planet begins with the formation of a heavy element core. Once the planet reaches Mars' mass, the gravity is sufficiently high to allow hydrogen and helium gas accretion from the disk. At this point, the planet will grow both solid (through planetesimal accretion) and gas, until it reaches the crossover mass and the gas runaway growth takes place.

The accretion rate, of course, depends on the planet's capture radius. If the protoplanet does not posses a gaseous envelope, the capture radius will simply be the core's radius.

In principle, in order to correctly predict the capture radius, one needs to compute the

[20] We recall that higher mass accretion rate implies a faster type I migration.

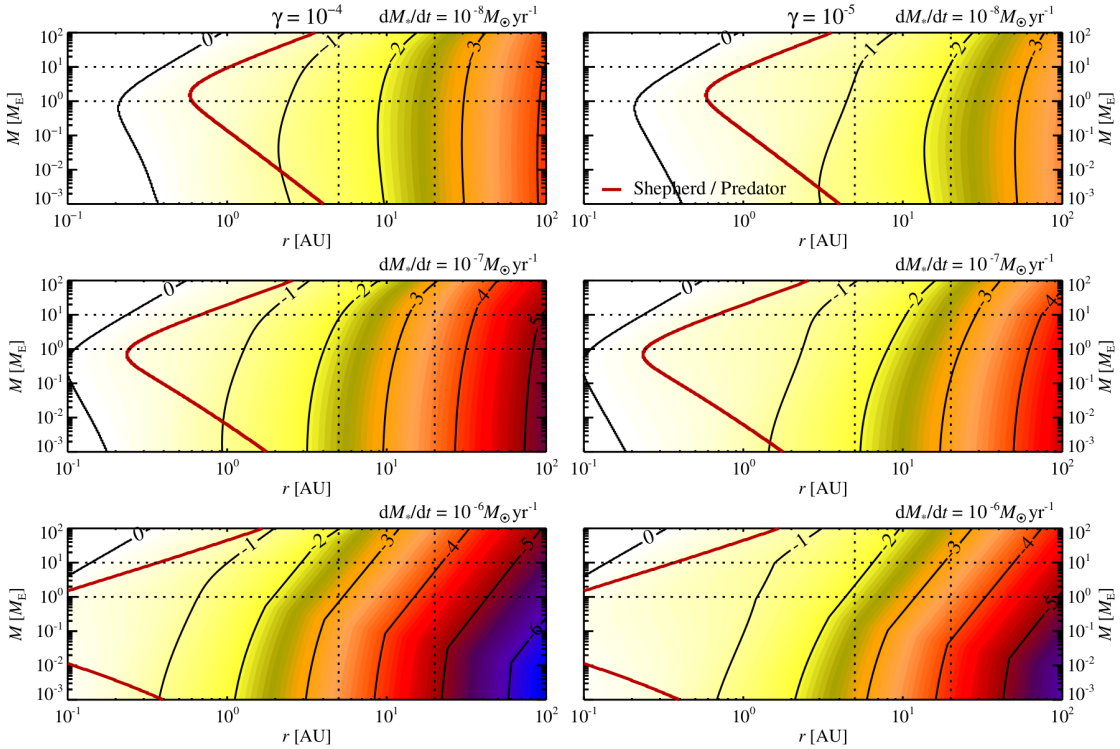

Figure 1.8: Accretion efficiency of a protoplanet accreting planetesimals of radius 50 km for weak stirring ($\gamma = 10^{-4}$, left panel) and very weak stirring ($\gamma = 10^{-5}$, right panel), as a function of the distance from the star and as a function of the protoplanet mass. The three rows show the accretion efficiency for three different increasing (top to bottom) values of the mass accretion rate through the disk, while the red line marks the transition of the protoplanet from an accreting predator (exterior of the red line) to a non-accreting shepherd (interior of the red line). The parameter region of core formation in the Solar System (the box made by 5 and 20 AU and by 1 and 10 $M_\oplus$) is marked with dashed lines. The efficiency overall increases with decreasing gas accretion through the disk because more slowly migrating planets accrete a higher fraction of the planetesimals that they migrate through.

trajectories of the planetesimals in the disk, solve the stellar structure equation within the protoplanet's envelope and take into account the drag force that the atmosphere exerts on the planetesimals. Inaba, S., Ikoma, M. (2003) have shown that the capture radius is significantly larger than the core's radius and that it depends mostly on the planetesimal size: The smaller the planetesimal, the bigger the capture radius.

In this work we implement the approximation derived in Valletta, Helled (2021) that does not require a numerical solution of the structure equations, but is still valid throughout all the planetary formation stages: Both when the planet is still attached to the disk and when it is already detached. The following paragraphs aim to describe the capture radius in these two different phases.

Attached phase When the planet is still embedded in the disk, its temperature and density are determined by its orbital location. We will define the outer radius of the planet as:

$$R_0 = \frac{GM_\mathrm{p}}{c_\mathrm{s}^2 + \frac{GM_\mathrm{p}}{0.25R_\mathrm{H}}}, \tag{1.90}$$

with M_p being the planet mass, R_H the Hill radius and c_s^2 the speed of sound in the disk.

The capture radius in this phase depends on the drag that the gas exerts on the planetesimals, which in itself is affected by the density profile of the planet's envelope, meaning that, to determine R_capt we need an estimate of the atmosphere's profile[21]. This estimate is inferred by means of the mass conservation, hydrostatic balance, thermal gradients, and energy conservation equations that regulate the envelope's structure:

$$\frac{\mathrm{d}m}{\mathrm{d}r} = 4\pi r^2 \rho, \tag{1.91}$$

$$\frac{\mathrm{d}P}{\mathrm{d}r} = -\frac{Gm}{r^2}\rho, \tag{1.92}$$

$$\frac{\mathrm{d}T}{\mathrm{d}r} = \nabla \frac{T}{P}\frac{\mathrm{d}P}{\mathrm{d}r}, \tag{1.93}$$

$$\frac{\mathrm{d}L}{\mathrm{d}r} = 4\pi r^2 \rho \left(\varepsilon - T\frac{\partial S}{\partial t}\right), \tag{1.94}$$

where m, r are the mass and radius coordinate respectively, ρ, P, T are the density, pressure and temperature in the envelope, L, S the luminosity and entropy, and $\nabla = \mathrm{d}\ln T/\mathrm{d}\ln P$ temperature gradient.

In the outer layers of the planet's envelope, the radiation transports the heat, resulting in an almost constant temperature profile and exponentially increasing pressure and

[21] Most important are the outer layers of the planet's atmosphere as they have a larger influence on the planetesimal's orbit.

density profile towards the center of the planet:

$$T(r) = T_0, \tag{1.95}$$
$$P(r) = P_0 \exp\left[\alpha(R_0/r - 1)\right], \tag{1.96}$$
$$\rho(r) = \rho_0 \exp\left[\alpha(R_0/r - 1)\right]. \tag{1.97}$$

If we substitute (1.95) into (1.92) we get an expression for α:

$$\alpha = \frac{GM\rho_0}{P_0 R_0}. \tag{1.98}$$

Now, assuming that $m = M$, the total mass of the planet, which is a reasonable guess for the outer layers of the planet's atmosphere, we can use equation (1.97) to infer the density profile of the envelope.

At this point, the approximation for the capture radius is obtained by inserting equation (1.97) into equation (18)[22] of Inaba, S., Ikoma, M. (2003):

$$R_{\text{capt}} = \frac{R_0}{1 + \frac{1}{\alpha}\ln\left(\frac{\rho_*}{\rho_0}\right)} \tag{1.100}$$

with

$$\rho_* = \frac{2 r_{\text{p}} \rho_{\text{p}}}{3 D R_{\text{H}}}, \tag{1.101}$$

where $r_{\text{p}}, \rho_{\text{p}}$ are the planetesimal's size and density, and D is the drag coefficient present in equation (11) of Inaba, S., Ikoma, M. (2003).

This type of approximation works good for small planetesimals (typically of the size of 10 meters) and less good for km sized planetesimals (although it is an error of a factor 2), as shown in Figure 1.9.

Detached phase Equation (1.100) that we derived for the attached phase is no longer valid when the planets run out of the gas supply from the disk and as a result, detaches from it. The assumption that we make is that this phase starts when the total mass of helium and hydrogen equals the heavy element mass (this is called the *crossover mass*), that is a phase in which the planetary radius collapses rapidly and then decreases slowly over time. At the crossover mass, the capture radius can be approximated as a constant, and it depends on the ratio between the heavy element mass and helium-hydrogen mass rather than on the runaway gas accretion rate. Furthermore, the capture radius is also independent on the orbital location, as shown in Figure 1.10. The planet's capture radius

[22]
$$r_{\text{p}} = \frac{3}{2}\frac{\rho(R_{\text{c}})}{\rho_{\text{p}}} R_{\text{H}} \tag{1.99}$$

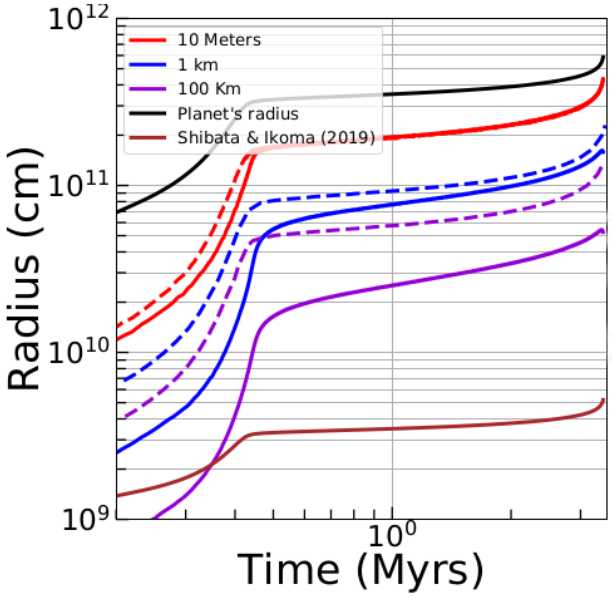

Figure 1.9: Capture radius as a function of time for different planetesimal sizes (red for 10 meter planetesimals, blue for 1 km and violet for 100 km). The black line shows the planet's radius while the brown line shows the commonly used constant-density assumption from Shibata, Ikoma (2019). (Valletta, Helled, 2021)

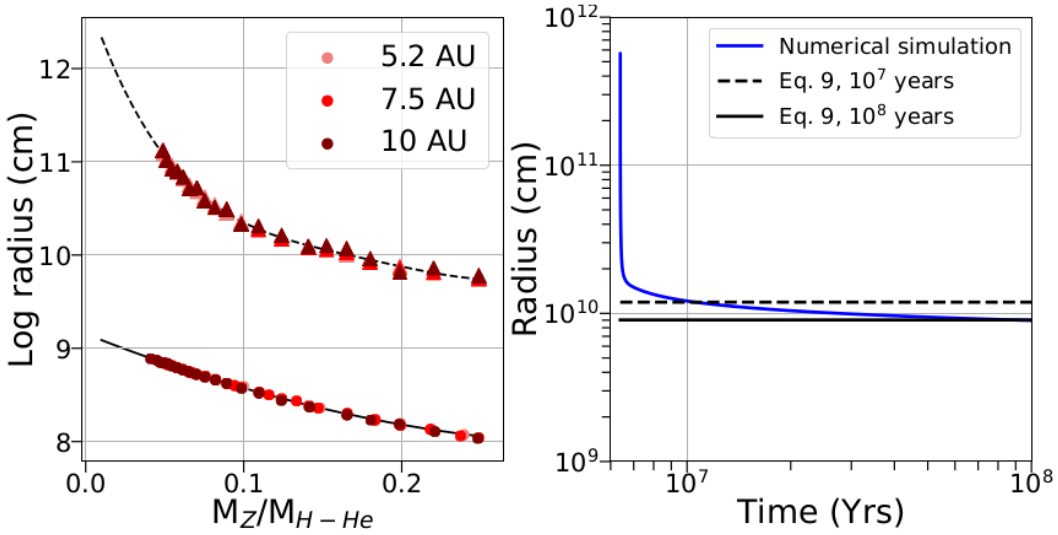

Figure 1.10: The left panel shows the planet's radius as a function of the ratio between heavy element mass and helium-hydrogen mass, with the triangles and dots representing the radius at 10^7 and 10^8 Myrs after the planet's formation. The three different colors represent planets at different orbital locations. From this, we can conclude that the orbital location does not affect the radius. The right panel shows, the planet's radius obtained through numerical simulations (blue line) and through a fit (black lines, solid for 10^7 yrs and dashed for 10^8 yrs) (1.102). From Valletta, Helled (2021)

in the detached phase is better represented by the following numerical fit (Valletta, Helled, 2021),

$$R = \left(\sum_{i=0}^{4} R_i \frac{M_{\rm Z}^i}{M_{\rm H-He}^i} \right) \cdot 10^9 {\rm cm}, \tag{1.102}$$

where the fit parameters are: $R_0 = 12.80662188, 9.15426162$, $R_1 = -50.86303789, -6.74548399$, $R_2 = 382.66267044$, 9.40271959, $R_3 = -1388.57741163$, 0 and $R_4 = 1902.60362959$, 0. Each of the two values represent the fit after 10^7 and 10^8 years of evolution, while the radius between these years can be derived with a logarithmic interpolation between the two values.

Figure 7 in Appendix 4 shows the planetesimal accretion radius we obtained following the recipe of Valletta, Helled (2021).

1.2.3 Pebble accretion

The idea of creating planets via the accretion of small, millimeter to centimeter sized, objects, called pebbles, was first presented by Johansen, Lacerda (2010) to try to solve issues that arise when dealing with giant planets' formation.

In the literature, there are two possible scenarios for the gas-giant formation before pebble accretion:

- **Disk instability scenario**: Gravitational instabilities in the protoplanetary disk excite dense spiral arms which fragment directly into gas-giant planets (Boss, 1997).
- **Core accretion (or nucleated instability) scenario**: Requires the formation of a $10 M_\oplus$ solid core, capable of holding a gaseous atmosphere. When the envelope reaches a mass comparable to the core mass, a run-away accretion of the surrounding gas is triggered (Mizuno, 1980; Pollack et al., 1996).

When we use the Solar System and the observations of exoplanets to check these scenarios, however, we see that both of them have certain limitations.

Formation of gas giants by direct gravitational collapse has been shown to be problematic. At large distances from the host star it becomes increasingly difficult to clump gas with masses below the deuterium burning limit. Additionally, at smaller stellar separations, gas cools too slowly for the spiral arms to fragment into bound clumps. On the other hand, gas-giant formation by core accretion suffers from exceedingly long timescales at wide stellar separations. Indeed, dust infrared emission observations constrain the disk lifetime to around 10^{6-7} yrs, while classical core formation by runaway planetesimal accretion is believed to take more than 10^7 yrs beyond 5 AU, where the planetesimal number densities are low. Furthermore, planetesimals can also undergo scattering and fail to accrete onto the core. Additionally, the formation of the planetesimals itself is problematic, due to the already mentioned formation barriers that need to be overcome. Particle

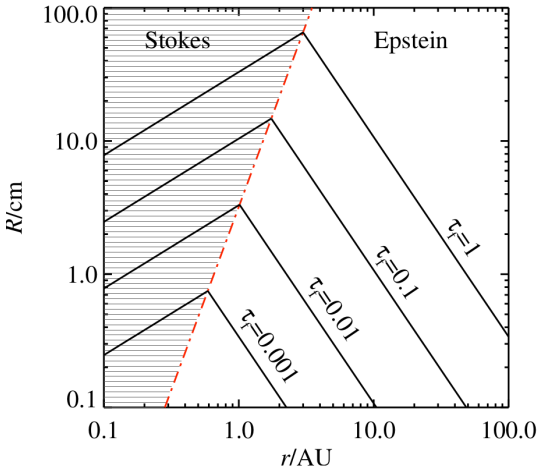

Figure 1.11: Drag regime of particles based on size and distance from the central star. The red dash-dotted line marks the size of the particle $R = 9/4\lambda$ that separates the two regimes. Around 10 AU, a dimensionless friction time τ_f corresponds to cm-sized particles (Lambrechts, M., Johansen, A., 2012).

growth beyond cm-sizes by coagulation is inefficient and radial drift timescales for m-sized boulders are as short as a hundred orbital timescales.

To try to solve the aforementioned problems and explain the observations of gas giants at wide orbital distances, first Johansen, Lacerda (2010) and later Lambrechts, M., Johansen, A. (2012) proposed the accretion of smaller particles, called pebbles, coupled to the gas on approximately orbital timescales. Johansen, Lacerda (2010) numerically found out that pebbles are accreted by the entire Hill sphere of the protoplanet, the region roughly corresponding to the maximal gravitational reach of the core. Dust continuum observations show that the dominant particles in the disk grow up to mm-cm size within 1 Myr. The dynamics of such particles are influenced by the gas and described by the Epstein drag.

These particles react on a friction timescale t_f[23] to the changes in the relative velocity between particles and local gas:

$$\dot{\mathbf{v}}_\mathrm{drag} = -\frac{1}{t_f}(\mathbf{v} - \mathbf{u}) = -\frac{\rho_\mathrm{g} c_\mathrm{s}}{\rho_\bullet R}(\mathbf{v} - \mathbf{u}), \tag{1.103}$$

with the particle- $\mathbf{v}$ and gas velocity $\mathbf{u}$, the radius R and the material density $\rho_\bullet$ of the particle, and the local gas density ρ_g. As we already mentioned in Subsection 1.1.1, the gas rotates at a sub-Keplerian velocity. The azimuthal velocity difference between the gas

[23]Referred to in the previous Section as stopping time?

velocity and the Keplerian orbit normalised to the speed of sound is given by,

$$\frac{v_\mathrm{g} - v_\mathrm{K}}{c_\mathrm{s}} = -\frac{1}{2}\frac{c_\mathrm{s}}{v_\mathrm{K}}\frac{\partial \ln P}{\partial \ln r}. \tag{1.104}$$

Equation (1.104) also shows that pressure bumps occuring in the disk, due to its turbulent nature, can reduce the headwind that the pebbles experience, which in turn causes their radial and azimuthal drift. The relative velocity between particle and core in Keplerian rotation is thus,

$$\Delta v = \frac{\sqrt{4\tau_\mathrm{f}^2 + 1}}{\tau_\mathrm{f}^2 + 1}\eta v_\mathrm{K}. \tag{1.105}$$

The pebbles that are set to accrete onto the core of planets settle vertically on the midplane and have a scale height h_p that is the balance midplane-directed gravity and turbulent diffusion.

As a result of their lower velocity due to the drift, pebbles frequently encounter planetesimals and can accrete on them. Indeed, the drag, which increases with the pebble velocity, can slow some of the pebbles enough to be captured by the gravity of the planetesimal and accrete on it.

The core of the accreting planet can range from the initial mass of a planetesimal to the core of a gas giant. The gravitational parameter of such core is given by,

$$\mu_\mathrm{c} = \frac{GM_\mathrm{c}}{\Omega_\mathrm{K}^2 H^3} = \frac{M_\mathrm{c}}{M_\odot}\left(\frac{H}{r}\right)^{-3} \propto r^{-3/4}. \tag{1.106}$$

With this equation, we can relate the dimensionless gravitational parameter to the orbital radius. The numerical results found by Lambrechts, M., Johansen, A. (2012) are in good agreement with the analytic expressions, indicating the existence of two accretion regimes, one set by the azimuthal and radial particle drift for the lower seed masses and the other, for higher masses, by the velocity at the edge of the Hill sphere. In the former, the optimally accreted particle size increases with core mass, whilst in the latter, the optimal size is centimeters, independent of core mass.

We can model the characteristic interaction radius R_g of a planetesimal (or plotoplanet) of mass M that exerts gravity on a particle passing close to it:

$$R_\mathrm{g} = \frac{GM}{\delta v^2}, \tag{1.107}$$

where δv is the relative speed of the particle.

This gravitational radius will be equated to the Bondi radius R_B if the relative speed is dominated by the sub-Keplerian speed of the particles (equation (1.105)) or to the Hill radius R_H if the relative speed is dominated by the Hill speed $v_\mathrm{H} = \Omega R_\mathrm{H}$. Equating Δv and v_H we get the transition mass between the two regimes:

$$M_\mathrm{t} = \sqrt{\frac{1}{3}}\frac{\Delta v^3}{G\Omega}. \tag{1.108}$$

This transition mass is typically in between the mass of Ceres ($M = 1.5 \cdot 10^{-4} M_\oplus$) and the mass of the Moon ($M = 1.2 \cdot 10^{-2} M_\oplus$), which will lead planetesimals to accrete in the Bondi regime and protoplanets to accrete in the Hill regime. The corresponding transition radius will be given by:

$$R_\mathrm{t} = 1,160\mathrm{km} \left(\frac{r}{5\mathrm{AU}}\right)^{1/2} \left(\frac{\Delta v}{30\mathrm{ms}^{-1}}\right) \left(\frac{\rho_\bullet}{2 \cdot 10^3 \mathrm{kgm}{-3}}\right)^{-1/3}. \tag{1.109}$$

Bondi accretion

In the Bondi regime, the pebble transport is due to the azimuthal and radial drift. If the pebbles are small (St < 0.1), the azimuthal drift is dominant and they move, embedded in the gas, with sub-Keplerian velocity Δv (see equation (1.105)). The Bondi accretion radius is given by (Johansen, Lambrechts, 2017):

$$R_\mathrm{B} = \frac{GM}{\Delta v^2}. \tag{1.110}$$

The pebble accretion radius is then given by the friction time of the pebbles (t_f) relative to the characteristic timescale needed to pass the core $t_\mathrm{B} = R_\mathrm{B}/\Delta v$. Figure 1.12 shows pebble accretion in the Bondi regime. Blue, red, and orange lines mark trajectories of different-sized pebbles as they approach the planetesimal. Blue lines represent large pebbles with big friction times ($t_\mathrm{f} \approx 100 t_\mathrm{B}$), that are scattered by the planetesimal. Red lines mark the trajectories of the optimally accreted pebbles, that typically have friction times of $t_\mathrm{f} \approx 10 t_\mathrm{B}$. Finally, orange lines mark the trajectory of strongly coupled pebbles (pebbles for which the friction time is shorter than t_B), which we see are accreted only in the case of small impact parameters.

Hill accretion

In the Hill regime, pebbles approach the protoplanet with Keplerian shear flow, i.e., inner orbits have faster velocities and outer orbits have slower velocities. The timescale to pass the Hill radius is $t_\mathrm{H} = 1/\Omega$ independently from the mass of the protoplanet, therefore, the accretion radius of the protoplanet is determined directly by the Stokes number of the pebbles. The Hill radius is set by the gravitational competition between the acceleration towards the core and the stellar tidal field in the radial direction, and can be expressed as:

$$R_\mathrm{H} = \left(\frac{GM}{3\Omega^2}\right)^{1/3}. \tag{1.111}$$

At a separation R_H from the core, the orbital time around the core approximately equals the orbital time around the star, $2\pi\Omega_\mathrm{K}^{-1}$. The Hill sphere's radius grows linearly with the

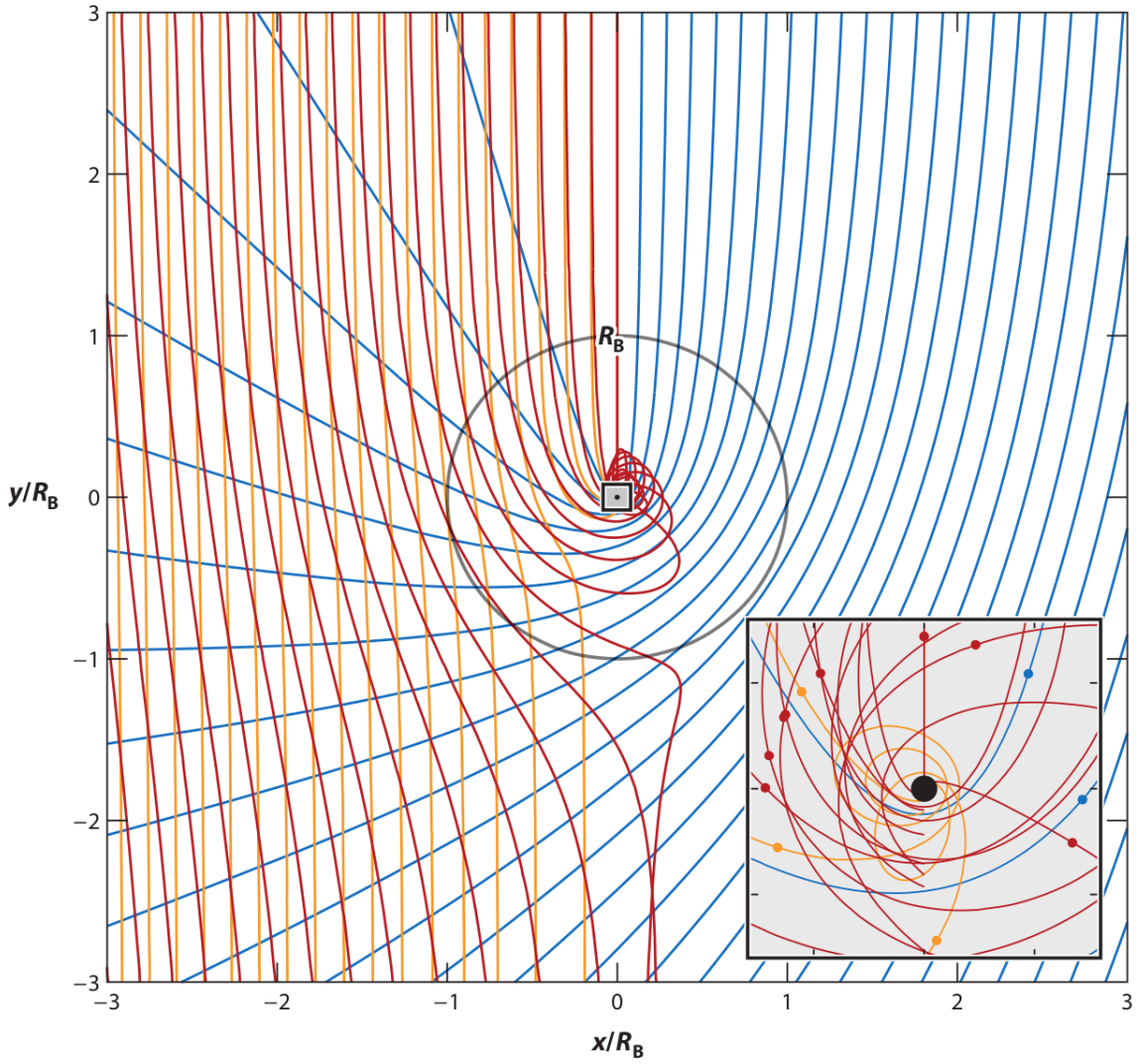

Figure 1.12: Trajectories of pebbles approaching a planetesimal (from above with sub-Keplerian speed) in the Bondi accretion regime, with axes normalized to the Bondi radius. Very large pebbles (blue lines) that have big friction times ($t_\mathrm{f} \approx 100 t_\mathrm{B}$) are scattered by the protoplanet because of their weak drag. The red lines represent the trajectories of the optimally accreted pebbles, that typically have friction times of $t_\mathrm{f} \approx 10 t_\mathrm{B}$. Orange trajectories show the strongly coupled pebbles ($t_\mathrm{f}/t_\mathrm{B} = 0.1$), that are accreted from smaller impact parameters only. (Johansen, Lambrechts, 2017)

orbital radius $R_{\rm H} \propto R$, placing more material in the gravitational region of influence of the core.

Figure 1.13 shows the trajectories of pebbles in the Hill regime. again we mark with the blue lines the weakly coupled particles, that are scattered by the planetesimal, and with the red and orange lines the optimally and strongly coupled particles respectively. These two classes of particles are instead accreted by most of the Hill radius.

Pebble accretion rates

The pebble accretion rate depends on the friction time of the pebbles and on the azimuthal flux of pebbles ($\rho_{\rm peb}\delta v$) through the cross section of the planet's accretion sphere ($\pi R_{\rm acc}^3$).

We distinguish two different cases: 2D and 3D accretion. In the case of 2D pebble accretion, the planetary accretion radius is larger than the midplane pebble scale height of the disk, so that the planet can accrete from the full pebble flux passing the planetary orbit. This is not the case in the 3D pebble accretion regime, where the planetary accretion radius is smaller than the pebble scale height and only a fraction of the pebble flux passing the planet can contribute to the accretion.

The most general expression for 2D and 3D accretion rates are given by:

$$\begin{aligned} \dot{M}_{\rm peb,2D} &= 2R_{\rm acc}\Sigma_{\rm peb}\delta v, \\ \dot{M}_{\rm peb,3D} &= \pi R_{\rm acc}^2\rho_{\rm peb}\delta v, \end{aligned} \tag{1.112}$$

where $R_{\rm acc}$ is the accretion radius (will be either Bondi or Hill radius depending on the regime), $\Sigma_{\rm peb}$ and $\rho_{\rm peb}$ column and midplane densities and $\delta v = \Delta v + \Omega R_{\rm acc}$ approach velocity.

Ormel, C. W., Klahr, H. H. (2010) and Lambrechts, M., Johansen, A. (2012) found the following limiting behaviours:

$$R_{\rm acc} = \left(\frac{4\tau_{\rm f}}{t_{\rm B}}\right)^{1/2} R_{\rm B} \qquad \text{Bondi,} \tag{1.113}$$

$$R_{\rm acc} = \left(\frac{\Omega\tau_{\rm f}}{0.1}\right)^{1/3} R_{\rm H} \qquad \text{Hill,} \tag{1.114}$$

The criterion for the transition between 2D and 3 D accretion is given by (Morbidelli et al., 2015),

$$H_{\rm peb} < \frac{2\sqrt{2\pi}R_{\rm acc}}{\pi}, \tag{1.115}$$

where $H_{\rm peb} = H_{\rm gas}\sqrt{\alpha_z {\rm St}}$ is the pebble scale height.

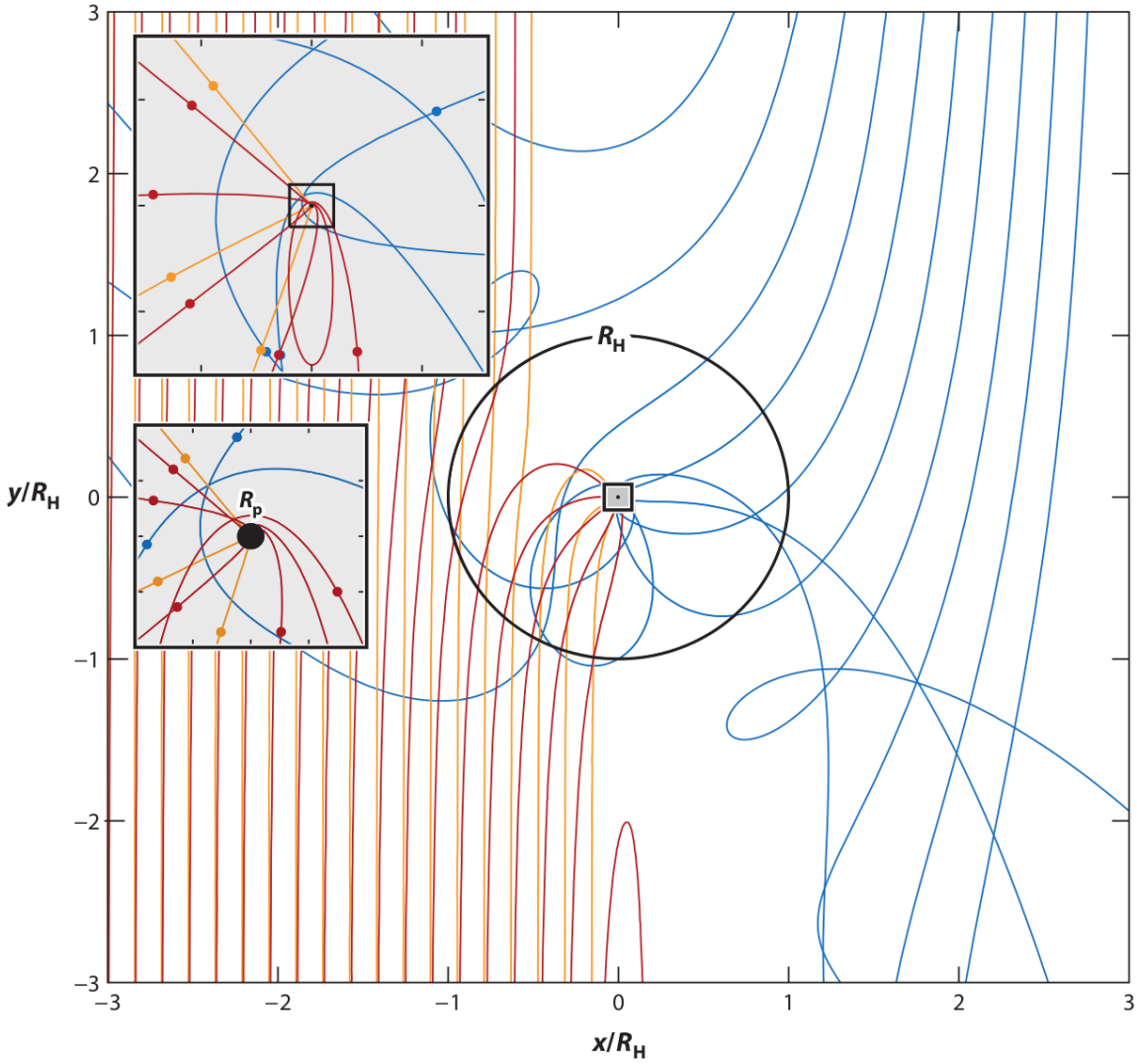

Figure 1.13: Trajectories of pebbles approaching a planetesimal (from above with sub-Keplerian speed) in the Hill accretion regime, with axes normalized to the Hill radius. Very large pebbles (blue lines) that are coupled to the gas on a timescale much longer than the orbital one are scattered by the protoplanet. The red lines represent the trajectories of the optimally accreted pebbles (St = 1), while orange trajectories show the strongly coupled pebbles (St = 0.1). Both classes of particles are accreted from most of the Hill radius. The grey boxes show a close up of the protoplanet, since its radius is just 0.001 times the Hill radius. (Johansen, Lambrechts, 2017)

1.2.4 Gas accretion

We will consider the forming planet to undergo gas accretion once it has reached pebble isolation mass, i.e., once the solid accretion stopped.

The gas accretion rate is given by the minimum between accretion rates of Ikoma et al. (2000) and Machida et al. (2010), and by the gas the disk can viscously provide into the horseshoe region after the planet has emptied the horseshoe region (Ndugu et al., 2020a).

Ikoma et al. (2000) gas accretion rate is given by:

$$\dot{M}_{\rm g,Ikoma} = \frac{M}{\tau_{\rm KH}}, \tag{1.116}$$

where $\tau_{\rm KH}$ is the Kevin-Helmholtz contraction rate,

$$\tau_{\rm KH} = 10^3 \left(\frac{M_{\rm c}}{30 M_\oplus}\right)^{-2.5} \left(\frac{\kappa_{\rm env}}{0.05 {\rm cm^2 g^{-1}}}\right) {\rm year}, \tag{1.117}$$

with $M_{\rm c}$ core mass.

Machida et al. (2010) accretion rate is given by the minimum between:

$$\begin{aligned} \dot{M}_{\rm g,Machida,low} &= 0.83 \Omega_{\rm K} \Sigma_{\rm gas} H_{\rm gas}^2 \left(\frac{R_{\rm H}}{H_{\rm gas}}\right)^{9/2}, \\ \dot{M}_{\rm g,Machida,high} &= 0.14 \Omega_{\rm K} \Sigma_{\rm gas} H_{\rm gas}^2. \end{aligned} \tag{1.118}$$

Once the planet opens a gap in the disk, the gas accretion is limited by the amount of gas that the disk can supply, which is regulated by the supply rate:

$$\dot{M}_{\rm disk} = -2\pi r \Sigma_{\rm gas} u_{\rm gas}, \tag{1.119}$$

where $u_{\rm gas}$ is the gas velocity. Furthermore, we also need to take into account the horseshoe depletion rate, that expresses the loss of mass from the horseshoe region:

$$\dot{M}_{\rm HS} = \frac{M_{\rm HS}}{2 T_{\rm HS}}, \tag{1.120}$$

with $M_{\rm HS}$ being the mass of the horseshoe region and the synodic period $T_{\rm HS} = 2\pi/\Omega_{\rm HS}$ at its border, where the half width $\Omega_{\rm HS} = 1.5\pi\Omega r_{\rm HS}/a_p$, with $r_{\rm HS} = x_s a_p$ where x_s is taken from equation (48) in Paardekooper et al. (2010).

Summarising, the gas accretion rate is given by the minimum between these three terms:

$$\dot{M}_{\rm gas} = \min(\dot{M}_{\rm g,Ikoma}, \dot{M}_{\rm g,Machida}, \dot{M}_{\rm disk} + \dot{M}_{\rm HS}). \tag{1.121}$$

1.3 Planet disk interaction

During the planet formation process and soon after that, the disk still has not dissipated, therefore the planet strongly interacts with it. In particular, the planet exchanges angular momentum with the disk, modifying the disk structure and its own orbital parameters like the semi-major axis and the eccentricity of the orbit.

As it grows and evolves, the planet gravitationally attracts material, carving a gap in the disk and cleaning its orbit. This process is interesting because it can clearly be observed through sub-millimeter observations.

Another very interesting process resulting from the planet-disk interaction and exchange of angular momentum is planetary migration. We will analyse the type of migrations in the following Section.

1.3.1 Torque

The exchange of angular momentum between the planet and the disk is the main mean of mutual interaction.

The analytical expression for the torque exerted by the planet on the disk can be derived using the impulse approximation as proposed in Lin, Papaloizou (1979). The total torque that the planet exerts on the disk:

$$\Gamma_{\rm p} = -\frac{8}{9}\left(\frac{M_{\rm p}}{M_*}\right)^2 \int_{R_0}^{\infty} \text{signum}(R-a_{\rm p})\Omega^2(R)\Sigma_{\rm gas}\left(\frac{a_{\rm p}}{R-a_{\rm p}}\right)^4 R\,dR. \tag{1.122}$$

Considering a power law for the surface density ($\Sigma_{\rm gas}(R) = \Sigma_{\rm gas,0}(r/a_{\rm p})^{-1}$ and $R_0 \approx a_{\rm p}$) we can express the torque that the outer disk exerts on the planet at a distance $a_{\rm p}$ with,

$$\Gamma_{\rm p} \approx \left(\frac{M_{\rm p}}{M_*}\right)^2 \Omega_{\rm p}^2(R) a_{\rm p}^4 \Sigma_0 \left(\frac{a_{\rm p}}{R-a_{\rm p}}\right)^3. \tag{1.123}$$

We can observe that the torque depends on the square of the mass ratio and that it reduces with the distance from the planet.

The disk exerts on the planet the following torques:

- The external part of the disk generates a negative torque on the planet causing it to migrate inward.
- The internal part of the disk generates a positive torque on the planet causing it to migrate outward.

Vice versa, the planet exerts on the disk the following torques:

- A negative torque on the inner part of the disk, slowing its rotation down.
- A positive torque on the outer part of the disk, accelerating it.

These two effects combined are responsible for the gap opening process.

Thermal torque

Recent studies (Lega et al., 2014; Benítez-Llambay et al., 2015; Masset, 2017) have shown that the thermal torque, originating from density perturbations close to the planet due to thermal heat exchange between the planet and the disk also plays an important role in the orbital evolution of the planet.

The thermal torque is the result of a cooling and heating torque, due to bombardment and ablation of solids. It is described in Masset (2017) and we used the accretion luminosity given by Chrenko, O. et al. (2017). This torque, depending on the accretion efficiency of the planet, might lead to outward migration.

Dynamical torque

The last type of torque to be considered when dealing with planet-disk interaction is the dynamical torque, originating from feedback processes of the migration rate of the planet on the torque. It can modify the semi-major axis of the planet as (Paardekooper, 2014):

$$\frac{da_\mathrm{p}}{dt} = \frac{a_\mathrm{p}}{\tau_M} = 2a_\mathrm{p}\Theta\frac{\Gamma_\mathrm{p}}{J_\mathrm{p}}, \tag{1.124}$$

with the numerical parameter, Θ that determines the effects of migration onto the migration rate (equations 31, 32 from Paardekooper (2014)). The dynamical torque can help to significantly slow down the inward migration of low-mass planets, preventing large-scale migration of planets.

1.3.2 Gaps

As we already mentioned in Section 1.3.1, planets exchange angular momentum with the disk. The torque exerted from the planet on the disk results in the creation of a gap in the disk. Generally, if the planet is sufficiently massive, it is able to open a gap in the disk. In order to do so, it is required that the torque dominates over the viscous forces, which results in a condition that the mass ratio needs to satisfy, known as the viscosity criterion:

$$\left(\frac{M_\mathrm{p}}{M_*}\right)^2 > \alpha_\mathrm{ss}\left(\frac{h_\mathrm{p}}{R(a_\mathrm{p})}\right)^2\left(\frac{\Delta}{a_\mathrm{p}}\right)^3. \tag{1.125}$$

The dimension of the opened gap, however, needs to be bigger than the scale height of the disk in the planet location[24] and the planet's Hill radius. Using the condition $R_H > h_\mathrm{p}$ (Lin, Papaloizou, 1993), we get another criterion for the gap opening, the thermal[25]

[24]Because the pressure gradients are unstable on a smaller length scale and the gap would collapse

[25]Is called thermal because it provides a constraint on the planet's temperature in order for it to be able to open a gap.

criterion:

$$\frac{M_\mathrm{p}}{M_*} > 3\left(\frac{h_\mathrm{g}}{R_\mathrm{p}}\right)^3. \tag{1.126}$$

Crida et al. (2006) proposed a criterion that joins the viscosity and thermal criteria for the planet to be able to open a gap:

$$\frac{3}{4}\left(\frac{h_\mathrm{p}}{R(a_\mathrm{p})}\right)\left(\frac{3M_*}{M_\mathrm{p}}\right)^{1/3} + \frac{50\nu_\mathrm{p}}{\Omega_\mathrm{p}a_\mathrm{p}^2}\left(\frac{M_*}{M_\mathrm{p}}\right) < 1. \tag{1.127}$$

The gap opening is caused, as we already saw, by gravitational interaction between the disk and the planet. However, it can be aided by gas accretion (Crida, Bitsch, 2017; Bergez-Casalou, C. et al., 2020). A gap is opened by gravity when:

$$P = \frac{3}{4}\frac{H_\mathrm{gas}}{R_\mathrm{H}} + \frac{50}{q\mathrm{Re}} \leq 1, \tag{1.128}$$

with Hill radius R_H, the Reynolds number Re. The depth of the gap is given by (Crida, Morbidelli, 2007):

$$f(P) = \begin{cases} \frac{P-0.54}{4} & P < 0.4646 \\ 1.0 - \exp\left(-\frac{P^{3/4}}{3}\right) & \text{otherwise.} \end{cases} \tag{1.129}$$

The contribution to the gap depth by gas accretion is given by f_A:

$$f_\mathrm{A} = 1 - \frac{\dot{M}_\mathrm{gas}\delta t}{f(P)\hat{M}_\mathrm{HS}}, \tag{1.130}$$

with $\hat{M}_\mathrm{HS}$ mass inside the horseshoe region in absence of gas accretion and gap, given by:

$$\hat{M}_\mathrm{HS} = 2\pi a_p r_\mathrm{HS}\hat{\Sigma_\mathrm{HS}}, \tag{1.131}$$

where $\hat{\Sigma_\mathrm{HS}}$ is the horseshoe gas density.

The total gap depth will, therefore, be given by:

$$f_\mathrm{gap} = f(P)\, f_\mathrm{A}. \tag{1.132}$$

1.3.3 Migration

Planet migration is the direct result of the exchange of angular momentum between the planet and the disk. We identify two different types of migration, depending on the mass of the planet and the local properties of the gas.

Generally, we can describe the change in orbital position of the planet (Armitage, 2013) as,

$$\dot{a}_\mathrm{p} = \frac{da_\mathrm{p}}{dt} = \frac{a_\mathrm{p}}{\tau_M} = 2a_\mathrm{p}\frac{\Gamma_\mathrm{p}}{J_\mathrm{p}} \tag{1.133}$$

with τ_M migration timescale and Γ_p torque that acts on the planet.

Type I migration

Type I migration is the scenario in which the planet is completely embedded in the disk. This can happen either because the disk has a particularly high viscosity, which makes it very difficult for the planet to carve a gap, or because the planet does not have enough mass to carve the gap.

In this case, the total torque that acts on the planet is the sum of the Lindblad and co-rotation torques. Whether the planet migrates inward or outward depends on the total angular momentum that has been exchanged (if the planet loses angular momentum it migrates inward, vice versa if it gains angular momentum it migrates outward). To model the type I migration we use the recipe in Paardekooper et al. (2010) that includes the Lindblad as well as the barotropic and entropy related co-rotation torques.

Type II migration

If the planet is sufficiently massive ($\approx M_J$), it is able to carve a gap in the disk. In this case the material that is orbiting inside the planet tends to lose angular momentum drifting inward, while the material external to the orbit gains angular momentum and drift outward, opening the gap. Type II migration is more inefficient and slower than type I because the angular momentum exchange is not as efficient as in the type I case. Furthermore, the migration in this case is directly linked to the gap. The mass limit for which type II migration occurs can be estimated comparing the exchange of angular momentum that leads to gap opening and viscous forces that always contrast the gap opening. Therefore, the timescale that regulates the type II migration is the viscous one:

$$\tau_{\rm visc} = \frac{a_p^2}{\nu}. \tag{1.134}$$

Contrary to what happens for type I migration, the type II migration velocity seems to be mass independent, although inertia of very massive planets may slow down the process. This happens if $M > 4\pi\Sigma_{\rm gas}a_p^2$, that leads to the migration timescale of:

$$\tau_{\rm typeII} = \tau_\nu \cdot \max\left(1, \frac{M}{4\pi\Sigma_{\rm gas}a_p^2}\right), \tag{1.135}$$

that leads to a slower inward migration for more massive planets.

Chapter 2

The model

2.1 CHEMCOMP code

2.1.1 Overview of the model and key assumptions

Although there are many models that deal with the planetary core formation process, they usually lack a proper treatment of the chemical composition and of the different molecular species in the disk. The model used in the CHEMCOMP code aims to trace the chemical composition of the disk and a planet during its formation process, in order to investigate the effects of inward drifting and evaporation of pebbles on the planet's atmospheric composition, with particular focus on the C/O ratio, heavy element content and volatile-to-refractory ratio.

Figure 2.1 shows the main idea behind the model, underlying how inward drift and evaporation of volatile-rich pebbles can affect the disk (and therefore subsequently the planet's) composition.

We can see from the top panel of Figure 2.1, that the chemical composition of the disk will depend on two main mechanisms:

- Inward pebble drift and subsequent evaporation, that enriches the gas in the inner region in different species[1],
- Outward diffusion and re-condensation of the gas, that will enrich the pebble surface density in the outer region of the disk.

The second panel of Figure 2.1 shows a planetary seed planted inside the disk at a certain distance from the central star that accretes pebbles and migrates at the same time. Depending on its starting position the planet will have a dry (if it is planted inside the water evaporation front) or icy (if it is planted outside) core. The bottom panel shows the

[1]Figure 2.1 illustrates the mechanism of the water-ice line, but it works in the same way for every species evaporation line.

planet growing until it reaches pebble isolation mass[2] and is no longer able to accrete pebbles anymore (Section 1.2.3), thus it switches to gas accretion (Section 1.2.4). Depending on the position of the planet, the accreted atmosphere will have a different composition. Figure 2.1 shows this idea by considering icy pebbles and the water evaporation line, but the same reasoning applies to all the chemical species we consider in the code.

Key Assumptions

The main aim of this Section is to specify the assumptions used in the CHEMCOMP code.

Dust Growth The dust growth is modeled using the two-population approach of Birnstiel, T. et al. (2012) and is limited by fragmentation, drift, and drift-induced fragmentation.

Small dust particles have low friction times and are therefore strongly coupled to the gas, whereas large particles have large friction times and therefore only couple weakly to the gas. Due to this headwind, as already explained in Section 1.1.2, dust grains will spiral inward with the radial velocity u_{Z}:

$$u_{\mathrm{Z}} = \frac{1}{1+\mathrm{St}^2} u_{\mathrm{gas}} - \frac{2}{\mathrm{St}^{-1} + St} \Delta v, \tag{2.1}$$

thus, growth from small to large grains implies an increase in the radial dust velocity. When the velocity of the dust grains exceeds a certain velocity boundary (Birnstiel, T. et al., 2009), the dust will fragment upon collision.

We get the pebble surface density from the solid surface density (Σ_{Z}) multiplying it by a factor f_m taken from Birnstiel, T. et al. (2012):

$$\Sigma_{\mathrm{peb}} = f_m \cdot \Sigma_{\mathrm{Z}}, \tag{2.2}$$

with $f_m = 0.97$ in the drift limited case and $f_m = 0.75$ in the fragmentation limited case.

The mass averaged dust velocity that we need for the dust transport, is given by:

$$\bar{u}_{\mathrm{Z}} = (1 - f_m) u_{\mathrm{dust}} - f_m u_{\mathrm{peb}}. \tag{2.3}$$

In this work we will ignore the bouncing and charging barrier.

Compositions The first assumption we are working with is that the original chemical composition of the disk is similar to the one of the host star. The chemical model used in the code is the one presented in Bitsch, Bertram, Battistini, Chiara (2020). Since the disk temperature is dependent on the orbital distance, the composition of dust and gas will also depend on that distance. The elements are distributed into molecules based on Bitsch, Bertram, Battistini, Chiara (2020), as shown in Figure 2.2. As already mentioned,

[2]It is the critical mass for which the planet generates a pressure bump that prevents pebble accretion.

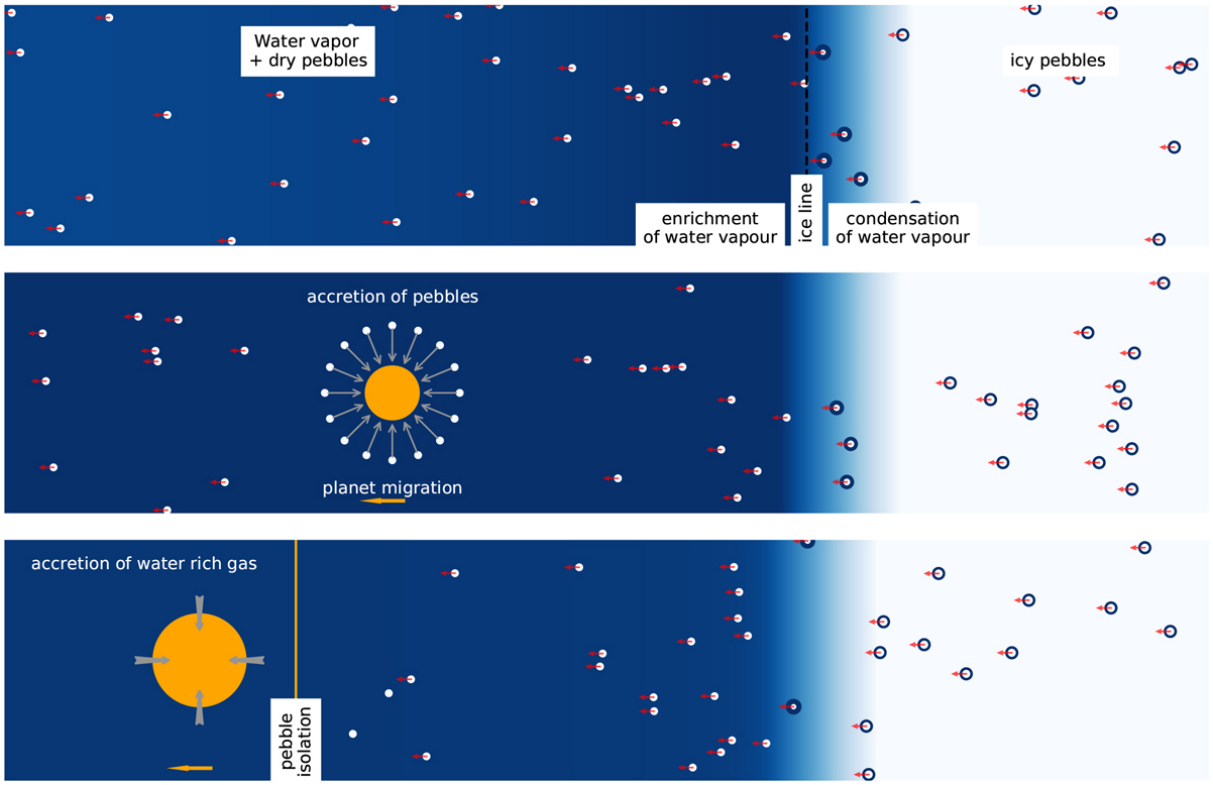

Figure 2.1: The top panel shows dust particles that grow into pebbles and migrate towards the star. Icy pebbles that cross the water ice line (black dashed line) evaporate and their water content enriches the gas with water vapor. On the other hand, water vapor that is drifting outward condenses into pebbles when crossing the ice line, increasing the pebble water content in the outer part of the disk. The middle panel shows the formation of the core of the planet via pebble accretion while the planet migrates inward (outward migration is also possible). Depending on the formation path, the core composition can be icy or dry, in this case, the core would be water poor. The bottom panel shows the stage at which the planet is heavy enough to reach pebble isolation mass and form a pressure bump, stopping the pebbles' accretion. At this point the planet will start to accrete gas that is enriched with water vapor. The water content of the disk (in solid or gaseous form) is color-coded, where a darker color indicates a higher water content. The same reasoning applies to any other evaporation front (not only the ice one). Figure from Schneider, Bitsch (2021)

Species (Y)	$T_{\rm cond}$ [K]	$v_{\rm Y,\ no\ C}$	$v_{\rm Y,\ with\ C}$
CO	20	0.45 × C/H	0.45 × C/H
N_2	20	0.9 × N/H	see $v_{\rm Y,\ no\ C}$
CH_4	30	0.45 × C/H	0.25 × C/H
CO_2	70	0.1 × C/H	0.1 × C/H
NH_3	90	0.1 × N/H	see $v_{\rm Y,\ no\ C}$
H_2S	150	0.1 × S/H	see $v_{\rm Y,\ no\ C}$
H_2O	150	O/H - (3 × $MgSiO_3$/H + 4 × Mg_2SiO_4/H + CO/H + 2 × CO_2/H + 3 × Fe_2O_3/H + 4 × Fe_3O_4/H + VO/H + TiO/H + 3×Al_2O_3 + 8×$NaAlSi_3O_8$ + 8×$KAlSi_3O_8$)	see $v_{\rm Y,\ no\ C}$
Fe_3O_4	371	(1/6) × (Fe/H - 0.9 × S/H)	see $v_{\rm Y,\ no\ C}$
C (carbon grains)	631	0	0.2 × C/H
FeS	704	0.9 × S/H	see $v_{\rm Y,\ no\ C}$
$NaAlSi_3O_8$	958	Na/H	see $v_{\rm Y,\ no\ C}$
$KAlSi_3O_8$	1006	K/H	see $v_{\rm Y,\ no\ C}$
Mg_2SiO_4	1354	Mg/H - (Si/H - 3×K/H - 3×Na/H)	see $v_{\rm Y,\ no\ C}$
Fe_2O_3	1357	0.25 × (Fe/H - 0.9 × S/H)	see $v_{\rm Y,\ no\ C}$
VO	1423	V/H	see $v_{\rm Y,\ no\ C}$
$MgSiO_3$	1500	Mg/H - 2×(Mg/H - (Si/H - 3×K/H - 3×Na/H))	see $v_{\rm Y,\ no\ C}$
Al_2O_3	1653	0.5×(Al/H - (K/H + Na/H))	see $v_{\rm Y,\ no\ C}$
TiO	2000	Ti/H	see $v_{\rm Y,\ no\ C}$

Figure 2.2: Condensation temperatures for molecules (Lodders, 2003) and volume mixing ratios $v_{\rm Y}$ for species. The volume mixing ratios are adopted as a function of the disk elemental abundances. These results apply the model without pure carbon grains.

the code takes different evaporation lines into account, therefore each species, Y, will be available in either solid form (before crossing its evaporation line) or in gaseous form (after crossing the evaporation line).

In protoplanetary disks, sulfur is mainly present in refractory form. Nitrogen is mainly locked into N_2, with a small fraction in NH_3. Ti, Al, K, Na, V are still included in this model because they can be observed in the atmospheres of hot Jupiters, although they are not abundant in disks and therefore do not significantly contribute to the planetary accretion rates.

We can define the elemental number ratio of two species X_1, X_2 as:

$$\frac{X_1}{X_2} = \frac{m_{X_1}}{m_{X_2}} \frac{\mu_{X_2}}{\mu_{X_1}}, \tag{2.4}$$

with mass fraction $\mu_{X_{1,2}}$, $\mu_{X_{1,2}}$ of element and atomic mass of element 1 and 2, respectively.

The change of molecular weight[3] due to evaporation of drifting pebbles that increase the water vapor in the disk is considered.

The pebble density for the icy species ($H_2O, H_2S, NH_3, CO_2, N_2, CO$) is $\rho_{\bullet,\mathrm{ice}} = 1\,\mathrm{gcm}^{-3}$, the one for the refractories is $\rho_{\bullet,\mathrm{ref}} = 3\,\mathrm{gcm}^{-3}$, while the exact pebble density is dynamically computed during the simulation as:

$$\rho_\bullet = (m_{\mathrm{ref}} + m_{\mathrm{ice}}) \left(\frac{m_{\mathrm{ref}}}{\rho_{\bullet,\mathrm{ref}}} + \frac{m_{\mathrm{ice}}}{\rho_{\bullet,\mathrm{ice}}} \right)^{-1}. \tag{2.5}$$

Viscous evolution For the theoretical background of the disk's viscous evolution see Section 1.1.1. Considering the inward drift of pebbles, the evolution of the solid surface density becomes (Birnstiel et al., 2010):

$$\frac{\partial \Sigma_{\mathrm{Z,Y}}}{\partial t} + \frac{1}{r} \frac{\partial}{\partial r} \left(r \left(\Sigma_{\mathrm{Z,Y}} \cdot \bar{u}_{\mathrm{Z}} - \frac{\partial}{\partial r} \left(\frac{\Sigma_{\mathrm{Z,Y}}}{\Sigma_{\mathrm{gas}}} \right) \cdot \Sigma_{\mathrm{gas}} \nu \right) \right) = -\dot{\Sigma}_{\mathrm{Y}} - \dot{\Sigma}_{\mathrm{Y}}^{\mathrm{acc,peb}}, \tag{2.6}$$

where $\bar{u}_{\mathrm{Z}}$ is given by equation (2.3), $\dot{\Sigma}_{\mathrm{Y}}^{\mathrm{acc,peb}}$ is the source term that describes the reduction of accreted pebbles by the dust surface density in the grid cell of the planet and $\dot{\Sigma}_{\mathrm{Y}}$ is the source term that accounts for pebble evaporation and condensation and is given by:

$$\dot{\Sigma}_{\mathrm{Y}} = \begin{cases} \dot{\Sigma}_{\mathrm{Y}}^{\mathrm{evap}} & r < r_{\mathrm{ice,Y}} \\ \dot{\Sigma}_{\mathrm{Y}}^{\mathrm{cond}} & r \geq r_{\mathrm{ice,Y}} \end{cases} \tag{2.7}$$

where $\dot{\Sigma}_{\mathrm{Y}}^{\mathrm{evap}}$ and $\dot{\Sigma}_{\mathrm{Y}}^{\mathrm{cond}}$ are the evaporation and condensation source terms for each species mentioned in the two surface density evolution equations (1.18) and (2.6). To model the

[3]It can lead to an increase from 2.3 up to 4, if the disk is heavily enriched in vapor.

condensation term, we assume the gas only condensates when it sticks to the surface of existent solids, with efficiency ε_p:

$$\dot{\Sigma}_{\mathrm{Y}}^{\mathrm{cond}} = \frac{3\varepsilon_p}{2\pi\rho_\bullet}\Sigma_{\mathrm{gas,Y}}\left(\frac{\Sigma_{\mathrm{Z}}}{a_{\mathrm{dust}}} + \frac{\Sigma_{\mathrm{peb}}}{a_{\mathrm{peb}}}\right)\Omega_{\mathrm{K}}\sqrt{\frac{\mu}{\mu_{\mathrm{Y}}}}, \tag{2.8}$$

with μ_{Y} being the mass of a molecule of species Y in proton masses, a_{dust} and a_{peb} the particle sizes of the small and large dust distribution.

To get an expression for the evaporation term, we assume the flux of solids that drifts through the evaporation line is evaporated into the gas within $1 \cdot 10^{-3}$ AU,

$$\dot{\Sigma}_{\mathrm{Y}}^{\mathrm{evap}} = \frac{\Sigma_{\mathrm{Z,Y}} \cdot u_{\mathrm{Z}}}{1 \cdot 10^{-3}\mathrm{AU}}. \tag{2.9}$$

In order to allow for mass conservation, we require that no more than 90% of the local surface density is evaporated or condensed in one time step.

Accretion As illustrated in Figure 2.1, a planetary embryo is planted at a certain location in the disk, and it grows through pebble (Section 1.2.3) and planetesimal (Section 1.2.2) accretion.

Once the planet is large enough to create a pressure bump in the gas surface density, pebble accretion stops, because pebbles are hindered from reaching the planet. This occurs at the pebble isolation mass M_{iso} (Morbidelli, A., Nesvorny, D., 2012; Lambrechts, M. et al., 2014), where we follow the pebble isolation mass from Bitsch, Bertram et al. (2018).

Once pebble isolation mass is reached, the envelope contraction and accretion follows (Section 1.2.4).

An important assumption we use is that as long as $M < M_{\mathrm{iso}}$ holds true, the mass actually accreted by the core is 90% of the total accreted mass, while the remaining 10% constitutes the primary envelope.

This approach is used to account for pebble evaporation into the planetary envelope during core buildup in a simplified way. The initial growth during the core buildup in our model is thus simply described via,

$$\begin{aligned} \dot{M}_{\mathrm{core}} &= 0.9\dot{M}_{\mathrm{peb}} \\ \dot{M}_{\mathrm{env}} &= 0.1\dot{M}_{\mathrm{peb}}. \end{aligned} \tag{2.10}$$

After the pebble isolation mass is reached, all material is accreted into the planetary envelope.

Gap profile The gap profile in the code is modeled using an approach with varying viscosity to mimic the effect of a pressure bump caused by a growing planet (e.g Pinilla,

Paola et al. (2021)). The viscous parameter in equation (2.6) is given at the planet's location by

$$\alpha = \alpha / N(r), \tag{2.11}$$

where $N(r)$ is a numerical factor that describes the gap profile, approximated by a Gaussian distribution peaked around the planet's location:

$$N(r) = 1 - [1 - f_{\text{gap}}] \exp\left((0.5 \left[\frac{(r - a_p)}{\sigma} \right]^2 \right), \tag{2.12}$$

where the width is given by the horseshoe width

$$\sigma = \frac{2 r_{\text{HS}}}{2\sqrt{2\log(2)}}. \tag{2.13}$$

The migration and accretion rate of the planet depends on the unperturbed disk, therefore, in the code the quantities are interpolated to the planetary position by excluding the gap (i.e, only the cells in which $N(r) < 1\%$ are used).

2.1.2 Operating principle

To study the effect of planetesimal accretion on the atmospheric composition of the planet we used the CHEMCOMP[4] code presented in Schneider, Bitsch (2021). This is a 1-dimensional semi-analytical model able to simulate the evolution of a disk and the growth of a single planet, tracing its chemical composition. To do so, the code is divided into two main modules.

- **Disk module**: All the disk quantities are defined on a logarithmic spaced grid with $N = 500$ cells between a defined inner radius R_{in} and R_{out} that can be set as parameters. This module deals with the formation of pebbles, dynamics of gas and pebbles (Section 1.1.1) and computes the temperature profile of the disk, as well as the temperature-dependent compositions of gas and pebbles by including the effects of the existence of evaporation lines.

- **Planet module**: This module handles the growth (Section 1.2) and migration (Section 1.3.3) of a single planet. It also acts as a supervisor of the disk module, collecting the matter available in the disk.

Figure 2.3 shows the operating principle of CHEMCOMP. There are input parameters for both the disk module, such as mass of the disk, inner and outer radius, dust-to-gas ratio etc., and for the planet module, such as position and the time at which the planetary seed is planted.

[4]The CHEMCOMP code is an adapted version of the unpublished code DISKLAB

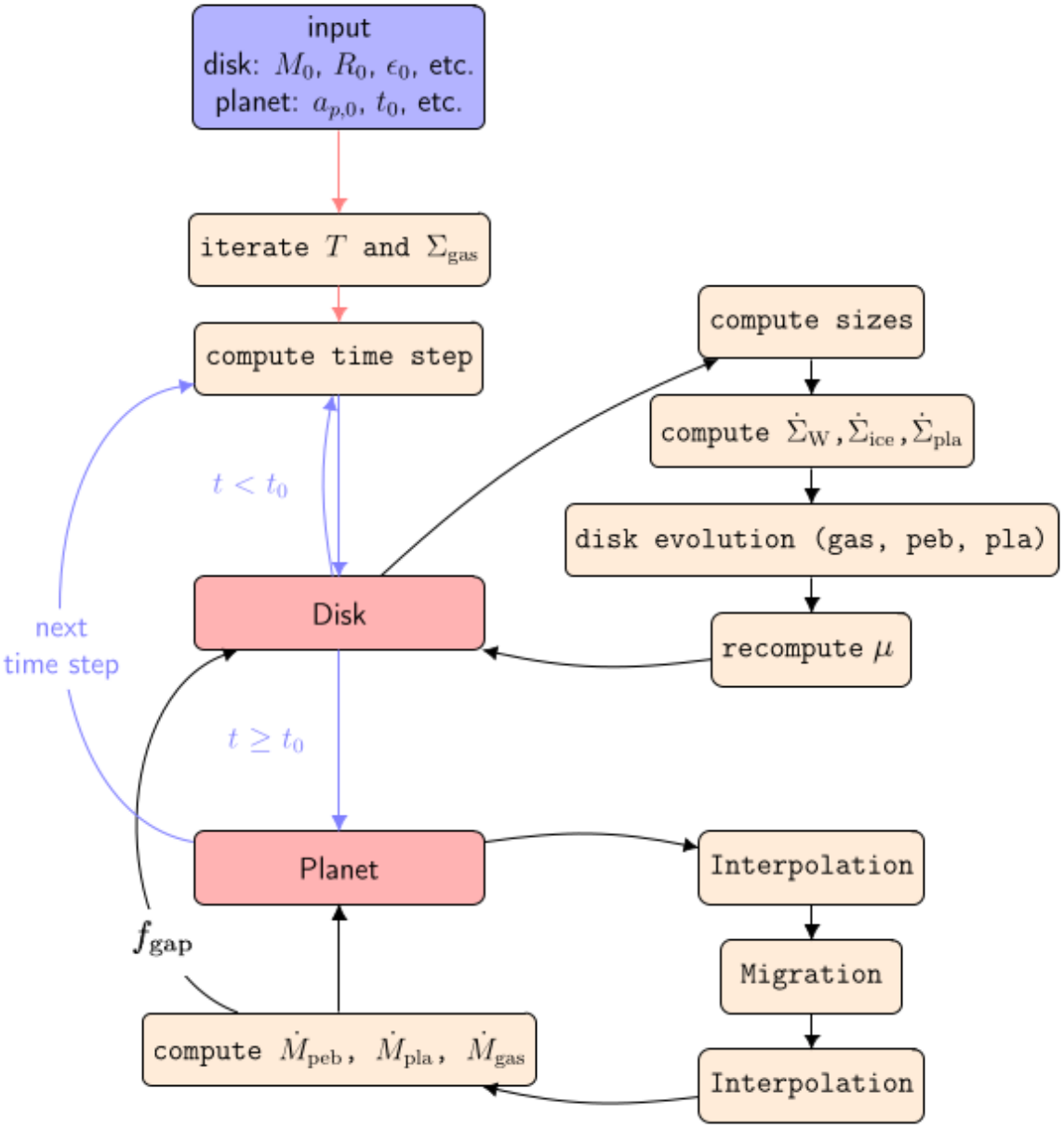

Figure 2.3: Operating principle of CHEMCOMP from Schneider, Bitsch (2021).

To initialise the code we use the analytical solution presented in Lodato et al. (2017) for the gas surface density. Using the input parameters (like dust-to-gas ratio), the code then computes the gas and dust surface densities and through them, the temperature profile of the disk, as shown by the first red arrow in Figure 2.3. Since the initial surface density is viscosity dependent, which itself depends on temperature, the initialization step is iterated until the temperature has reached 0.1% accuracy, to ensure convergence. The red arrows of Figure 2.3 are steps that are done just once in each simulation.

The main temporal loop of the code is marked by the violet arrows and begins with the disk module computing the pebble growth according to (Birnstiel, T. et al., 2012), as well as evaporation and condensation at evaporation fronts and the sink and source terms ($\dot{\Sigma}_{\mathrm{W}}$, $\dot{\Sigma}_{\mathrm{ice}}$) for the viscous evolution of the disk, as shown in the subroutine of the disk module in Figure 2.3. The viscous evolution of the disk is computed using a donor-cell scheme outlined in Birnstiel et al. (2010), which solves equations (15-11) for every molecular species.

At this point, the disk has evolved in time and we can use the updated quantities to compute the torque acting on the planet (that will make the planet migrate). To do so, we perform interpolation to get these values at the planet's current location, we advance its position by means of equation (1.124) and we interpolate the disk quantities again to the updated planet position, as sketched in the planet subroutine in Figure 2.3.

The next step is then to model the growth of the planet via pebble accretion (Johansen, Lambrechts, 2017) (equation (1.112)) and gas (Ndugu et al., 2020b) (equation (1.121)) inside the disks, while tracing the chemical composition of the accreted material to derive the atmospheric C/O ratio and the heavy element content. These accretion terms are added to the composition of the planet and additionally converted into sink terms for the viscous evolution of the disk in the next time step. The accreted gas, pebbles, and planetesimals are removed from the respective surface densities and in the pebble case, these are removed from the cell in which the planet is located since the Hill sphere is not resolved numerically during pebble accretion.

The stop conditions for the simulation are either the planet reaching the inner edge of the disk or the disk has completely dissipated (its mass is below $10^{-6} M_{\odot}$). If both checks are negative, a new time evolution takes place.

Chapter 3

Results

The main aim of this work is to study how the different formation pathways impact the atmospheric composition of the planet. To do so, we focus our attention on the growth tracks of the planets, their atmospheric C/O ratio, volatile to refractory ratio, and heavy element content. The following Sections will cover the comparison between three different planet formation scenarios:

- Planetary formation via pebble accretion only
- Planetary formation via pebble accretion with the possibility of planetesimal formation in the disk
- Planetary formation via pebble and planetesimal accretion

We start by specifying all the possible parameters used in the simulation for the disk and the planet:

Planet parameters		
Quantity	Value	Meaning
a_p	3, 10, 30 AU	initial position of planetary seed
t_0	0.05 Myrs	time at which the seed is planted
$\kappa_{\rm env}$	0.05 $\rm cm^2 g^{-1}$	envelope opacity

Disk parameters		
Quantity	Value	Meaning
α	$(1, 5, 10) \cdot 10^{-4}$	alpha viscous parameter
α_z	$1 \cdot 10^{-4}$	vertical mixing
M_0	$0.128 M_\odot$	initial disk mass
R_0	137 AU	intial disk radius
t_{evap}	3 Myrs	disk lifetime
ε_0	1.5%	dust to gas ratio
u_{frag}	5 m/s	fragmentation velocity
$\%C$	60%	carbon grain percentage
R_{pla}	$1, 50$ km	radius of accreted planetesimals

The following Sections also have a table that specifies which kind of parameters were used for which analysis.

3.1 Pebble accretion and planetesimal formation scenario

We started by considering the first two planet formation scenarios, namely the case in which the planet formation is due to pebble accretion and the case in which planetesimal formation (described in Section 1.2.1) is also allowed inside the disk.

All the results presented in this section are simulated using the parameters presented in tables 3 for three planets whose seeds were planted at 3, 10 and 30 AU. We also consider the three possible disk viscosities of table 3.

3.1.1 Disk quantities

We first analyse what happens to the gas and dust in the disk in the two considered scenarios if we do not form a planet inside our disk.

Disk surface densities

Figure 3.1 shows the gas, pebble[1] and planetesimal surface densities of a disk with $\alpha = 10^{-3}$ as a function of radius and time, in the pebble accretion only scenario (left panel) and in presence of planetesimal formation (right panel). The vertical dotted lines represent the evaporation fronts of some molecules that we consider in our model.

[1]We recall that the pebble surface density is obtained from the dust surface density multiplying it by a factor f_m as given by equation (2.2).

In both cases we observe the gas surface density (blue line) to decrease with time in the inner part of the disk, due to the gas falling into the protostar, and slightly increasing outward, due to the diffusion.

The pebble surface density (green line) in both cases shows spikes at the evaporation lines, due to the fact that immediately beyond the evaporation line, the gas condenses into dust increasing the local pebble surface density. Furthermore, the pebble surface density first increases with time, then it decreases as pebbles are used either to form planets or drift into the central star. this increase is smaller in the case of planetesimal formation because the material is subtracted by the pebble surface density to form planetesimals. The pebble surface density shows generally, as time passes, a steeper profile with respect to the gas profiles due to the inward drift of pebbles (increased Σ in the inner part, decreased in the outer part of the disk).

The right panel of Figure 3.1 shows the scenario in which we allow planetesimal formation. The planetesimal surface density (red line) also presents spikes at the evaporation lines, due to the re-condensation of gas forming a higher density of pebbles, which leads to the formation of planetesimals. As observed in Lenz et al. (2019), the planetesimal surface density profile is steeper than the initial dust[2] and gas surface density. This happens in the case of not too high turbulence (in Figure 3.1 we have $\alpha = 10^{-3}$, moderate turbulence) when the planetesimal formation is mostly hindered by the radial drift barrier, because the particles that are not converted into planetesimals in the outer part of the disk drift inward and can still participate in the planetesimal formation in the inner part of the disk, increasing the planetesimal surface density.

Different disk viscosities We now show, in a more general case, the form of the surface densities for different disk viscosities.

Figure 3.2 shows a comparison between the pebble only scenario (top row) and the planetesimal formation scenario (bottom row) for the three different viscosities that we considered in our simulations ($\alpha = 10^{-4}, 5 \cdot 10^{-4}, 10^{-3}$).

The top row of Figure 3.2 shows the pebble accretion scenario. We notice that the pebbles tend to drift inward with time (the surface density increases in the inner part and decreases outside) regardless of the viscosity. In particular, after 0.5 Myrs the higher viscosities (right panels) have pebble surface densities that are even one order of magnitude above the initial value in the inner part of the disk, showing a more efficient inward drift. In all cases the surface density decreases as the disk evolves because pebbles fall into the central star or accrete on planets.

Lower viscosities give rise to bigger pebbles, which implies a more efficient pebble accretion into planets. Indeed, in the lowest viscosity case (top left plot of Figure 3.2) we can see that we end up with a lower pebble surface density, meaning more pebbles have been used either to form planets or have drifted more efficiently towards the central star.

[2]In this case we compare it to pebble surface density.

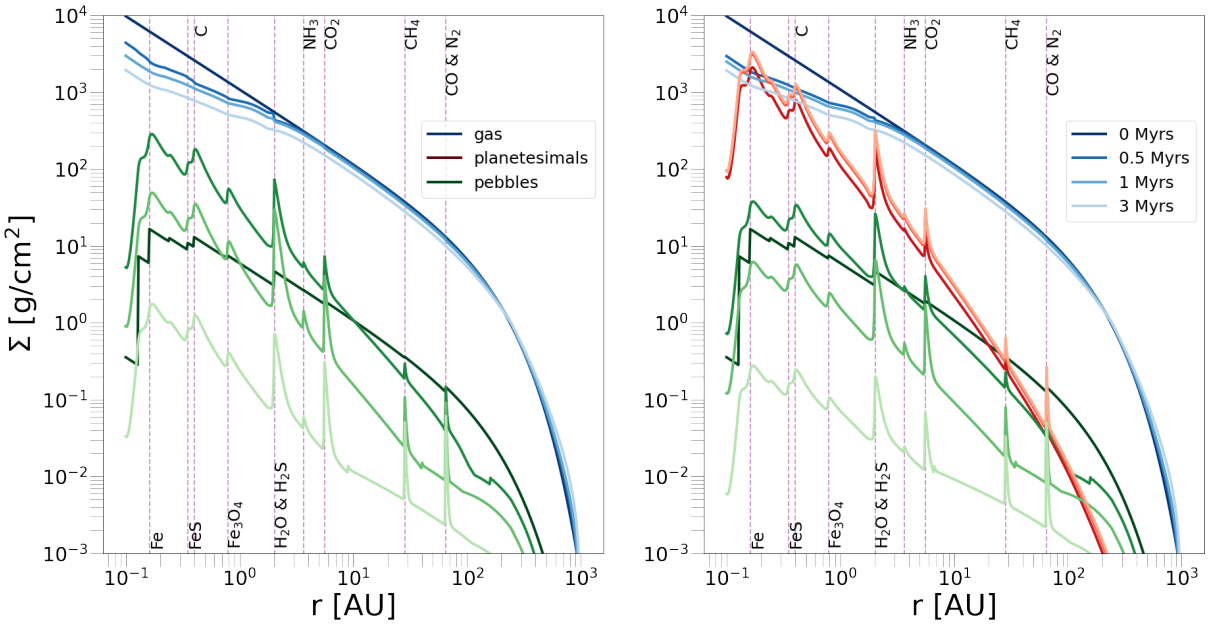

Figure 3.1: Surface densities of gas, pebbles and planetesimals for the disk described in table 3 in absence of planets, in the case of $\alpha = 10^{-3}$. The left panel shows the pebble accretion scenario, where planetesimals cannot form, right panel shows what happens, instead, to the surface densities when planetesimal formation is involved. We observe the same trend of time evolution of gas and pebble surface densities. The pebble surface density in particular, despite being reduced in the right panel, because some material is subtracted by it to form planetesimals, still shows the typical spikes at the evaporation fronts. This is due to the fact that, when crossing the evaporation line, gas rapidly re-condenses into pebbles, increasing the local surface density. It also decreases with time in both cases as the pebbles either drift and accrete onto the protostar or accrete on the planet. We observe that the planetesimal surface density also presents spikes at the evaporation fronts for the same reason, furthermore, it is steeper than the initial dust and gas surface density: this happens when the disk is drift limited and particles that were not able to form planetesimals in the outer part of the disk are still able to drift inward and form planetesimals inside.

The same comments on the pebble surface density comparison between different viscosities also apply to the case in which planetesimal formation is present (bottom row of Figure 3.1). The profile of the planetesimal surface density is slightly steeper in the case of low viscosity and leads to higher densities in the inner part of the disk. This happens, as also pointed out in Lenz et al. (2019), when the turbulence is low and the disk is drift limited: the pebbles drift inward faster and the ones that were not involved in planetesimal formation in the outer part of the disk form planetesimals in the inner part, increasing $\Sigma_{\rm pla}$.

Disk water content

We investigate the water content of the disk in the absence and presence of planetesimal formation to better understand how much the drifting and evaporation of pebbles affects the disk gas composition.

Figure 3.3 shows the water content of the gas in the disk (color coded) as a function of the distance from the central star and as a function of time, for $\alpha = 10^{-3}$ viscosity. The left panel shows the pebble accretion case, while the right panel describes the planetesimal formation scenario. The vertical violet line marks the water evaporation front in the disk.

We notice that in both cases at the early stages the water fraction in the gas is low because pebbles still did not have the time to drift inward and enrich the inner part of the disk in water vapour. As the disk evolves and the pebble drift, the water content increases. The main difference that we can notice between the two scenarios is that, in the planetesimal formation case, the water enrichment is clearly limited by the fact that a large number of pebbles are locked into planetesimals, and thus cannot evaporate enriching the gas in water vapour.

Different disk viscosities Figure 3.4 shows the water content of the disk for the two scenarios (top row: pebble accretion, bottom row: planetesimal formation) for the three different viscosities. The main difference that we notice between the high and the low viscosities is that the lower the viscosity (left panels), the more the gas in enriched in water, because low viscosities have more inefficient gas diffusion.

The lowest viscosities for both scenarios (left top and bottom panels of Figure 3.4), also take more time initially to enrich the innermost part of the disk. We also observe that the higher the viscosity, the faster the disk loses water vapor as it evolves with time. This is due to more efficient gas diffusion that accretes onto the central star.

Pebble and planetesimal total mass

Figure 3.5 shows the total mass of pebbles (light blue line) and pebbles and planetesimals (blue line) as a function of time in the pebble only accretion scenario (dotted line) and in presence of planetesimal formation (solid line).

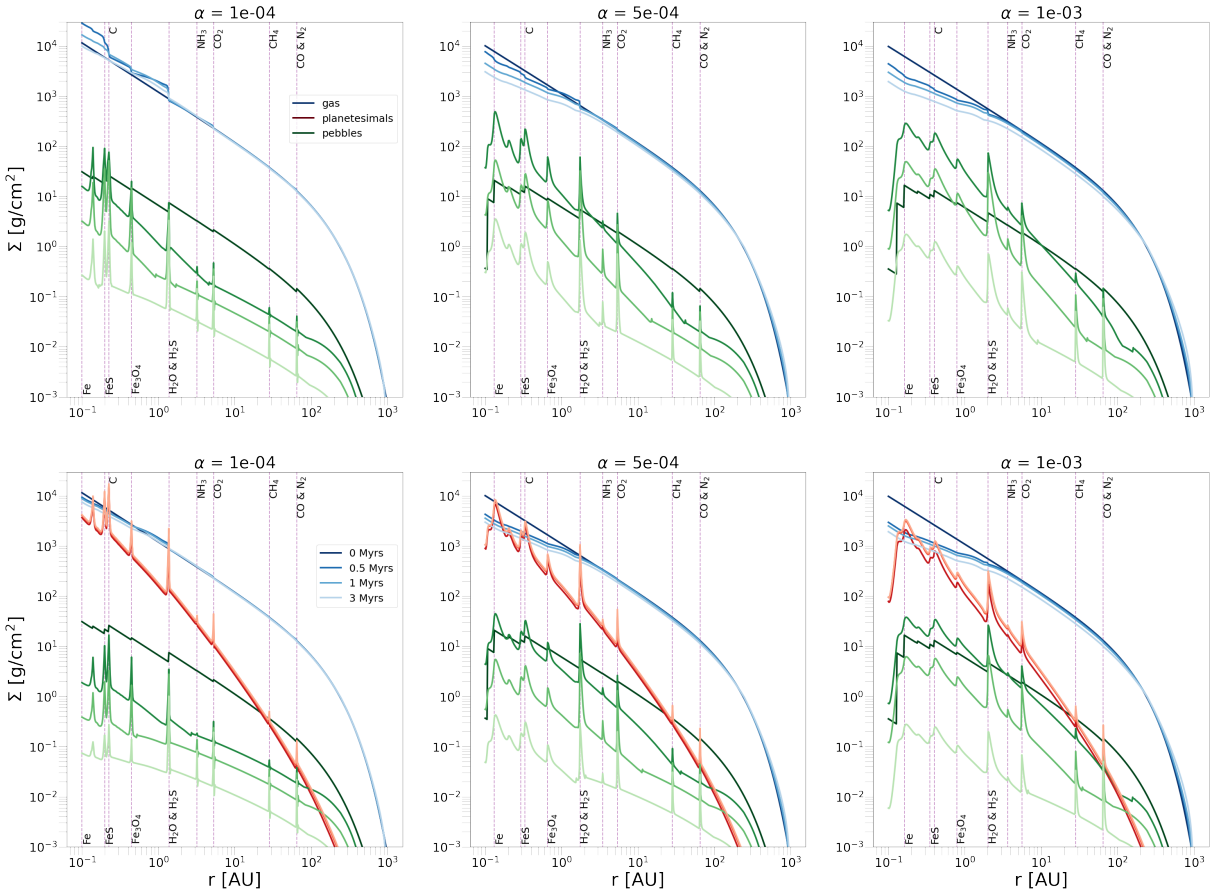

Figure 3.2: Gas (blue lines), pebble (green lines) and planetesimal (red lines) surface densities as a function of the distance from the central star for 4 time snapshots for the three different disk viscosities. The top row represents the disk in the case of pebble accretion only, while the bottom row includes the planetesimal formation. We can notice that lower viscosities (left panels) result generally in lower pebble surface densities, because they give rise to bigger pebbles drift inward more efficiently or accrete more efficiently into planets. Lower disk viscosities give rise to steeper planetesimal surface density because the bigger pebbles drift faster inward, thus are involved in planetesimal formation in the inner part of the disk rather than in the outer one.

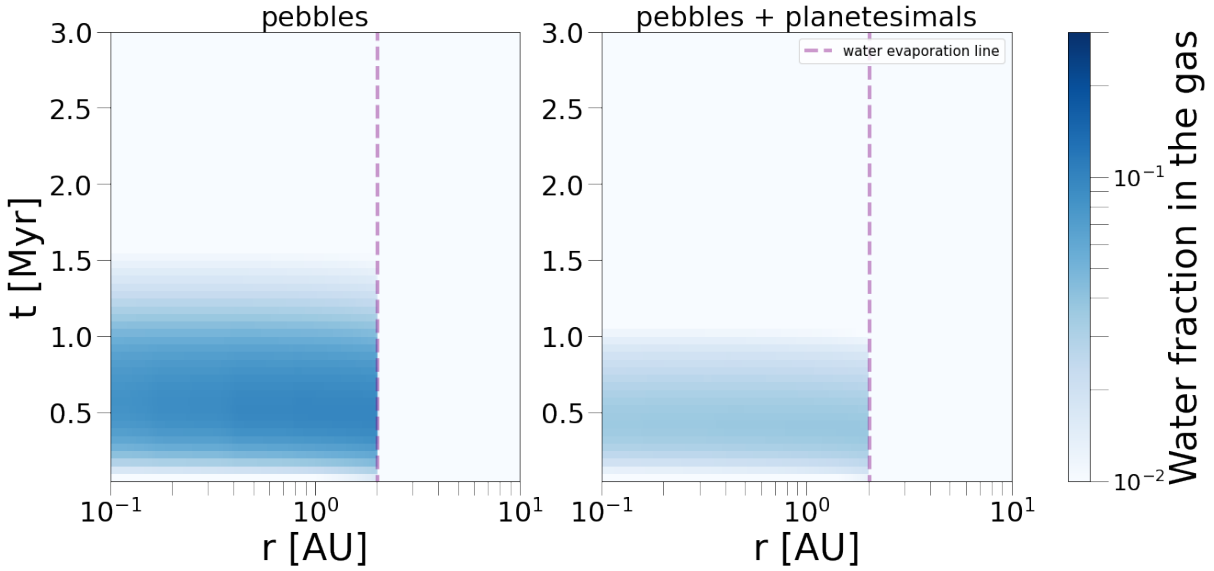

Figure 3.3: Water content in the gaseous phase of the disk as a function of radius and time for a disk viscosity $\alpha = 10^{-3}$ in the case of pebble accretion only (left panel) and in presence of planetesimal formation (right panel). We notice that at early evolutionary stages the water content in the inner part of the disk is small because pebbles have not yet drifted inward and enriched the gas in water vapour. As time passes, the inner disk is enriched in water: the main difference is that in the case of planetesimal formation, more material is locked into planetesimal and thus cannot drift and evaporate in the inner part of the disk, leaving it more depleted in water content.

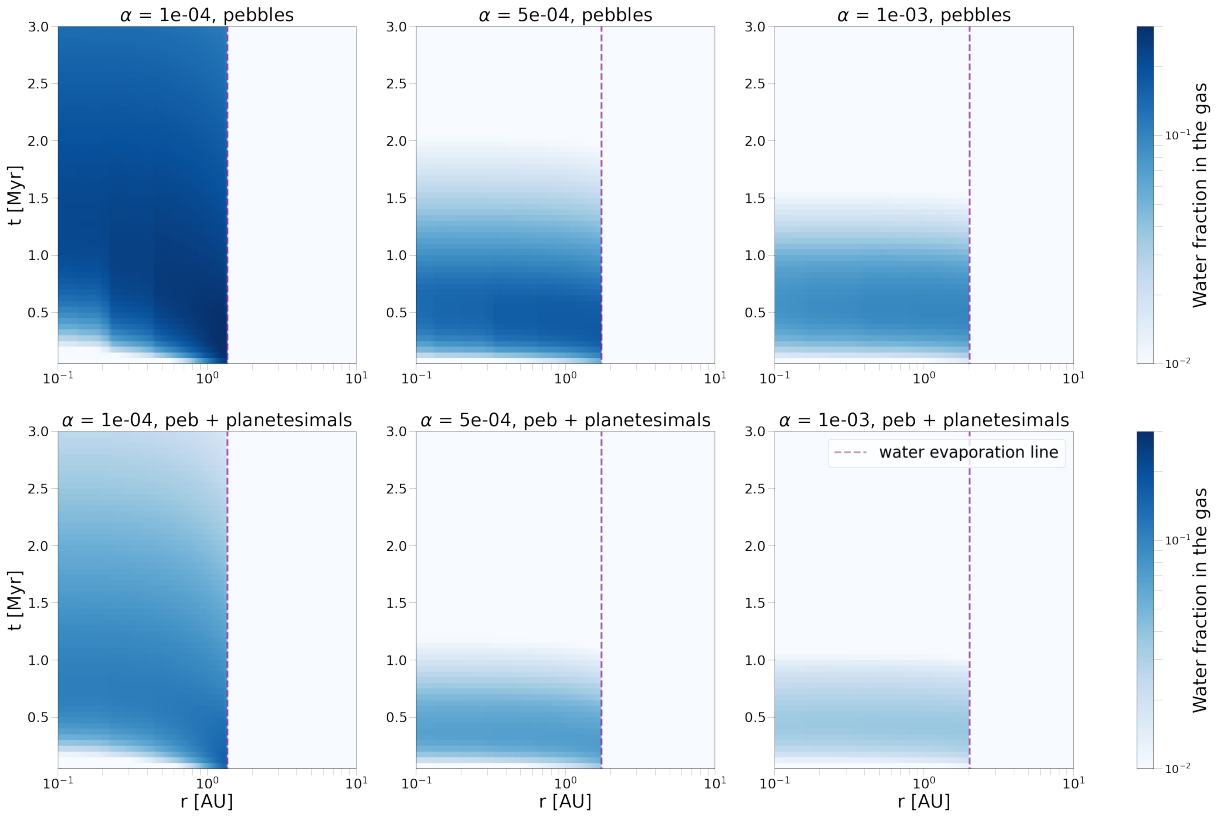

Figure 3.4: Water fraction in the gaseous component of the disk as a function of time and radius for the two different scenarios (pebble accretion in the top row, pebble accretion, and planetesimal formation in the bottom row) for the three different disk viscosities. We clearly see that low viscosities (left panels) lead, in both, cases to water richer disks, because the pebble inward drift is more efficient, thus more pebbles evaporate and enrich the disk. In this case, the disk remains water rich until it dissipates because low viscosity results in an inefficient gas diffusion. ///check the plots

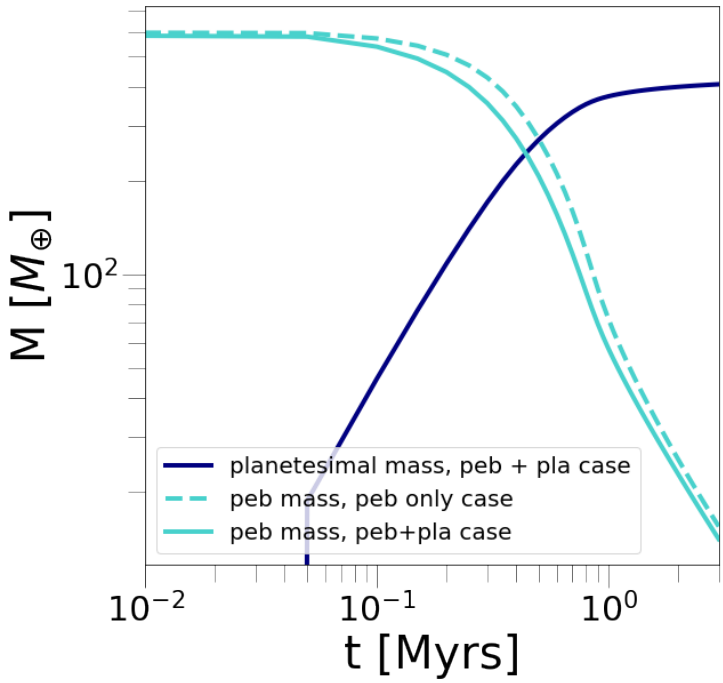

Figure 3.5: Total mass of pebbles (light blue lines) and planetesimals (navy line) in the two scenarios: pebble accretion only (dotted line) and planetesimal formation (solid lines). The total pebble mass decreases as a function of time with the same trend in both scenarios but is depleted in the planetesimal formation scenario because some of the pebbles are used to form planetesimals. The total planetesimal mass increases with time starting from 100 kyrs. This delay is due to the fact that pebbles need to grow in the disk before they are able to create a sufficiently high pebble flux to collapse into a planetesimal.

We observe that the total mass of the pebbles decreases with time in both cases with the same trend, but in the planetesimal formation scenario, it is slightly reduced because the "missing" mass is stored in the planetesimals.

The planetesimal total mass (blue solid line), indeed, increases with time, starting at around 100 kyrs. This delay is the result of the planetesimal formation method that we use, which requires a sufficient high pebble flux to form planetesimals, that actually need time to grow and end up in particle traps.

3.1.2 Growth tracks and atmospheric composition

Observations of exoplanets are able to constrain the composition of the atmosphere of the planet, thus it is important to investigate if different formation pathways can lead to different atmospheric compositions. To do so, we study in particular the C/O ratio of the atmosphere and the abundances of the different chemical species compared to solar abundances.

C/O ratio

Figure 3.6 shows the growth track of the three planets, planted initially at $3, 10, 30$ AU in a disk with $\alpha = 10^{-3}$, with the C/O ratio of the envelope color coded. The vertical lines represent the evaporation fronts of the different chemical species.

The left panel shows the case in which the planets formed via pebble accretion only, while the right panel shows the final result, including planetesimal formation. We can see in both cases that as the planets cross the water evaporation line, the C/O ratio decreases because the envelope is enriched in water vapor. Instead, as soon as the planets cross the C evaporation front the C/O ratio increases again. These increases/decreases in the C/O ratio happen with a bit of delay because the pebbles still drift a little bit after crossing the evaporation front and the gas needs time to accrete on the planet.

In the planetesimal formation case, we can observe the 30 AU planet migrating more with respect to the pebble only case. This is due to the fact that by removing pebbles from the pebble surface density (because they are used to form planetesimals), pebble accretion becomes more inefficient, thus the planetary growth is slower. This means that the planet reaches the pebble isolation mass later and therefore is subjected to type I migration, which is more efficient than type II, for a longer time, leading to a greater migration overall.

Figure 3.6 shows that the final C/O ratio (black numbers) in the two scenarios is different. The final value of the C/O ratio depends on when during the formation process the planet crosses the various evaporation fronts as well as on the mass of the planet: big planets have a smaller amount of accreted material compared to the total mass, thus a smaller change in C/O ratio.

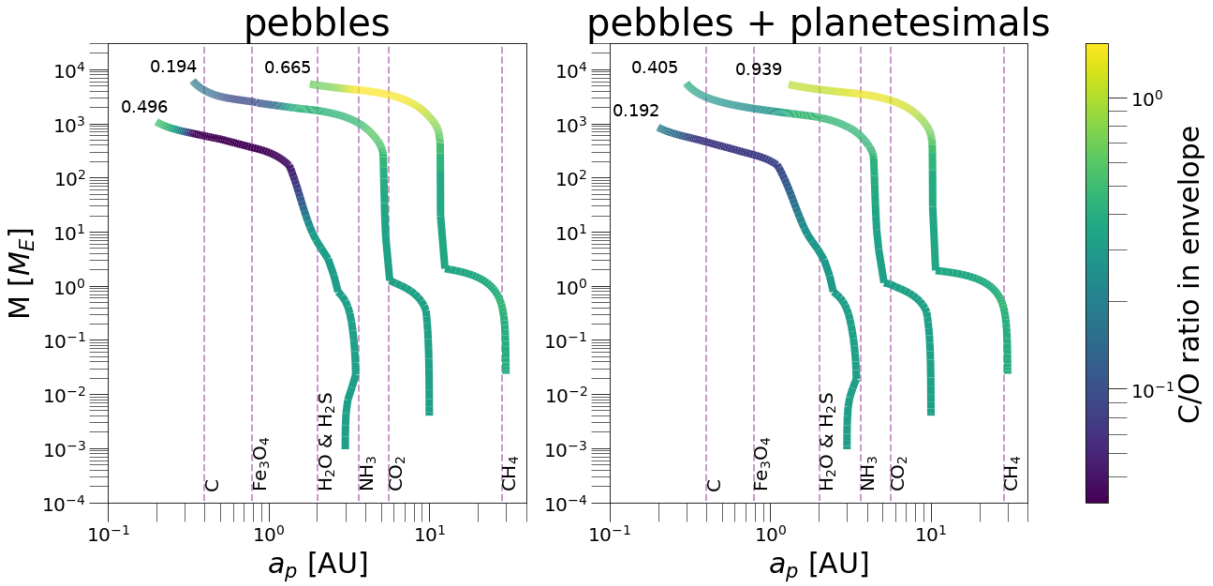

Figure 3.6: C/O ratio in the envelope of three planets planted initially at 3, 10 and 30 AU in a disk with $\alpha = 10^{-3}$, with planetesimal formation efficiency $\varepsilon = 0.01$. We observe the C/O ratio decreases as the planets pass through the water evaporation front and it increases again passing through the C evaporation front. The increase/decrease is not immediate because the pebbles still drift slightly after crossing the line before evaporating and the gas needs time to accrete on the planet. The 30 AU planet in the planetesimal formation case is able to migrate inward more because planetesimal formation hinders pebble accretion, making it less efficient and resulting in slower planetary growth. This, in turn, implies that the planet undergoes type I migration for a longer time, thus migrating inward more.

Furthermore, the changes in the C/O ratio of the planet as it crosses the different evaporation fronts are smaller in the planetesimal formation scenario, because the gas is less enriched in evaporated material compared to the pure pebble scenario.

For these reasons, the C/O ratio cannot provide sufficient information to tell the two formation scenarios apart.

Atmospheric composition

We also analysed the atmospheric composition of the planets in order to investigate whether the atmospheric composition, with a particular focus on the volatile to refractory ratio, can show significant differences between the two formation scenarios.

Figure 3.7 shows the comparison between the amount of C,O,N and C/O ratio in the atmosphere of a planet initially planted at 3 AU, with 60% carbon grains in the pebble accretion only scenario (left panel) and in the planetesimal formation scenario

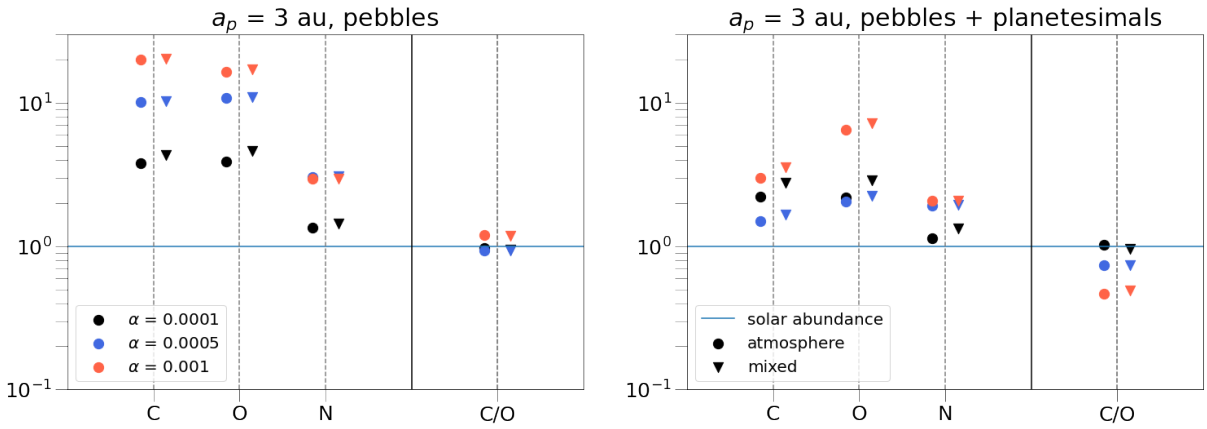

Figure 3.7: C,O,N and C/O ratio for the 3 AU planet in the two different scenarios. The different colors represent the three disk viscosities, while the different markers represent the atmospheric abundance (dots) and the mixed atmospheric and core abundance (triangles). Planets formed in the pebble accretion only scenario clearly show enhanced C/H and O/H ratios. We clearly observe a drop in the elemental abundance in the planetesimal formation case (right panel) due to the fact that some material is locked into planetesimals and thus cannot be accreted onto the planet.

(right panel). The different colors refer to different disk viscosities, while the different markers identify either the atmosphere composition (dots) or the total atmosphere and core composition (triangles).

The first thing that we notice is that considering the mixing of atmosphere and core (triangles), we have a general increase in the total amount of elements. The biggest change between the total and the atmosphere elemental abundances is in the low viscosity case (black), because these planets possess the same core mass as the planets that form in high viscosity disks but smaller envelope, thus the core elemental composition is diluted in a smaller atmosphere, causing a bigger change.

In the pebble accretion only scenario, the planets have clearly supersolar C/H and O/H ratios, because the drifting pebbles efficiently enrich the gas in volatile content that is subsequently accreted by the planet. The bigger the viscosity, the more enhanced are the C/H and O/H abundances because planets generally grow bigger and migrate more across the innermost evaporation fronts. If we introduce planetesimal formation in the disk, we see a general depletion in the elemental abundances because some of the elements available are locked into planetesimals. The depletion is more significant for higher viscosities because in higher viscosity disks planets migrate faster and are thus able to cross more evaporation fronts and enrich more in the different elements, resulting, therefore in a bigger depletion when the disk is less enriched because of planetesimal formation. In Figure 3.8 we compare the atmospheric composition for all the three planets simulated in

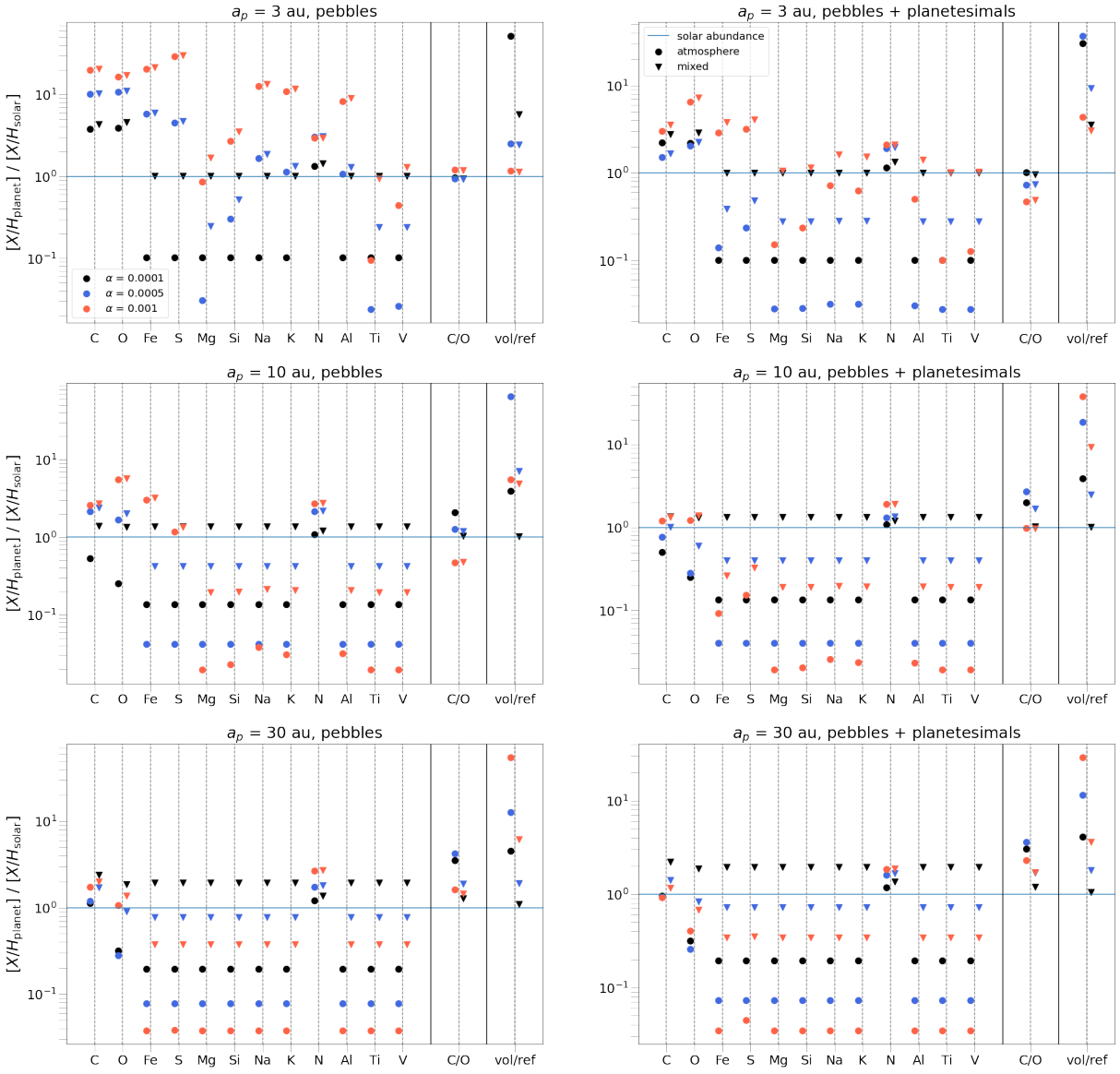

Figure 3.8: Comparison of the elemental abundance of the three planets in the two different scenarios. The different colors represent the different disk viscosities, while the different markers represent the atmospheric composition (dots) and the joint atmospheric plus core composition (triangles). Considering the mixing between core and atmosphere we observe an increase in all the elemental abundances that is more significant in the low viscosity case because in high viscosity disks planets migrate faster, thus accreting more gas, resulting in a more different mixed vs atmospheric composition. The pebble accretion only scenario clearly shows planets with supersolar C/H and O/H ratios. In the planetesimal formation case (right panel) we observe a general depletion of all the elemental species, in particular the refractories. This results in a slight increase in the volatile to refractory ratio, especially for higher viscosities.

the two scenarios, considering all the elements that we can trace in the disk. We see that for all three planets we can observe the depletion in the elemental abundances, mainly visible in the refractories[3]. This is due to the fact that refractories are mostly locked into planetesimals, that in this scenario do not accrete on the planet, while volatiles are accreted in gaseous form from the planet also in the planetesimal formation scenario.

We observe a slight increase in the volatile to refractory ratio in the case of planetesimal formation because the refractories that are locked into planetesimals are not accreted by the planet, therefore resulting in a depletion in the refractory content of the planet thus an increase in the volatile to refractory ratio.

3.1.3 Heavy element content

In Figure 3.9 we can see the heavy element content of the planets as a function of the total mass in the two different scenarios. The left panel shows the three planets in the pebble accretion only scenario, while the right panel includes planetesimal formation. The green line represents the fit from Thorngren et al. (2016), while the different disk viscosities are color coded.

We notice that higher viscosities in the disk lead to higher heavy element content in the planets because in high viscosity discs, the planets can migrate quickly by type II migration and accrete more refractory species that are closer to the central star. There is a clear difference between the pebble accretion only case and the planetesimal formation scenario, for which the heavy element content of the planets drops significantly. This is the result of locking refractory material into planetesimals that is therefore no longer available to be accreted on the planet, giving a smaller amount of heavy elements.

3.2 Pebble and planetesimal accretion scenario

In this Section we aim to compare the results from the previous section 3.1 with the planets formed in the planetesimal accretion scenario, to investigate whether we can find tracers to constrain the formation pathway of the planet.

3.2.1 Growth tracks

Figure 3.10 shows the growth tracks of the planets for the three different scenarios (top row pebble accretion only, middle row pebble accretion and planetesimal formation, bottom row pebble and planetesimal accretion) with the C/O content in the envelope color coded. Again, as already commented for the first two scenarios, the C/O ratio in the plant's envelope changes as the planet crosses the evaporation fronts.

[3]The refractories are all the elements except C,O and N.

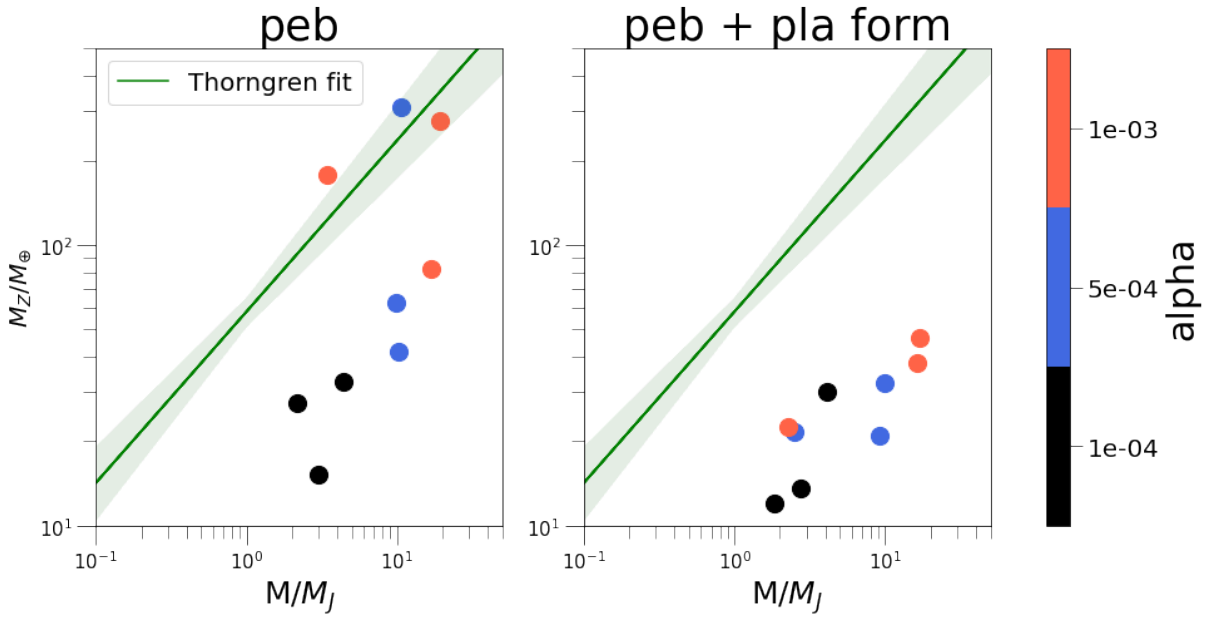

Figure 3.9: Heavy element content of the $3, 10, 30$ AU planets as a function of the total mass for the three different disk viscosities (color coded) in the two formation scenarios. The green line represents the Thorngren et al. (2016) fit. We clearly see that, in the planetesimal formation case, the heavy element content in all the planets drops significantly, due to the large amount of heavy elements locked into planetesimals that cannot accrete on the planet. Higher viscosities leads generally to more massive and more heavy element rich planets because in these disks planets can migrate quickly through the inner evaporation fronts and accrete more refractory species that are closer to the central star.

We observe that the changes in the C/O ratio become less important as we go from the pebble accretion only scenario to the planetesimal accretion scenario. In the planetesimal formation scenario, the changes are smaller because the gas is less enriched in evaporated material.

In the planetesimal accretion scenario, we see the drop in the C/O ratio when the planet crosses the water evaporation front is even smaller compared to the other two scenarios. The reason for this is that, as the planet crosses the water evaporation front it accretes water enriched vapor, but it also accretes planetesimals from that location, that are carbon rich, therefore the overall change in the C/O ratio is smaller compared to the planetesimal formation only scenario. The final C/O content of the atmosphere is different for the three scenarios but depends on many parameters, thus it is not a good method to tell the formation pathway apart.

3.2.2 Atmospheric composition

We compare the chemical composition of the atmosphere in presence of planetesimal accretion to the first two scenarios in Figure 3.11.

It is important to stress that planetesimals can be accreted at any time during the planet formation, more precisely, they will be accreted onto the core in the early formation stages, when the planet is still subjected to pebble accretion and into the atmosphere at later stages, as soon as the planet reaches pebble isolation mass and switches to gas accretion.

The most remarkable observation is that, in the case of planetesimal accretion, we have an overall increase in the refractory content, mainly in the atmosphere (dots) because the planetesimal surface density (and therefore chance of accretion) is higher in the inner part of the disk and the planetesimals accreted after the planet has reached pebble isolation mass are accounted for in the atmospheric composition. We also observe a slight drop in the volatile content. The atmospheric increase in the elemental abundance is more marked for the planet closer to the star because they migrate closer to the star where the gas is more enriched in elements coming from pebble evaporation.

We observe an important drop in the volatile to refractory ratio, due to the accretion of refractory reach planetesimals onto the planet, that may help to constrain the formation pathway of the planet. This drop is more significant in the atmosphere of the planet because more planetesimal mass is accreted after the planet has reached pebble isolation mass, thus it is accreted onto the atmosphere. Furthermore, it is more marked for the planet closer to the protostar because their pebble isolation mass is reached faster.

3.2.3 Heavy element content

We checked the heavy element content of the simulated planets as a function of the total mass also in the planetesimal accretion case. Figure 3.12 shows the comparison between

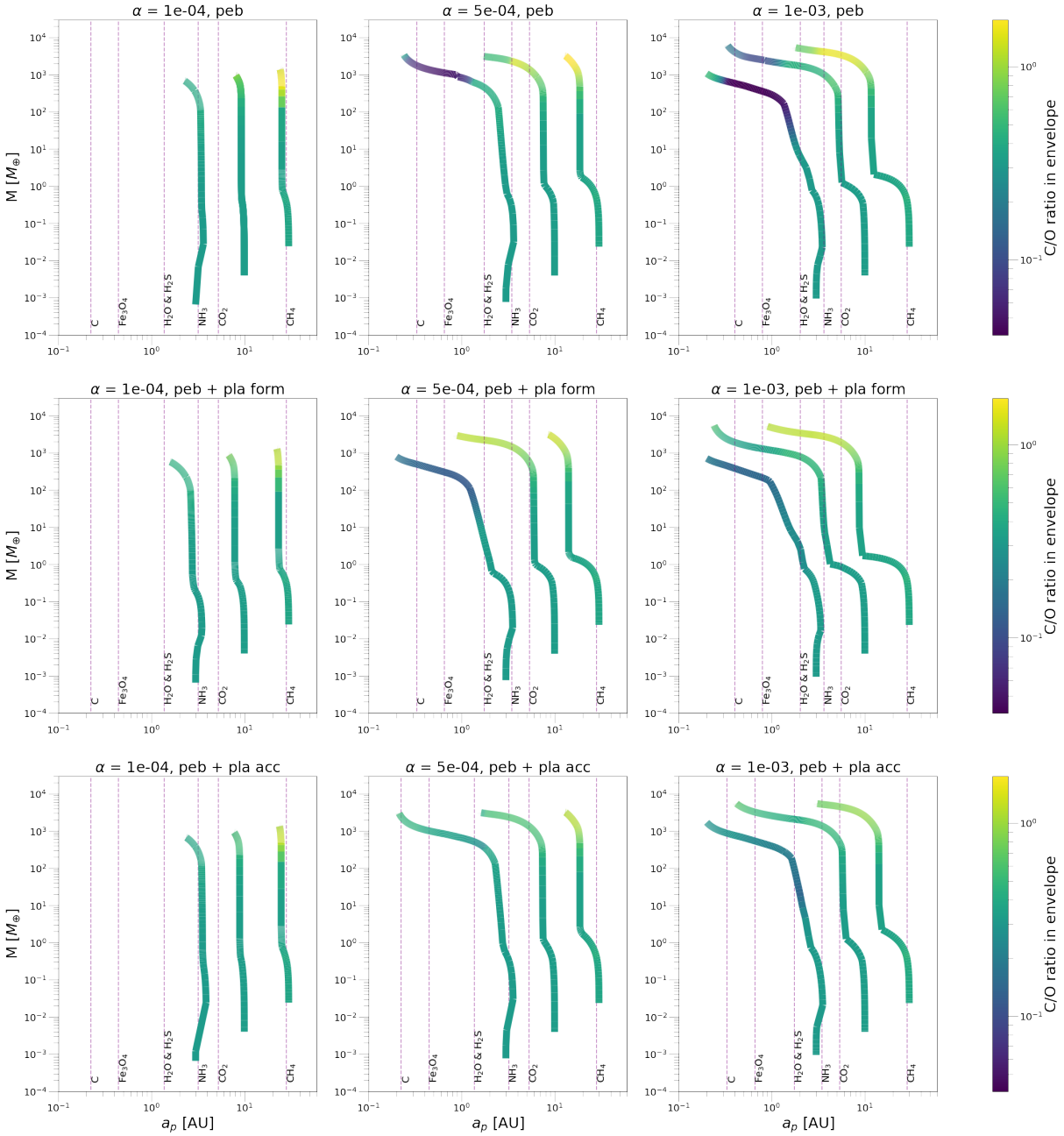

Figure 3.10: Growth tracks of the three planets in the different scenarios (top row pebble accretion only, middle row pebble accretion and planetesimal formation, bottom row pebble and planetesimal accretion). Color-coded the C/O ratio. We observe that the drop in the C/O ratio of the planets when crossing the water evaporation front is big in the pebble accretion only scenario because the gas of the disk is enriched in evaporated material. It slightly reduces in the planetesimal formation scenario because in that case the enrichment of the gas in the disk is smaller, due to the fewer number of pebbles drifting and evaporating. In the case of planetesimal accretion, the drop in the C/O ratio is very small because the planet also accretes planetesimals from that region at the same time, that are carbon rich, and therefore contribute to enhancing the C/O ratio.

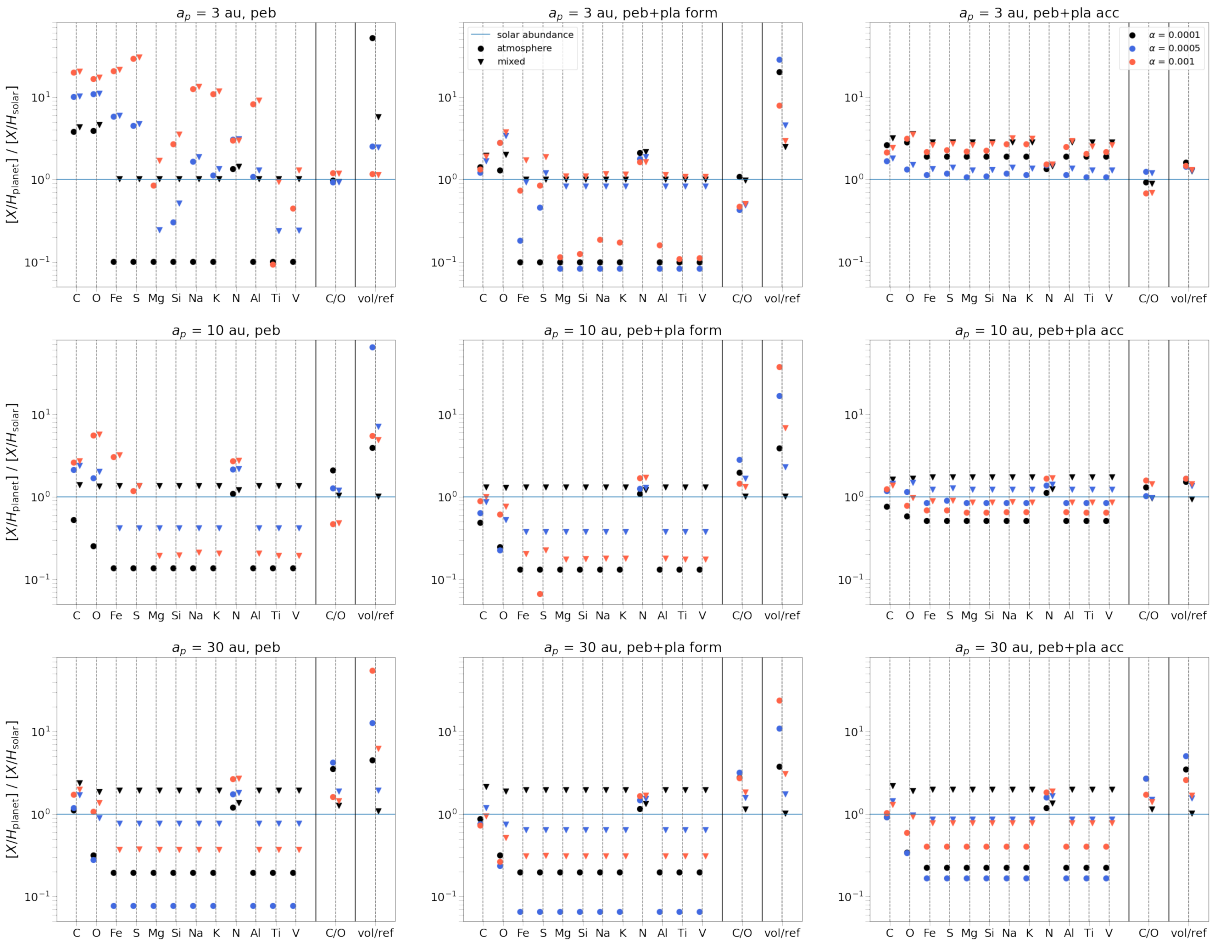

Figure 3.11: Elemental abundance in the atmosphere of the three planets, for the three viscosities and in the three scenarios. The different colors represent the different viscosities while the markers represent the atmospheric composition (dots) and the mixed composition (triangles). The refractory abundance is clearly enhanced in the planetesimal accretion case, mainly in the atmosphere of the planet because planetesimals are more likely to accrete in the inner region of the disk when the planet has already reached pebble isolation mass and thus they are accreted into the atmosphere. The volatile abundance is slightly decreased. We notice a remarkable drop in the volatile to refractory ratio due to the accretion of refractory reach planetesimals onto the planet in the planetesimal accretion case, which might help to constrain the formation pathway of the planet.

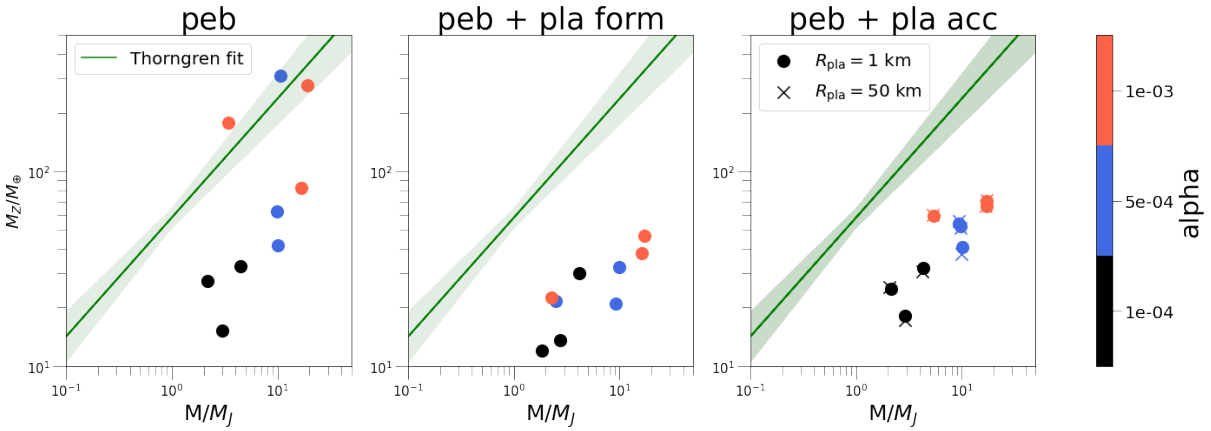

Figure 3.12: Heavy element content of the planet as a function of the total mass for the three scenarios. The color coding represents the different viscosities, while the crosses and the dots in the planetesimal accretion scenario represent different sizes of the accreted planetesimals. Compared to the planetesimal formation case (central panel), in the planetesimal accretion scenario (right panel) we can see an increase in the total heavy element mass due to the planetesimals being able to accrete on the planet. The size of the accreted planetesimals (dots and crosses) seems to have a very small impact on the final heavy element mass. Again higher viscosities lead to larger amounts of heavy elements in all scenarios.

the pebble accretion only scenario (left panel), planetesimal formation (central panel), and planetesimal accretion (right panel), with the color coding representing the different viscosities. The dots and the crosses in the right panel distinguish between the two different radii of accreted planetesimals, respectively 1 and 50 km. The green line again represents the fit from Thorngren et al. (2016).

As already commented in Section 3.1.3, if we form planetesimals in the disk we significantly deplete the heavy element mass of the planets, because we lock material into planetesimals. If we include the possibility to accrete those planetesimals onto the planet (right panel), then we observe a small increase in the heavy element content. The size of the accreted planetesimals (dots or crosses) seems not to have a significant impact on the final heavy element mass of the planets. The scenario that produces the planets with the highest heavy element mass content is clearly the pebble accretion scenario.

Heavy element content origin

The triangular plot in Figure 3.13 shows the origin of the heavy element content of the simulated planets. Each of the three axes represents the percentage of heavy element mass provided by a certain phase (gas, pebbles, or planetesimals). The different markers represent the three different scenarios: the dots for the pebble accretion only scenario, the

triangles for the planetesimal formation scenario, and the plus and crosses for the planetesimal accretion scenarios with 1 and 50 km radii of accreted planetesimals respectively. The color bar distinguishes between the three different disk viscosities.

We see that all the planets simulated in the first two scenarios lie on the bottom row because they do not accrete planetesimals. In particular, we clearly see that in the pebble accretion only scenario (dots) most of the heavy element mass of the planet is in gaseous form (for example, the two planets in the bottom left corner have more than 90% of heavy elements in the gas phase). This happens because, in the pebble accretion only scenario, pebbles are accreted up to the time at which the planet reaches pebble isolation mass, then the planet grows only by gas accretion. This limiting mass is bigger in the outer regions of the disk, thus we expect planets that form further away to have less mass percentage in gas and more in pebbles, as we confirm in these plots.

In the planetesimal formation case, instead, the pebble contribution to the heavy element content is more significant (between 25% and 75%).

On the contrary, the planets simulated in the planetesimal accretion scenario gain most of their heavy element mass from planetesimals, especially for high viscosities (red plus and crosses), where more than 50% of the heavy mass is due to planetesimals. This is due to the fact that the heavy elements are locked into planetesimals and therefore cannot enrich the gas and be accreted in gaseous form, but are then dumped into the planet when the planetesimal accretes on the planet. Again the size of the accreted planetesimal does not make a difference in the final mass of the planet, nor in the heavy element content origin. Figure 3.14 shows the same diagram as Figure 3.13 but with the total heavy element mass colour coded and the different markers representing the different initial positions of the planets: 3 AU (stars), 10 AU (diamonds), 30 AU pentagons.

For the pebble accretion only planets we observe that the 3 AU planets (stars) have most of their heavy element content in gaseous form (more than 80%) for all the considered viscosities. This happens because planets closer to the star reach pebble isolation mass and switch to gas accretion faster than the outside planets. We also observe that the higher the viscosity of the disk, the bigger the final total heavy element mass. This happens because planets in higher viscosity disks migrate more and thus cross more evaporation lines (especially the water ice line), as clearly shown in the growth tracks in Figure 3.10, accreting higher heavy element content.
The 10 AU planets (diamonds) also show a high fraction of the total heavy element mass in gaseous form (above 75%), with the exception of the planet formed in the low viscosity disk, which has a gas fraction of just 20%.
The 30 AU planets (pentagon) have a more variable fractional distribution of the heavy element mass, but confirm the trend of higher total heavy element mass for higher disk viscosities.
Another trend that we observe in this case is that the higher the gaseous fraction of heavy elements, the higher the final total heavy element mass.

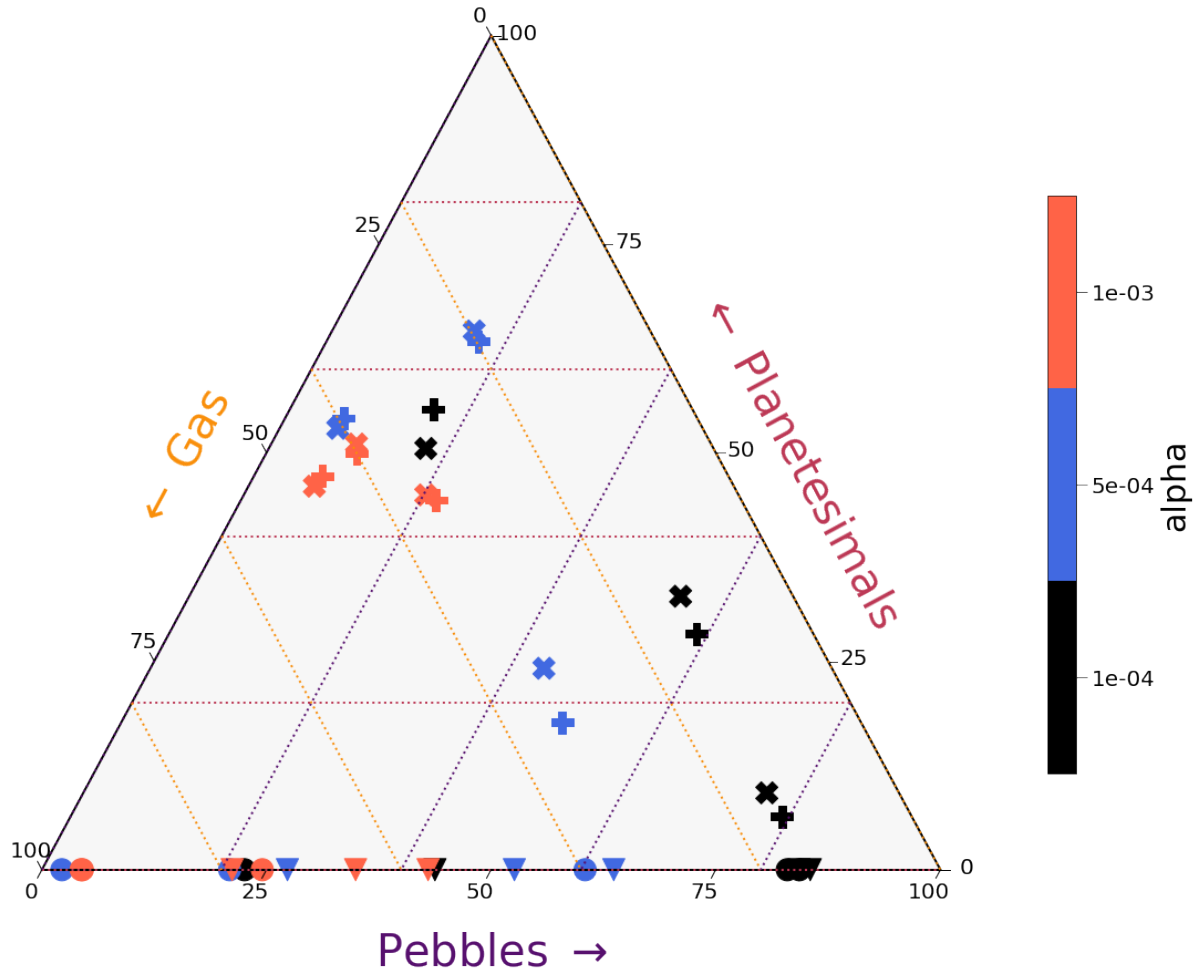

Figure 3.13: Heavy element mass origin of the planets. Each axis contains the percentage of heavy element mass given by a certain phase (gas, pebbles, or planetesimals). The different markers represent the different scenarios: pebble accretion only (dots), planetesimal formation (triangles) and planetesimal accretion (plus for the 50 km planetesimals and crosses for the 1 km planetesimals). The planets of the pebble accretion scenario have most of their heavy element mass in gaseous form, because, once the planet has reached pebble isolation mass, it grows only by gas accretion. The pebble isolation mass is reached faster for the planet closest to the star. The planets growing in the planetesimal formation have an important contribution also in pebbles. Finally, the planets of the planetesimal accretion scenario have most of their heavy elements in solid form, because the pebbles locked into planetesimals couldn't enrich the gas in heavy elements, but they could still be accreted on the planet in solid form. Higher viscosities lead to higher percentages of heavy elements locked into planetesimals.

In the planetesimal formation scenario both the 3 AU and 10 AU planets have a gaseous fraction between $75\% - 50\%$, while the 30 AU planets tend to have higher pebble fraction (above 50%), probably due to the fact that, starting further out, they need more time to migrate and get to accrete less heavy element enrich gas (that is already not as enriched as in the pebble accretion only scenario).
In this case, we observe that a higher gaseous fraction of heavy elements leads to lower total heavy element mass because the gas is depleted with respect to the pebble accretion only phase.

In the planetesimal accretion scenario, the 3 AU planets are all concentrated in the same part of the plot, regardless of the viscosity or the planetesimal radius. They all have a $40\% - 60\%$ fraction of planetesimal mass, $50\% - 30\%$ gas, $10\% - 20\%$ pebbles, and similar final total heavy element mass.
The 10 AU planets have a low planetesimal and gas mass fraction for the lowest viscosity (around 30% and 15% respectively) while for the higher viscosities they show in between $50\% - 65\%$ of the planetesimal mass fraction.
The 30 AU planets are the ones with the lowest planetesimal fraction (just 10% for the low viscosity case), furthermore, they show a trend: higher viscosities lead to a higher planetesimal fraction.
All the planets show the same trend regarding the final heavy element mass, the higher the viscosity, the higher the mass.

We notice, accordingly to Figure 3.12, that the planets formed in the pebble accretion scenario only have bigger heavy element masses than the planets formed in the other two scenarios.

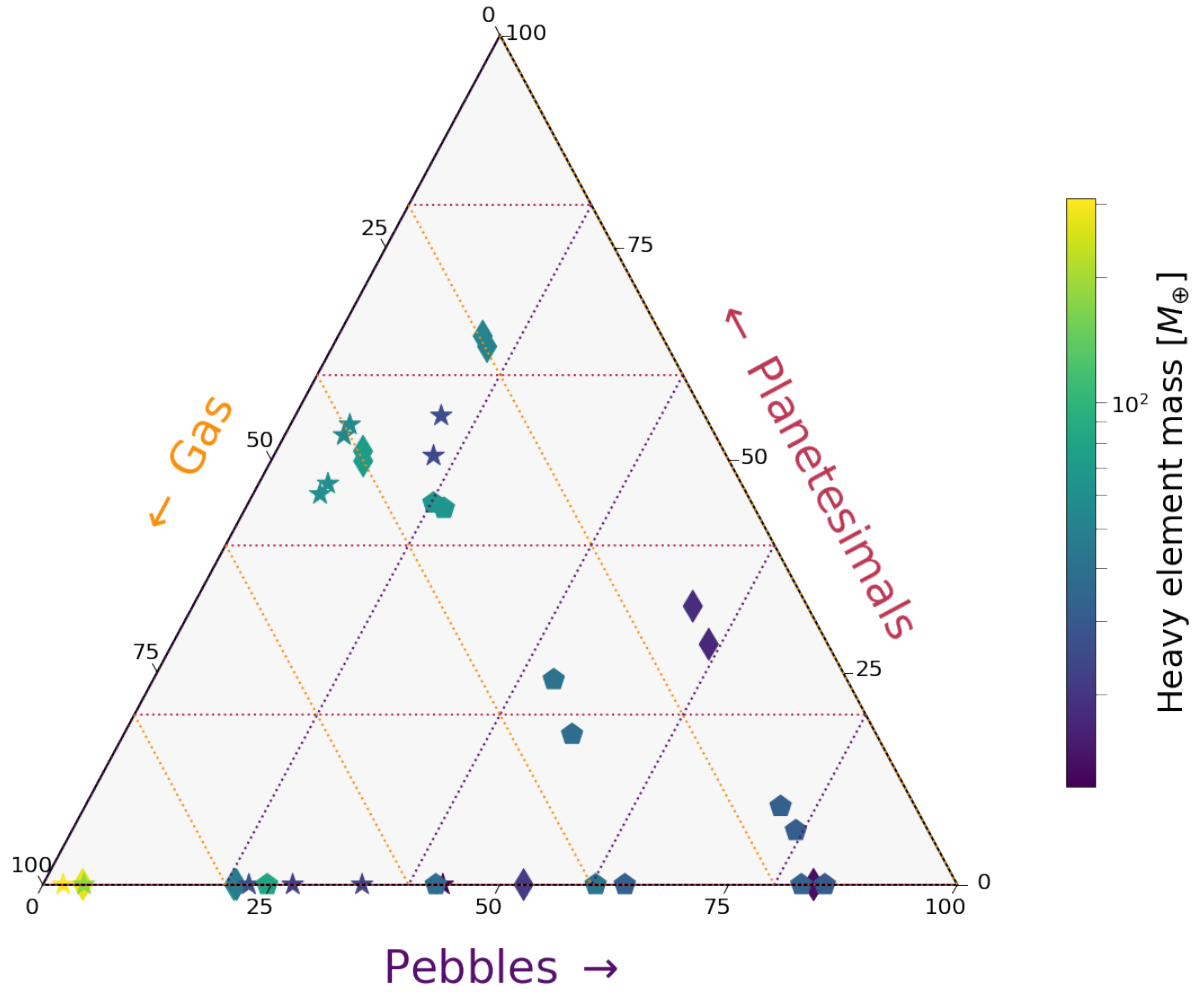

Figure 3.14: Heavy element mass origin for the simulated planets, as in figure 3.13, but with total heavy element mass color coded. The different markers represent the different initial positions of the planets: 3 AU (stars), 10 AU (diamonds), and 30 AU (pentagons). In the pebble accretion only scenario, the 3 and 10 AU planets have most of their heavy element mass fraction in gaseous form (up to 80%), while the 30% AU planets show a more variable fractional distribution. Overall, all planets have higher final total heavy element mass for higher viscosities. In the planetesimal formation scenario, 3 and 10 AU planets still have a significantly high gaseous mass fraction, while the 30 AU tends to have a higher pebble fraction. In this case, we notice that the higher the gaseous fraction is, the lower the final total heavy element mass. Finally, in the planetesimal accretion scenario, the 3 AU planets are all concentrated in the same part of the plot, regardless of the viscosity or the planetesimal radius. The 10 AU planets show a smaller planetesimal and gas mass fraction for low viscosities and a higher one for higher viscosities, while the 30 AU planets are the ones with the lowest planetesimal fraction. We also observe a trend both in the 10 and 30 AU planets: the final total heavy element mass increases with increasing viscosities.

Chapter 4

Discussion

Constraining the formation pathway of a planet is still an open question in the planetary formation field. Observed exoplanetary abundances could help tell the formation scenarios apart (Mordasini et al., 2016; Madhusudhan et al., 2017), especially the atmospheric C/O ratio that can be measured with high precision (Mollière et al., 2015) and strongly depends on the planet's formation environment.

These atmospheric measurements will be improved by means of the JWST observations and the ARIEL survey by the end of the decade. The models that aim to investigate the planet formation processes often include the growth of planetary cores via planetesimal accretion (Mordasini, C. et al., 2012; Emsenhuber et al., 2021) or pebble accretion (Bitsch, Bertram et al., 2015; Lambrechts, M., Johansen, A., 2012; Lambrechts, M. et al., 2014), but usually they do not include the chemical composition of the dust. Other studies instead focus on the chemistry of the disk (Semenov, D. et al., 2010; Eistrup, Christian et al., 2016; Notsu et al., 2020) without considering the physics of grain growth and drift.

In this work, the disk model includes both the growth and drift of the pebbles along with the evaporation and condensation of pebbles at the evaporation fronts. We then model the growth of a planet starting with a seed artificially planted in the disk, via both pebble and planetesimal accretion, while tracing the planet's chemical composition to derive the C/O ratio and the heavy element composition.

Figure 3.12 summarizes the main message that we aim to convey in this study. The pebble accretion only scenario is able to provide planets with low heavy element content as well as planets with high total heavy element masses, while the planetesimal formation and accretion scenarios both fail to grow planets with enhanced heavy element mass. Although we could potentially form planets with low heavy element masses in a high-efficiency planetesimal formation and accretion scenario, planets with high heavy element content are observation supported, meaning that planetesimal formation in those cases must be inefficient.

Now we provide a qualitative discussion of the parameters that were omitted or only partially investigated in this work before briefly setting these results in a wider context.

Fragmentation velocities Fragmentation velocity determines how fast a pebble can drift before a collision will lead to fragmentation rather than coagulation. Laboratory experiments (Blum, Wurm, 2008; Gundlach, Blum, 2015; Musiolik, Wurm, 2019) show typical fragmentation velocities between 1 and 10m/s. In this work, we always used an intermediate and constant value of fragmentation velocity, 5m/s, motivated by the fact that recent laboratory experiments do not find differences in the fragmentation velocity between silicates and water (Musiolik, Wurm, 2019). Nevertheless, we also investigated the 1 and 10m/s velocities. The higher the value of the fragmentation velocity, the larger can be the Stokes number and the radial drift velocity of the pebbles. This leads to more efficient pebble accretion if the planetary core is formed on a sufficiently small timescale because they need to accrete pebbles before they drift onto the central star.
Lower values of fragmentation velocity result in smaller pebbles that drift slower and in a potentially hindered pebble accretion since the process is size dependent. We would expect that higher fragmentation velocities will increase the heavy element content of early forming planets because the gas is polluted faster by the evaporation of the larger pebble flux.

Disk mass and radius The total disk mass is responsible for the amount of material available for planet formation, high mass disks provide higher dust masses. Pebble and gas accretion rates depend linearly on the available mass, therefore planetary formation is accelerated for larger disks.

The disk radius affects the pebble surface density, larger radii will lead to disks that have a larger supply of pebbles from the outer regions, while smaller radii run out of pebbles faster. Both of these variables will affect the heavy element content of the disk; it will be larger for heavier disks. We chose a relatively massive disk because we wanted to have the opportunity to form giant planets.

Planet's envelope opacity The planet's envelope opacity will affect the envelope contraction phase of the planet, which scales proportionally to the envelope opacity. During this phase, planets migrate fast, thus a low opacity will result in fast gas accretion and earlier transition to the type II migration regime.
We used a fixed value of the opacity consistent with Movshovitz, Podolak (2008), but we also analysed the effect of the different opacities on the planetesimal accretion radius, as shown in Figure 7 in Appendix 4. Higher envelope opacity allows the planet to stay for a longer time in the attached phase, reaching the constant planetesimal accretion radius at a later time.

Planetesimal formation model We proceeded to perform our simulation using the planetesimal formation model proposed in Lenz et al. (2019) based on the idea that planetesimals form if there is a sufficiently high pebble flux in a region. We also tested

another method for planetesimal formation, proposed in Drazkowska, J. et al. (2016) based on the streaming instability scenario, as presented in Appendix 4. With this scenario, we are also able to produce planetesimals that are, however, distributed in a different way in the disk.
We decided to proceed with the planetesimal formation model of Lenz et al. (2019) because it is able to form planetesimals everywhere in the disk and we were mainly interested in maximizing the effect of planetesimal formation in order to study its impact on the final planet composition. We expect the final composition of the planet to be different considering another planetesimal formation scenario but we expect to be able to find the same overall conclusions.

Planetesimal formation efficiency We used a fixed parameter for the planetesimal formation efficiency taken from Lenz et al. (2019), but we also tested different planetesimal formation efficiencies, as shown in Figure 4 and discussed in Appendix 4. Higher formation efficiencies lead to a stronger depletion in the pebble surface density, resulting in a less efficient pebble accretion (possibly hindering it, if they are too high). If the efficiency is too low, instead, we hardly form planetesimal and we fall back into the pebble accretion only scenario. We chose, therefore, a value for the efficiency that was sufficiently large to easily form planetesimals but not too large to prevent pebble accretion, which is clearly supported by observations.

Interior model and atmosphere The assumption made in this work is that during the initial phase of pebble accretion, 90% of the accreted material builds up the core and 10% goes into the primordial atmosphere. Recent studies (Brouwers, M. G., Ormel, C. W., 2020) have, however, shown that the actual solid core accretion uses just 50% of the accreted pebble and that more of them contribute to the atmospheric envelope. This would not change the final heavy element mass of the planet, but it can change the atmospheric constraint. In particular, the exact C/O ratio in case of higher mixing is reduced, but the general trend that planets forming farther away from the central star should harbor a larger C/O that remains intact for both models with and without evaporation of pebbles, as shown in Appendix I of Schneider, Bitsch (2021).

Therefore, the interior model that provides a distribution of the accreted material should be integrated in order to better constrain the C/O ratio and other possible tracers. Another important assumption is that the atmospheric composition reflects the bulk composition.

Chemistry The CHEMCOMP code deals with evaporation lines of the different molecules that we consider to build up the disk, but does not include any chemical reaction. Including grain surface chemistry would change the chemical composition of the dust (Semenov, D. et al., 2010), mainly affecting the micrometer-sized grains rather than the pebbles,

for which evaporation at evaporation fronts will be more significant. The effect of grain surface reactions on the chemical composition thus depends on the growth and drift of the pebbles, requiring a proper model that combines both evaporation and chemical reactions (Krijt et al., 2020).
Booth, Ilee (2019) showed, however, that the pebble drift velocity happens on a shorter timescale compared to the chemical reaction timescale, therefore it is a reasonable assumption not to consider chemical reaction in our model.

The approach used in this work, comparing the outcomes between pebble-dominated and planetesimal-dominated scenarios, combining them with the tracing of the chemical composition of the gas giants, is new in the literature. We proved that, in order to form planets with high heavy element mass content, planetesimal formation needs to be inefficient. Furthermore, the small volatile-to-refractory ratio observed in the planetesimal accretion scenario could be used as a parameter to constrain the planet's formation pathway. These predictions will be testable with large observation programs such as JWST and ARIEL.

Conclusion

The formation pathway of planets is still an open question in the planetary formation field. In particular, there is still a debate whether it is more likely that planets form via pebble or planetesimal accretion. Protoplanetary disk observations confirm the presence of pebbles in the disk, while the presence of asteroids in the Solar System confirms the existence of planetesimals.
Recent observations of giant exoplanets suggest super-stellar C/O ratios in the atmosphere of gas giants, while recent protoplanetary disk observations have revealed super-solar C/H and O/H ratios, as well as high heavy element contents. These observational constraints can be matched by forming a planet in a pebble accretion scenario, with pebbles able to drift inwards and enhance the volatile content of the disk.
This is the state of art scenario in which we conduct our study, the aim of which is to check the effect of planetesimal formation and accretion on the final composition of the planet, possibly answering the question of whether we can use atmospheric composition tracers to constraint the formation pathway of the planet in order to provide a contribution to the debate between pebble and planetesimal accretion scenarios.

To do so we considered three different scenarios:

1. Pebble accretion only scenario.

2. Pebble accretion with planetesimal formation in the disk.

3. Pebble and planetesimal accretion scenario.

We performed a set 1D semi-analytical simulation of different planets, whose planetary seeds were planted at different distances in the disk, for different disk parameters in those three scenarios. In all scenarios, dust grains grow into pebbles and drift inwards, eventually evaporating when they cross the different evaporation lines.
Planets build their core starting from a planetary seed of approximately the dimension of the Moon, planted artificially at some location in the disk. Planetary growth proceeds in different ways according to the considered scenario:

- **Pebble accretion scenario**: The planet accretes the core by solid pebble accretion (90% of the pebbles from the core, 10% a primordial atmosphere) and migrates in

the disk until it reaches pebble isolation mass. At this point it is able to create a pressure bump in the gas, preventing pebbles from accreting and drifting inwards. After reaching pebble isolation mass the planet switches to gas accretion, becoming a gas giant.

- **Pebble accretion and planetesimal formation scenario**: The planet accretes in the same way, but in this scenario planetesimal formation is allowed, meaning that pebbles are removed from the pebble surface density to form planetesimals, therefore the available amount of pebbles that can drift and evaporate is less.

- **Pebble and planetesimal accretion scenario**: In this case, parallel to pebble and gas accretion, the planet can also accrete the planetesimal formed in the disk, at any location and at any point in time. If the planetesimals are accreted during the pebble accretion phase, they are added to the core mass, while if they are accreted after the planet has reached pebble isolation mass, they are accreted into the atmosphere.

Our simulations show that the presence of planetesimal formation in the disk strongly reduces the enhancement of the gas in the disk caused by pebble drift and evaporation, as shown in Figure 3.3 for the water vapor.
The amount of heavy elements available to be accreted on the planet drops dramatically in the case of planetesimal formation, as shown in Figure 3.9, especially for planets forming in disk with high viscosities, that in the pebble accretion only scenarios migrate to the innermost part of the disk, crossing more evaporation fronts and accreting larger amounts of heavy elements from volatile-enriched gas.
In the planetesimal formation scenario, we are not able to reproduce planets with high heavy element content, not even for high viscosities, because a large amount of refractory mass is locked into planetesimals.
The situation does not change much if we include the possibility of accreting those planetesimals. As we can see in Figure 3.12, the same planets in the planetesimal accretion scenario increase their total heavy element mass, but still, end up with a much smaller heavy element mass than in the pebble accretion scenario.
This proves that to reproduce giant planets with high heavy element mass content, we need to have inefficient planetesimal formation.

The final atmospheric C/O ratio is different for the three different scenarios. It generally depends on the mass of the planet and how and when it migrates through the disk. Crossing the different evaporation fronts the C/O ratio increase or decreases, depending on the composition of the enriched gas (crossing the water evaporation front, for example, will make it decrease while crossing the C evaporation front will make it increase again). The three scenarios show different increases/decreases in the C/O ratio. In the pebble accretion only, the changes in the C/O ratio are significant because the gas is heavily enriched, while in the planetesimal formation scenario, the changes in the C/O ratio are

smaller because the gas is less enriched. The planetesimal accretion scenario presents the smallest variation in the C/O ratio of the planet. Taking the water evaporation line as an example, a planet crossing that line should suffer a decrease in the C/O ratio, but it also accretes carbon-rich planetesimals, therefore the changes in the ratio are smaller than in the two previous scenarios.
Due to the big dependence on different parameters, the C/O ratio of the planet alone is not a suited tracer to tell the formation scenarios apart. A remarkable result obtained by our simulation regards the final atmospheric composition of the planets.
The pebble accretion only scenario clearly shows a super-solar C/H and O/H abundance (left panels of Figure 3.8).
The planetesimal formation scenario presents a general depletion of all the elemental species, especially the refractories, due to them being locked inside planetesimals and not accreted on the planet, as well as a small decrease in the volatile to refractory ratio, as shown in the right panels of Figure 3.8.
The planetesimal accretion scenario shows an enhanced refractory abundance with respect to the previous scenarios and a small decrease in the volatile abundance. The volatile to refractory ratio is significantly decreased compared to the other formation scenarios, as shown in Figure 3.11, due to a large amount of refractories being accreted through planetesimals.
Thus, the volatile to refractory ratio may be used in future studies to help constrain the planet formation pathway.

Appendices

Drążkowska, Alibert (2017) method

The method of planetesimal formation presented in Drążkowska, Alibert (2017) is based on the streaming instability scenario.Let us consider a disk in the gas rich phase, where the dust grain size is $1\mu m$ and they are composed by water-ice and silicates. The evolution of solids and water vapor is governed by their interactions with the sub-Keplerian, turbulent gas. The gas disk is a background for the solid evolution and different modelling for the disk can be considered: a power law disk, a non-irradiated disk and an irradiated disk.

The solid surface density evolution is obtained solving the advection-diffusion equation (1.64),

$$\frac{\partial \Sigma_{\rm d}}{\partial t} = \frac{1}{R}\frac{\partial}{\partial R}\left[R\left(\Sigma_{\rm d} v - D_{\rm g}\Sigma_{\rm g}\frac{\partial}{\partial R}\left(\frac{\Sigma_{\rm d}}{\Sigma_{\rm g}}\right)\right)\right], \tag{1}$$

where v is the mass-weighted average radial velocity of solids, which encompasses information about their size. To calculate this velocity both radial drift, due to the interaction with sub-Keplerian gas, and gas accretion flow are taken into account:

$$v = \frac{2\eta v_{\rm K}{\rm St} + v_{\rm g}(1+\varepsilon)}{{\rm St}^2 + (1+\varepsilon)^2}, \tag{2}$$

with the maximum radial drift speed $\eta v_{\rm K}$ driven by the pressure gradient, the dust-to-gas ratio ε. To model dust aggregate size we use the two-population algorithm proposed in Birnstiel, T. et al. (2012), in which the dust size distribution is set in every cell based on the dominating process: Either coagulation-fragmentation equilibrium or radial drift.

The most important parameter that describes the dust-gas interaction is the Stokes number (c.f. Subsection 1.1.2), which depends on the grain size a and for the Epstein drag regime is given by:

$${\rm St} = \frac{\pi}{2}\frac{a}{\rho\Sigma_{\rm g}} \tag{3}$$

with the internal density aggregate ρ, computed based on the grain composition,

$$\rho = (m_{\rm sil} + m_{\rm ice})\left(\frac{m_{\rm sil}}{\rho_{\rm sil}}\frac{m_{\rm ice}}{\rho_{\rm ice}}\right)^{-1}, \tag{4}$$

where $m_{\rm sil}$ and $m_{\rm ice}$ are the masses of silicate and ice respectively, contained within the aggregate.

The evolution of solids is dominated by the radial drift and by the fragmentation that prevents the solid growth. The maximum aggregate size that can be obtained before fragmentation kicks in is stronger dependent on the fragmentation threshold velocity v_f:

$$a_{\text{frag}} \propto \frac{v_f^2}{\alpha_t c_s^2}, \tag{5}$$

where α_t is the midplane turbulence strength parameter[1]. Laboratory experiments show that on average the fragmentation threshold velocity is ~ 1 m/s for silicates, although it may be increased for icy aggregates because their surface energies are about 10 times higher, meaning that there can be up to 10 m/s.

Evaporation and re-condensation are also taken into account. The ice travels through the disk into aggregates (thus faster than the water vapour), while the water vapour's evolution is traced following the transport equation 1. Dust grains at the same orbital distance are assumed to have the same composition, meaning that the water is added and removed from the dust with constant dm/m during evaporation and re-condensation. This is consistent with the fact that the fragmentation/coagulation that should redistribute the ice content happens on a shorter timescale than the radial drift.

At every time step the equilibrium pressure is computed by means of the Clausius-Clapeyron equation:

$$P_{\text{eq}} = P_{\text{eq},0} \exp\left(\frac{-A}{T}\right), \tag{6}$$

with the constants for the inital equilibirum pressure and $P_{\text{eq},0} = 1.14 \cdot 10^{13}\text{g/cms}^2$, $A = 6062$ K taken from Lichtenegger, Komle (1991). At this point, the equilibrium pressure is compared to the water vapour pressure:

$$P_{\text{vap}} = \frac{\Sigma_{\text{vap}}}{\sqrt{2\pi} H_g} \frac{k_B T}{\mu_{\text{H}_2\text{O}}}, \tag{7}$$

with the water vapor surface density Σ_{vap} and gas scale height H_g. If $P_{\text{vap}} < P_{\text{eq}}$ evaporation takes place, and the ice surface density is decreased, and if $P_{\text{vap}} > P_{\text{eq}}$ then the water vapor condenses onto grains (until the vapor pressure reaches equilibrium pressure) and the surface density of ice is increased. The surface density added to the ice is subsequently removed from the vapor supply. As we assume a continuous size distribution for every radial cell[2] in our model, we can forego making a distinction between dust and pebbles. Furthermore, we avoid modelling every size bin by taking the surface-weighted average size $\bar{a}$. This can be done as vapor condensation happens mostly for the smallest grains with the most surface area, in contrast to micro-sized ones, where it takes some time as they have smaller surface areas.

[1]It differs from the α_ν efficiency in angular momentum transport via turbulence viscosity, because in contemporary theories the angular momentum transport is not necessarily driven by turbulence anymore.

[2]The cells are set at coagulation-fragmentation equilibrium around the snowline

The model The model used in Drążkowska, Alibert (2017) is a one-dimensional model, meaning that it cannot resolve streaming instability that would locally condense pebbles into denser filaments that would then collapse to form planetesimals. The approach is, instead, to check at every time-step in every radial bin if the midplane surface density exceeds unity, meaning the condition to form planetesimals translates into:

$$\frac{\rho_{\mathrm{d}}(\mathrm{St} > 10^{-2})}{\rho_{\mathrm{g}}} > 1 \tag{8}$$

where we consider only the dust grains that have $St > 10^{-2}$ because they are the only ones that can participate in the planetesimal formation via streaming instability. During the planetesimal formation, part of the surface density of the pebbles is transferred into planetesimals:

$$\dot{\Sigma_{\mathrm{pla}}} = \zeta \cdot \Sigma_{\mathrm{d}}(\mathrm{St} > 10^{-2}) \cdot \Omega_{\mathrm{K}} \tag{9}$$

with $\zeta = 10^{-3}$ efficiency derived by the numerical methods presented in Simon et al. (2016).

The assumptions The model is based on the following assumptions:

- We consider one-dimensional, locally isothermal disk models and focus on the evolution of their midplane, where pebbles and planetesimals reside. Thus, we only consider the radial snow line and neglect effects associated with the atmospheric snow line.
- Grain sizes are set by either the coagulation-fragmentation or the growth-drift equilibrium. We do not consider the impact of evaporation and condensation on aggregate sizes. This is equivalent with assuming that the ice added during recondensation is quickly redistributed by coagulation and fragmentation. Any aggregates that would increase their size over the maximum are immediately fragmented or removed by radial.
- During one time-step and at a given orbital distance, all the aggregates are either in evaporation or in condensation mode. We do not consider grain curvature effects that could switch between those effects from grain to grain drift.
- Porosity is neglected, and grains are treated as spheres.
- We assume that the vertical structure of solids is always in equilibrium between settling and turbulent mixing, leading to a dust scale height given by:

  $$H_{\mathrm{d}} = H_{\mathrm{g}} \sqrt{\frac{\alpha_{\mathrm{t}}}{\alpha_{\mathrm{t}} + \mathrm{St}}} \tag{10}$$

  and that the water vapor is instantly mixed up to gas scale height H_{g}, even though it is released by pebbles with $H_{\mathrm{d}} < H_{\mathrm{g}}$.

- We assume that minimum pebble size necessary to trigger planetesimal formation via streaming instability corresponds to St $< 10^{-2}$, following Drazkowska, J. et al. (2016) and Bai, Stone (2010).

- The structure of our gas disks is independent on solids evolution. This looses validity for high dust-to-gas ratio, when $\Sigma_{\mathrm{d}} \approx \Sigma_{\mathrm{g}}$, which happens when the pile-up forms in our models.

Results Planetesimal formation via streaming instability simulated in Drążkowska, Alibert (2017) shows that the highest solid-to-gas ratio is obtained directly outside the snow line. Generally, the radial drift of the dust enhances the dust-to-gas ratio in the innermost part of the disk. The maximum size of the dust grains depends on the fragmentation, leading to a surface solid density profile of $R^{-1.5}$ (Birnstiel, T. et al., 2012). The gas surface density is shallow, thus in principle planetesimal formation via streaming instability should already be possible in the innermost parts of the disk at a timescale of $\approx 10^5$ years.

We know that refractory aggregates fragment at lower impact velocities, meaning they form smaller grains compared to icy aggregates. As the Stokes number of an aggregate decreases, also its drift velocity decreases causing the dust to be retained in the inner disk, producing a sort of "traffic jam" effect. Dry dust inside the snow line are coupled pretty good with the gas, thus undergo significant diffusion and do not pile up as, instead, happens to icy aggregates outside the snowline. Indeed, the outwards diffusion of water vapor causes an increase in the surface density of icy pebbles outside the snowline (as the vapor recondenses crossing it), triggering streaming instability and thus planetesimal formation.

In summary, the snowline pile-up is facilitated by different processes, as also shown in figure 1:

1. The presence of ice increases the solid density outside the snow line.

2. Aggregates that incorporate water ice coagulate more efficiently, creating bigger size solids that are able to drift inwards faster. Once they cross the snowline, volatile evaporate, leaving behind the embedded refractory material, that does not drift rapidly, causing a "traffic jam" and an increase of dust concentration in the inner disk.

3. Water vapor diffuses outwards and recondenses after crossing the snowline, causing an increase in the solid abundance just outside the snowline, contributing to the pile-up of icy pebbles.

Planetesimals formed using this model start to appear at the snowline after around $2 \cdot 10^5$ years, and their formation lasts another $2 \cdot 10^5$ years. During planetesimal formation, the snowline shifts inwards as the disk cools down and the planetesimal formation region

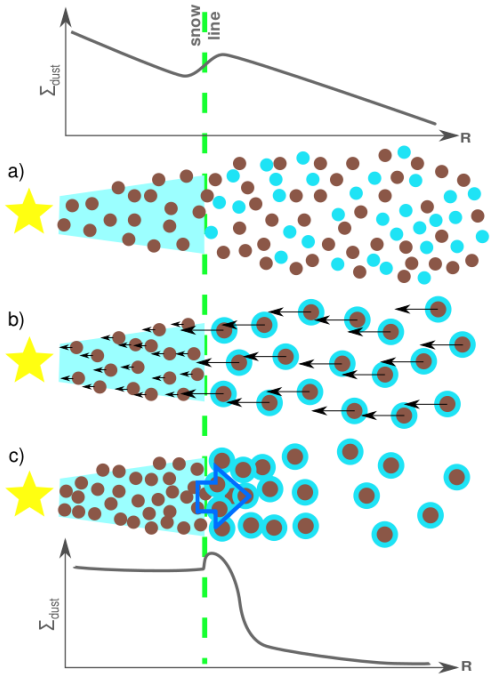

Figure 1: This figure from Drążkowska, Alibert (2017) shows the processes facilitating the snowline pile-up: a) The presence of ice increases the solid density outside the snowline, b) The icy aggregates coagulate more efficiently thus grow lareger in size and drift faster inwards, once they cross the snowline water evaporates and refractory material drifts slower, causing a traffic jam effect, c) The outward gas diffusion increases the solid density outside the snowline, contributing to the pebble pile-up.

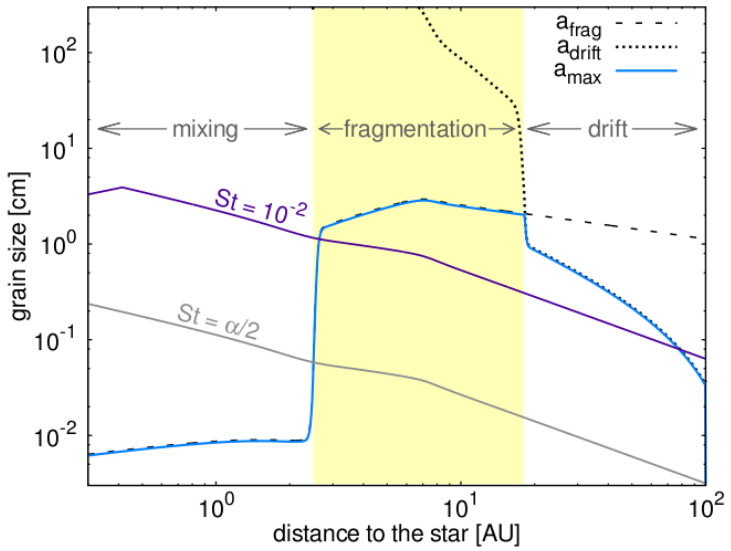

Figure 2: This plot shows the maximum pebble size ($a_{\max}$, blue line) as a function of the radial distance after $2 \cdot 10^5$ years of evolution, from Drążkowska, Alibert (2017). We can see that in the outer part of the disk, the size is limited by the radial drift (dotted line), while in the innermost parts is driven by the fragmentation (dashed line). The aggregates that are large enough to participate in planetesimal formation via streaming instability are the one with $\mathrm{St} > 10^{-2}$, marked by the purple solid line, that are present only outside of the snow line.

(which inner edge is the snowline) starts to spread outwards because of the collective drift effect. After 10^4 years the inward pebble flux is no longer sufficient to fuel the snowline pile-up and the solid surface density drops, terminating the planetesimal formation phase.

Figure 2 shows the pebble size obtained by the simulations: we clearly see that the inner disk is dominated by fragmentation driven by turbulence and the outer disk is gradually depleted by the radial drift before the particles have time to grow to the fragmentation limit. The presence of a fragmentation threshold (5) is responsible for the rapid change of the pebble size around the snowline: icy pebbles outside grow to cm size pebbles ($\mathrm{St} > 10^{-2}$), while the dry pebbles inside remain of sub-mm size with $\mathrm{St} < \alpha_\nu$, meaning that they are well coupled with the gas in a mixed regime, drift inside much slower than the icy ones and therefore enhance the dust-to-gas ratio inside the snowline retention of icy pebble pile-up outside of the snowline thanks to the outward diffusion of small grains. By performing the simulations switching off the recondensation and switching off the traffic jam effect[3] we clearly see that the dominant effect to create the pile-up overdensity is the difference between the sticking properties of icy and dry pebble (so, the

[3]This is achieved setting the same fragmentation velocity for both icy and dry pebbles

traffic jam effect).

Different simulations with different gas parameters, initial dust-to-gas ratio, turbulence level and disk dimension show that it is easier to trigger planetesimal formation when the snowline is closer to the central star. The main constraints of the planetesimal formation zone's inner edge come from the disk model itself and its metallicity:

1. The disk model determines the flux of pebbles reaching the snow line if the abundance of solids is increased. This means that more water vapor is delivered, which, in turn, increases the vapor pressure and thus the location of the snow line

2. The resulting metallicity directly determines the width of the planetesimal annulus by broadening it via the collective drift effect, caused by the higher incoming pebble flux. At the gas-solid ratio peak the radial drift slows down and the peak becomes wider the more pebbles are delivered.

We stress that the collective drift effect is a critical compo- nent of our model without which obtaining the significant pile- up and planetesimal formation is nearly impossible.

Testing the impact of turbulence parameter α_t shows that lower turbulence facilitates planetesimal formation.The lower the turbulence strength, the wider and more massive the resulting planetesimal annulus becomes, while no planetesimal formation is possible for turbulence values that are significantly higher than 10^{-3}. This is due to the fact that higher turbulence reduces the maximum size to which pebble can grow, as shown in equation (5) and decreases their settling possibility (10).

Also the dimension of the disk can impact planetesimal formation, although the difference is much less pronounced than in the varying turbulence case: generally we observe that the larger the disk, the more massive and more extended the planetesimals annulus becomes. This is because larger disks provide long lasting supply of pebbles, as their growth takes longer at larger orbital distances. In other words, increasing the disk size (while keeping its mass unchanged) shifts more solid mass to its outer regions, and this reservoir can be then used to form more planetesimals.

Planetesimal formation in our simulations

We tested the Drążkowska, Alibert (2017) method for planetesimal formation in our simulations. Figure 3 shows the comparison between the two planetesimal formation methods: Drążkowska, Alibert (2017) (top row) and Lenz et al. (2019) (middle row). We can clearly notice that the Drążkowska, Alibert (2017) provides a suitable planetesimal surface density characterized by the same spikes at the evaporation lines, but it is more efficient in forming planetesimals in the outer region of the disk. Lenz et al. (2019) method, on the contrary, provides a broader planetesimal distribution that covers the entire disk, thus maximizing the planetesimal impact on the planet's growth.

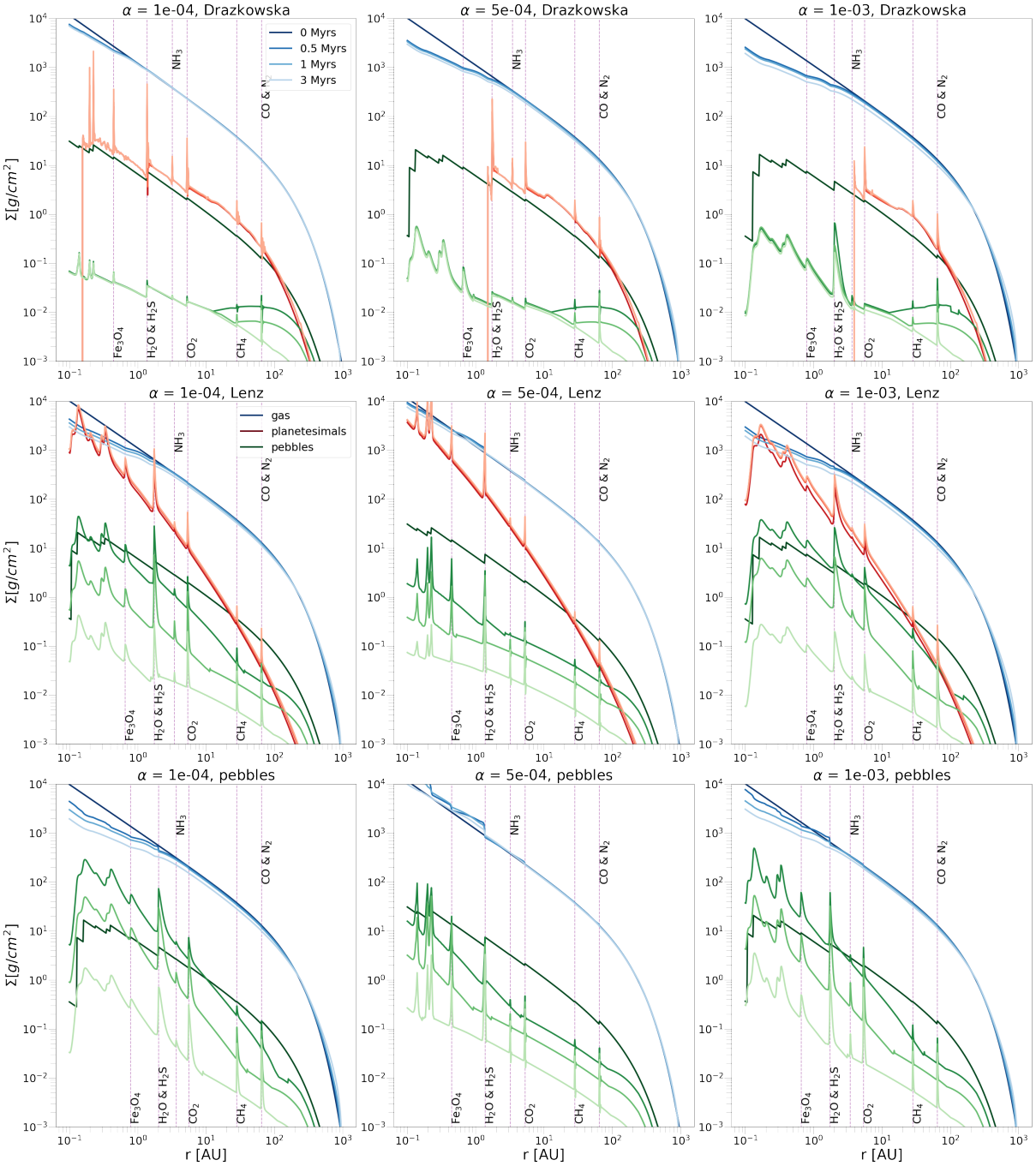

Figure 3: Gas, pebble and planetesimal surface density comparison for the two different plantesimal formation scenarios, pebble accretion only, for three disk viscosities. Top row shows the Drążkowska, Alibert (2017) method, middle row the Lenz et al. (2019) method and bottom row the pebble only scenario. Although the Drążkowska, Alibert (2017) method is able to provide a suitable planetesimal surface density for our simulations, we clearly see that the method is more efficient in the outer part of the disk, compared to the Lenz et al. (2019) method that efficiently forms plantesimals everywhere in the disk. For this reason, we decided to proceed with the Lenz et al. (2019) method, to study the maximum impact of planetesimal formation on planet formation.

Planetesimal formation efficiencies

In this work we also tested different planetesimal formation efficiencies to check whether they would lead to substantially different results.

Figure 4 shows the surface density of pebbles, planetesimals and gas as a function of distance from the central star for different planetesimal efficiencies (respectively $\varepsilon = 0$, pebble only case top panels, $\varepsilon = 0.1$ mid panels, $\varepsilon = 0.01$ bottom rows). As already underlined in Lenz et al. (2019), we can observe the typical spikes around the water (and in our case also other elements) evaporation fronts where the pebbles and the planetesimals pile up. Higher planetesimal formation efficiencies (bottom row) result in s faster decrease of the pebble surface density, causing the pebble accretion to be more inefficient (possibly also hindering it, if the efficiency is too high). We chose a fixed value of planetesimal formation efficiency of $\varepsilon = 0.1$ following Lenz et al. (2019), since in this case we are still able to have an efficicent pebble accretion and at the same time form planetesimal faster. Figure 5 shows the water content in the disk for the three different efficiencies. We clearly notice that a higher plantesimal formation efficiency leads to a bigger depletion in the water content of the disk, because material is more efficiently and faster locked into planetesimals, preventing it to drift and enrich the gas in the disk.

Figure 6 shows the heavy element mass of the three planets as a function of the total mass in the different viscosities and planetesimal formation efficiencies scenarios. In all cases we can notice that the correlation is at first linear, due to the fact that in the first phase of solid accretion the planet accrets only heavy elements, while when it switches to gas accretion phase, the relation changes. Higher plantesimal formation efficiencies lead to smaller heavy element mass accretion in the gas accretion phase, because the gas in less enriched in heavy elements.

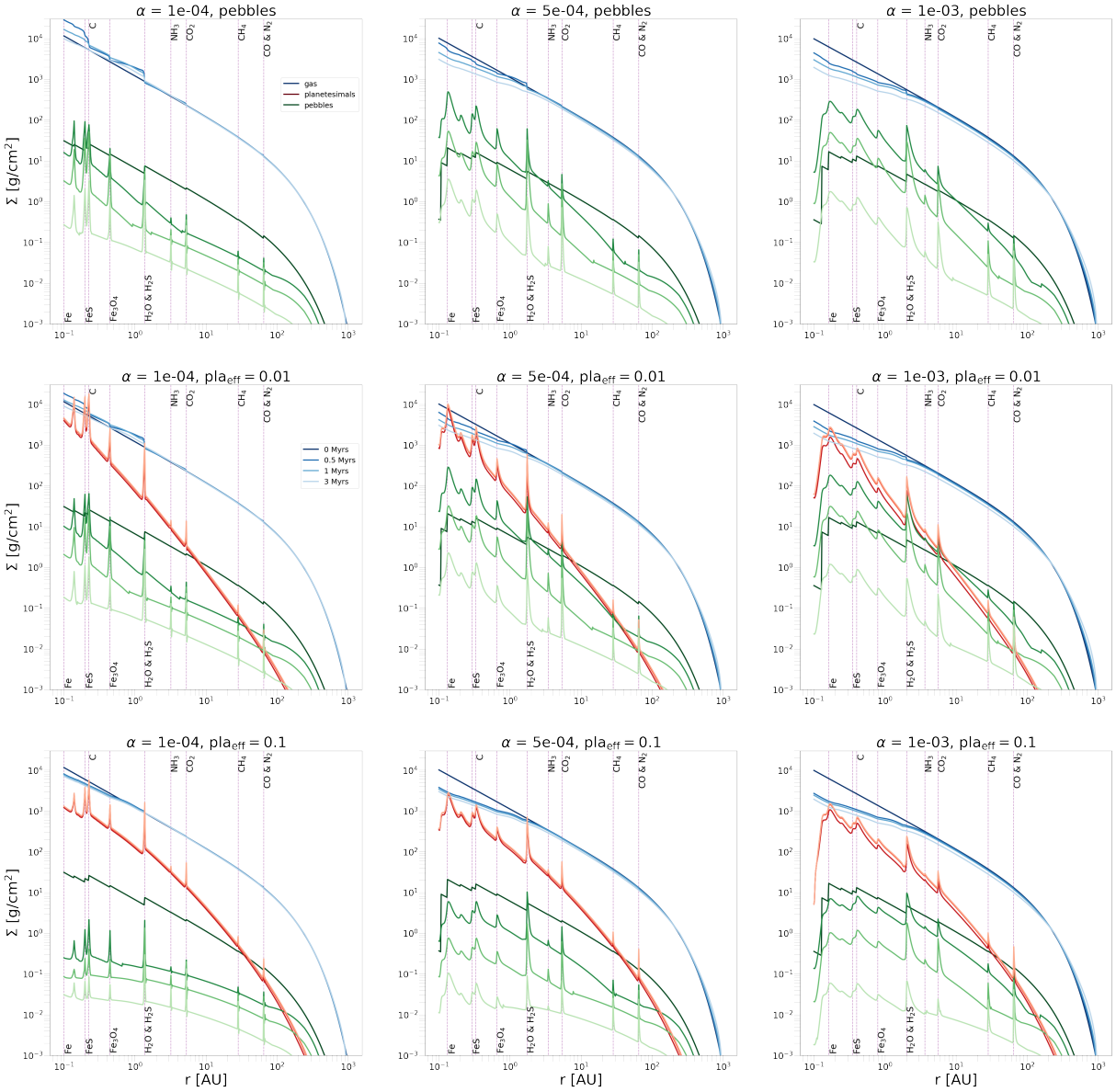

Figure 4: This figure shows the surface density of pebble planetesimal and gas as a function of distance from the central star if we consider different planetesimal formation efficiency (top row $\varepsilon = 0$, mid row $\varepsilon = 0.1$, bottom row $\varepsilon = 0.01$) for the three different disk viscosities. We see that increasing the efficiency we decrease the pebble surface density faster with time, because we form planetesimal faster.

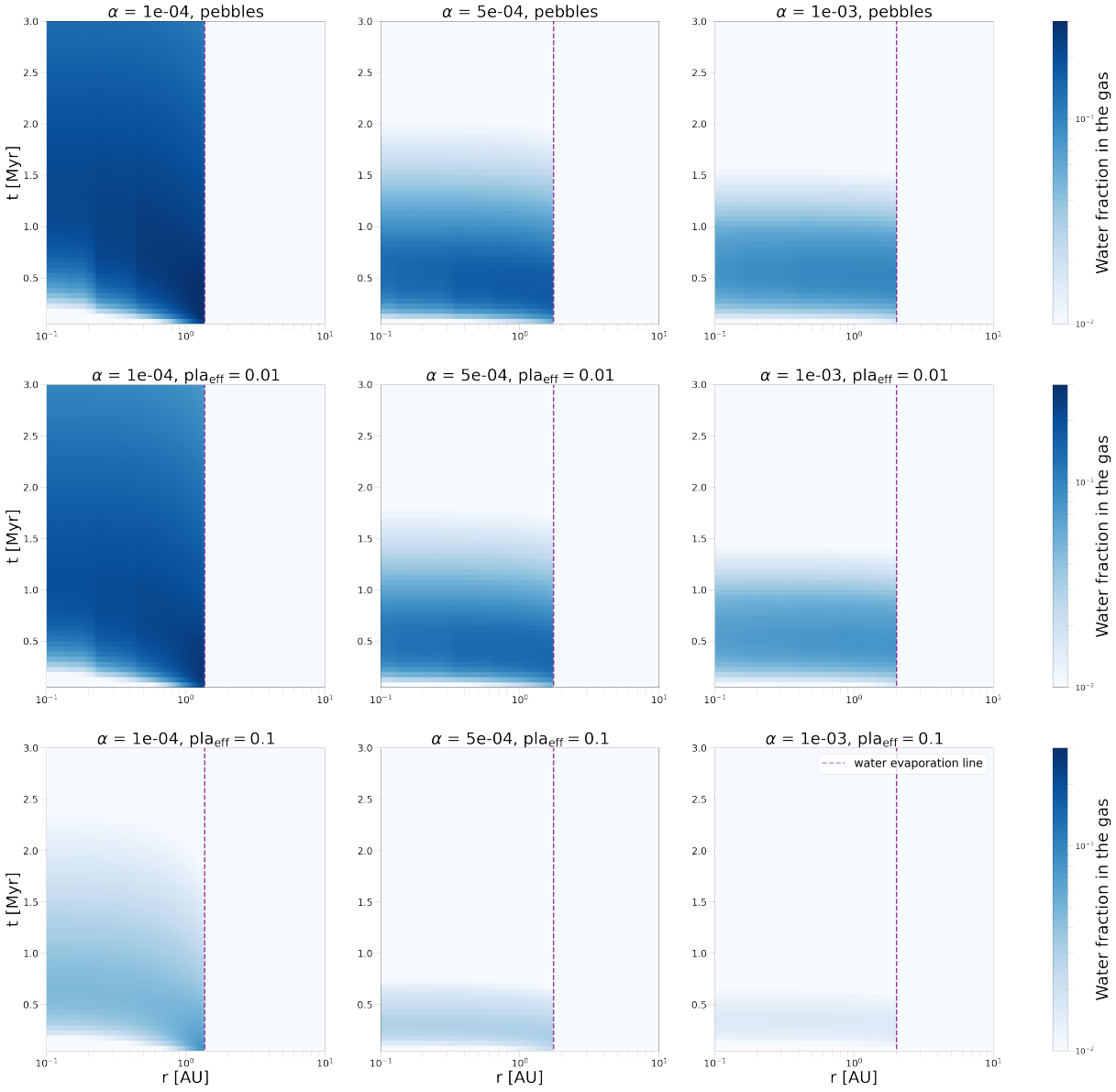

Figure 5: This figure shows the water content of the disk for the different planetesimal formation efficiencies (top row $\varepsilon = 0$, mid row $\varepsilon = 0.1$, bottom row $\varepsilon = 0.01$). We clearly notice that the higher the planetesimal formation efficiency, the more depleted in water content is the disk.

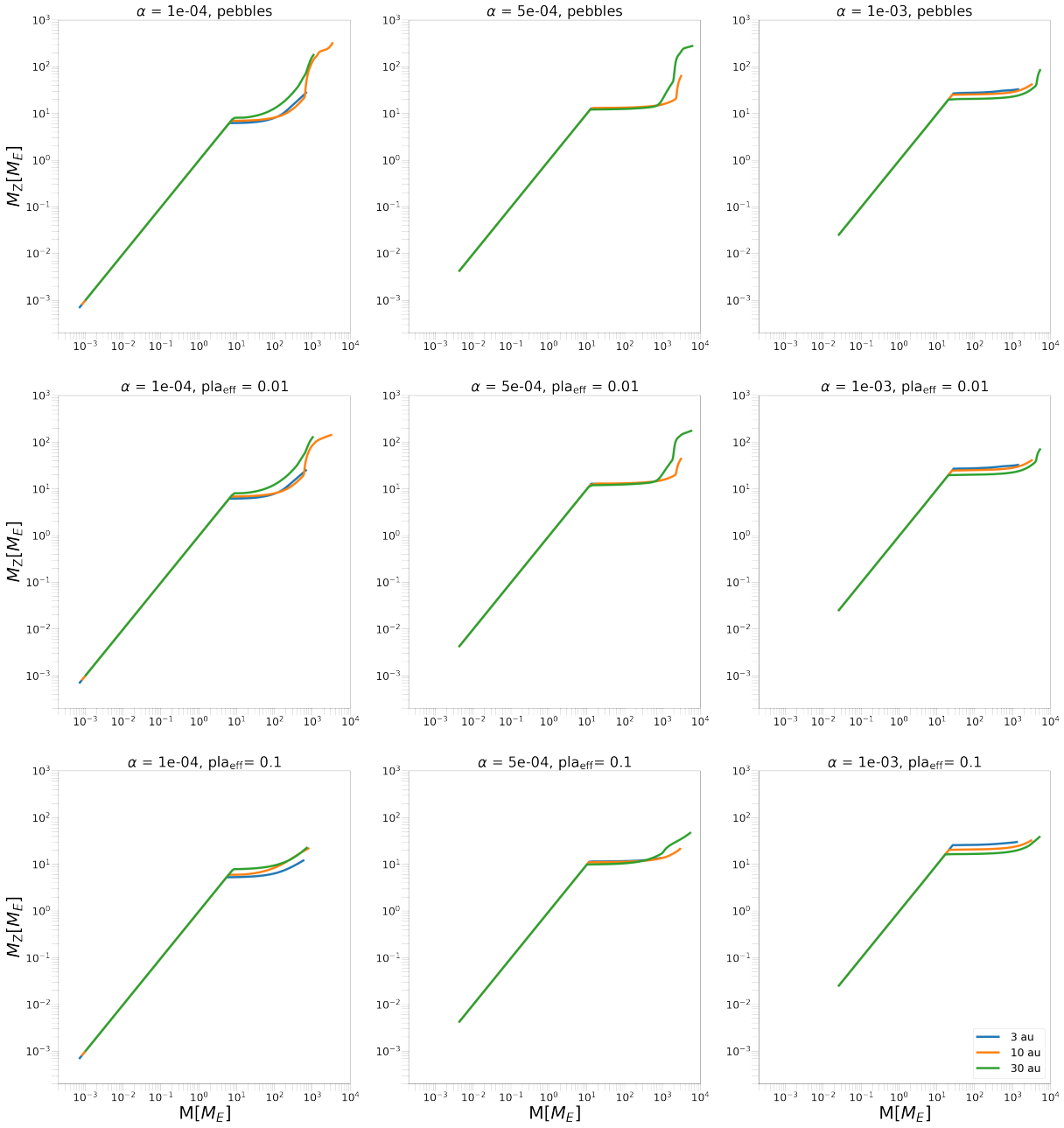

Figure 6: This figure shows the heavy element mass of the planet as a function of the total mass for the three planets, viscosities and the different planetesimal formation efficiencies (top row $\varepsilon = 0$, mid row $\varepsilon = 0.1$, bottom row $\varepsilon = 0.01$). the relation is at first linear because in the first phase of solid accretion the planets accretes only heavy elements. When it switches to gas accretion, the planet starts to accrete volatiles and the mass relation changes. Higher plantesimal formation efficiencies lead to smaller heavy element mass accretion in the gas accretion phase, because the gas in less enriched in heavy elements.

Planetesimal accretion radius

Figure 7 shows the planetesimal accretion radius for different planetesimal sizes ($R_{\rm pla} = 1 - 50$ km) and for different disk opacities ($\kappa = 0.05 - 0.5$). It shows the same trend as in Figure 1.9 from Valletta, Helled (2021), i.e. a steeply increasing accretion radius at early times, when the planet is still in the attached phase and the prescription for the capture radius is given by equation (1.100), then a fast collapse and a flat profile, given by equation (1.102), when the crossover mass[4] is reached and the planet switched to the detached phase. We observe a net distinction between the two opacities values ($\kappa = 0.05$, red and gold, $\kappa = 0.5$, navy and lightseagreen): bigger opacities (navy and lightseagreen) allow the planet to stay longer in the attached phase because it is more difficult for the planet to open a gap in the disk, while lower opacity planets reach the detached phase way faster. This happens because for higher opacities the cooling of the envelope is less efficient, and the gas accretion is directly related to the cooling.

The capture radius poorly depends on the planetesimal size during the attached phase (as proved by the small difference between the two planetesimal radii in Figure 7), while it is by definition independent during the detached phase, as observed in Valletta, Helled (2021).

[4]We recall the crossover mass is defined when the planet's Helium and Hydrogen mass and the heavy element mass are equal.

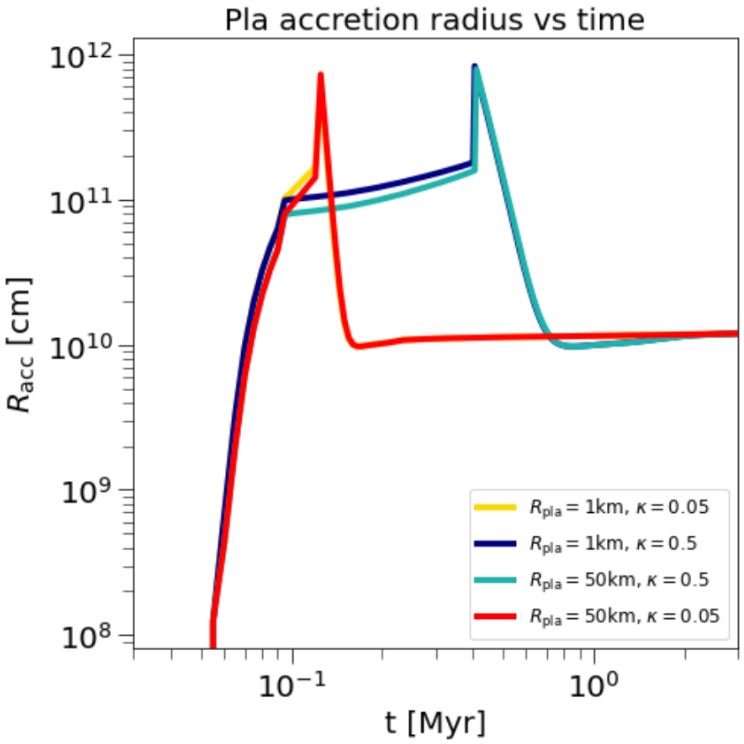

Figure 7: Capture radius as a function of time for $R_{\rm pla} = 1$ km, $\kappa = 0.05$ (gold), $R_{\rm pla} = 1$ km, $\kappa = 0.5$ (navy), $R_{\rm pla} = 50$ km, $\kappa = 0.05$ (red) and $R_{\rm pla} = 50$ km, $\kappa = 0.5$ (lightseagreen). Higher envelope opacities (navy and lightseagreen lines) lead to planet that stay longer in the attached phase. We observe a weak dependence of the accretion radius on the planetesimal size in the attached phase and independence (by definition) in the detached phase. All the results are in good accordance with Valletta, Helled (2021).

Bibliography

Armitage Philip J. Astrophysics of Planet Formation. 2013.

Bai Xue-Ning, Stone James M. Dynamics of Solids in the Midplane of Protoplanetary Disks: Implications for Planetesimal Formation // . X 2010. 722, 2. 1437–1459.

Benítez-Llambay Pablo, Masset Frédéric, Koenigsberger Gloria, Szulágyi Judit. Planet heating prevents inward migration of planetary cores // Nature. apr 2015. 520, 7545. 63–65.

Bergez-Casalou, C. , Bitsch, B. , Pierens, A. , Crida, A. , Raymond, S. N. . Influence of planetary gas accretion on the shape and depth of gaps in protoplanetary discs // A&A. 2020. 643. A133.

Birnstiel, T. , Dullemond, C. P. , Brauer, F. . Dust retention in protoplanetary disks // A&A. 2009. 503, 1. L5–L8.

Birnstiel, T. , Klahr, H. , Ercolano, B. . A simple model for the evolution of the dust population in protoplanetary disks // A&A. 2012. 539. A148.

Birnstiel T., Dullemond C. P., Brauer F. Gas- and dust evolution in protoplanetary disks // . IV 2010. 513. A79.

Bitsch, Bertram , Battistini, Chiara . Influence of sub- and super-solar metallicities on the composition of solid planetary building blocks // A&A. 2020. 633. A10.

Bitsch, Bertram , Lambrechts, Michiel , Johansen, Anders . The growth of planets by pebble accretion in evolving protoplanetary discs // A&A. 2015. 582. A112.

Bitsch, Bertram , Morbidelli, Alessandro , Johansen, Anders , Lega, Elena , Lambrechts, Michiel , Crida, Aurélien . Pebble-isolation mass: Scaling law and implications for the formation of super-Earths and gas giants // A&A. 2018. 612. A30.

Blum J., Wurm G. The growth mechanisms of macroscopic bodies in protoplanetary disks. // . IX 2008. 46. 21–56.

Booth R A, Ilee J D. Planet-forming material in a protoplanetary disc: the interplay between chemical evolution and pebble drift // Monthly Notices of the Royal Astronomical Society. 05 2019. 487, 3. 3998–4011.

Boss A. P. Giant planet formation by gravitational instability. // Science. I 1997. 276. 1836–1839.

Brouwers, M. G. , Ormel, C. W. . How planets grow by pebble accretion - II. Analytical calculations on the evolution of polluted envelopes // A&A. 2020. 634. A15.

Carrera, Daniel , Johansen, Anders , Davies, Melvyn B. . How to form planetesimals from mm-sized chondrules and chondrule aggregates // A&A. 2015. 579. A43.

Carry B. Density of asteroids // Planetary and Space Science. 2012. 73, 1. 98–118. Solar System science before and after Gaia.

Chrenko, O. , Broz, M. , Lambrechts, M. . Eccentricity excitation and merging of planetary embryos heated by pebble accretion // A&A. 2017. 606. A114.

Crida A., Bitsch B. Runaway gas accretion and gap opening versus type I migration // . III 2017. 285. 145–154.

Crida A., Morbidelli A. Cavity opening by a giant planet in a protoplanetary disc and effects on planetary migration // Monthly Notices of the Royal Astronomical Society. 04 2007. 377, 3. 1324–1336.

Crida A., Morbidelli A., Masset F. On the width and shape of gaps in protoplanetary disks // Icarus. Apr 2006. 181, 2. 587–604.

Dipierro G., Lodato G., Price D., Laibe G., Pinilla P., Ragusa F. Substructures in protoplanetary discs-dust and gas dynamics. II 2016.

Drazkowska, J. , Alibert, Y. , Moore, B. . Close-in planetesimal formation by pile-up of drifting pebbles // A&A. 2016. 594. A105.

Drążkowska J., Alibert Y. Planetesimal formation starts at the snow line // . XII 2017. 608. A92.

Eistrup, Christian , Walsh, Catherine , van Dishoeck, Ewine F. . Setting the volatile composition of (exo)planet-building material - Does chemical evolution in disk midplanes matter? // A&A. 2016. 595. A83.

Emsenhuber Alexandre, Mordasini Christoph, Burn Remo, Alibert Yann, Benz Willy, Asphaug Erik. The New Generation Planetary Population Synthesis (NGPPS). I. Bern global model of planet formation and evolution, model tests, and emerging planetary systems // . XII 2021. 656. A69.

Fromang S., Papaloizou J. Dust settling in local simulations of turbulent protoplanetary disks // Astronomy and Astrophysics. Jun 2006. 452, 3. 751–762.

Gundlach B., Blum J. The Stickiness of Micrometer-sized Water-ice Particles // . I 2015. 798, 1. 34.

Güttler, C. , Blum, J. , Zsom, A. , Ormel, C. W. , Dullemond, C. P. . The outcome of protoplanetary dust growth: pebbles, boulders, or planetesimals?* - I. Mapping the zoo of laboratory collision experiments // A&A. 2010. 513. A56.

Henning Thomas, Semenov Dmitry. Chemistry in Protoplanetary Disks // Chemical Reviews. Dec 2013. 113, 12. 9016–9042.

Ikoma Masahiro, Nakazawa Kiyoshi, Emori Hiroyuki. Formation of Giant Planets: Dependences on Core Accretion Rate and Grain Opacity // . VII 2000. 537, 2. 1013–1025.

Inaba, S. , Ikoma, M. . Enhanced collisional growth of a protoplanet that has an atmosphere // A&A. 2003. 410, 2. 711–723.

Johansen Anders, Bitsch Bertram. Exploring the conditions for forming cold gas giants through planetesimal accretion // . XI 2019. 631. A70.

Johansen Anders, Lacerda Pedro. Prograde rotation of protoplanets by accretion of pebbles in a gaseous environment // Monthly Notices of the Royal Astronomical Society. 04 2010. 404, 1. 475–485.

Johansen Anders, Lambrechts Michiel. Forming Planets via Pebble Accretion // Annual Review of Earth and Planetary Sciences. 2017. 45, 1. 359–387.

Krijt Sebastiaan, Bosman Arthur D, Zhang Ke, Schwarz Kamber R, Ciesla Fred J, Bergin Edwin A. CO Depletion in Protoplanetary Disks: A Unified Picture Combining Physical Sequestration and Chemical Processing // The Astrophysical Journal. 2020. 899, 2. 134.

Lambrechts, M. , Johansen, A. . Rapid growth of gas-giant cores by pebble accretion // A&A. 2012. 544. A32.

Lambrechts, M. , Johansen, A. , Morbidelli, A. . Separating gas-giant and ice-giant planets by halting pebble accretion // A&A. 2014. 572. A35.

Lega E., Crida A., Bitsch B., Morbidelli A. Migration of Earth-sized planets in 3D radiative discs // Monthly Notices of the Royal Astronomical Society. 03 2014. 440, 1. 683–695.

Lenz Christian T., Klahr Hubert, Birnstiel Tilman. Planetesimal Population Synthesis: Pebble Flux-regulated Planetesimal Formation // . III 2019. 874, 1. 36.

Lichtenegger H. I. M., Komle N. I. Heating and evaporation of Icy particles in the vicinity of comets // . IV 1991. 90, 2. 319–325.

Lin D. N. C., Papaloizou J. Tidal torques on accretion discs in binary systems with extreme mass ratios. // Monthly Notices of the RAS. Mar 1979. 186. 799–812.

Lin D. N. C., Papaloizou J. C. B. On the Tidal Interaction Between Protostellar Disks and Companions // Protostars and Planets III. Jan 1993. 749.

Lodato G. Classical disc physics // New Astronomy Review. VI 2008. 52. 21–41.

Lodato Giuseppe, Scardoni Chiara E., Manara Carlo F., Testi Leonardo. Protoplanetary disc 'isochrones' and the evolution of discs in the $\dot{M}$-M_d plane // . XII 2017. 472, 4. 4700–4706.

Lodders Katharina. Solar System Abundances and Condensation Temperatures of the Elements // The Astrophysical Journal. jul 2003. 591, 2. 1220–1247.

Lynden-Bell D., Pringle J. E. The evolution of viscous discs and the origin of the nebular variables. // Monthly Notices of the RAS. IX 1974. 168. 603–637.

Machida Masahiro N., Kokubo Eiichiro, Inutsuka Shu-ichiro, Matsumoto Tomoaki. Gas accretion onto a protoplanet and formation of a gas giant planet // Monthly Notices of the Royal Astronomical Society. 06 2010. 405, 2. 1227–1243.

Madhusudhan Nikku, Bitsch Bertram, Johansen Anders, Eriksson Linn. Atmospheric signatures of giant exoplanet formation by pebble accretion // Monthly Notices of the Royal Astronomical Society. 05 2017. 469, 4. 4102–4115.

Masset Frédéric S. Coorbital thermal torques on low-mass protoplanets // Monthly Notices of the Royal Astronomical Society. 09 2017. 472, 4. 4204–4219.

Mayor M., Queloz D. A Jupiter-mass companion to a solar-type star // Nature. XI 1995. 378. 355–359.

Mayor Michel. Interview, NobelPrize.org, Nobel Media AB. 2019. [Online; accessed 02-September-2022].

Mizuno Hiroshi. Formation of the Giant Planets // Progress of Theoretical Physics. 08 1980. 64, 2. 544–557.

Mollière P., van Boekel R., Dullemond C., Henning Th., Mordasini C. Model Atmospheres of Irradiated Exoplanets: The Influence of Stellar Parameters, Metallicity, and the C/O Ratio // . XI 2015. 813, 1. 47.

Morbidelli, A. , Nesvorny, D. . Dynamics of pebbles in the vicinity of a growing planetary embryo: hydro-dynamical simulations // A&A. 2012. 546. A18.

Morbidelli A., Lambrechts M., Jacobson S., Bitsch B. The great dichotomy of the Solar System: Small terrestrial embryos and massive giant planet cores // Icarus. sep 2015. 258. 418–429.

Mordasini, C. , Alibert, Y. , Georgy, C. , Dittkrist, K.-M. , Klahr, H. , Henning, T. . Characterization of exoplanets from their formation - II. The planetary mass-radius relationship // A&A. 2012. 547. A112.

Mordasini C., Boekel R. van, Mollière P., Henning Th., Benneke Björn. THE IMPRINT OF EXOPLANET FORMATION HISTORY ON OBSERVABLE PRESENT-DAY SPECTRA OF HOT JUPITERS // The Astrophysical Journal. Nov 2016. 832, 1. 41.

Movshovitz N., Podolak M. The opacity of grains in protoplanetary atmospheres // . III 2008. 194, 1. 368–378.

Musiolik Grzegorz, Wurm Gerhard. Contacts of Water Ice in Protoplanetary Disks—Laboratory Experiments // The Astrophysical Journal. mar 2019. 873, 1. 58.

Ndugu N, Bitsch B, Morbidelli A, Crida A, Jurua E. Probing the impact of varied migration and gas accretion rates for the formation of giant planets in the pebble accretion scenario // Monthly Notices of the Royal Astronomical Society. 11 2020a. 501, 2. 2017–2028.

Ndugu N, Bitsch B, Morbidelli A, Crida A, Jurua E. Probing the impact of varied migration and gas accretion rates for the formation of giant planets in the pebble accretion scenario // Monthly Notices of the Royal Astronomical Society. 11 2020b. 501, 2. 2017–2028.

Notsu Shota, Eistrup Christian, Walsh Catherine, Nomura Hideko. The composition of hot Jupiter atmospheres assembled within chemically evolved protoplanetary discs // Monthly Notices of the Royal Astronomical Society. 09 2020. 499, 2. 2229–2244.

Ormel, C. W. , Cuzzi, J. N. . Closed-form expressions for particle relative velocities induced by turbulence // A&A. 2007. 466, 2. 413–420.

Ormel, C. W. , Klahr, H. H. . The effect of gas drag on the growth of protoplanets - Analytical expressions for the accretion of small bodies in laminar disks // A&A. 2010. 520. A43.

Paardekooper S.-J. Dynamical corotation torques on low-mass planets // Monthly Notices of the Royal Astronomical Society. 09 2014. 444, 3. 2031–2042.

Paardekooper S.-J., Baruteau C., Kley W. A torque formula for non-isothermal Type I planetary migration – II. Effects of diffusion // Monthly Notices of the Royal Astronomical Society. 12 2010. 410, 1. 293–303.

Pinilla, Paola , Lenz, Christian T. , Stammler, Sebastian M. . Growing and trapping pebbles with fragile collisions of particles in protoplanetary disks // A&A. 2021. 645. A70.

Pollack James B., Hubickyj Olenka, Bodenheimer Peter, Lissauer Jack J., Podolak Morris, Greenzweig Yuval. Formation of the Giant Planets by Concurrent Accretion of Solids and Gas // . XI 1996. 124, 1. 62–85.

Pringle J. E. Accretion discs in astrophysics // . I 1981. 19. 137–162.

Queloz Didier. Interview, NobelPrize.org, Nobel Media AB. 2019. [Online; accessed 02-September-2022].

Schneider Aaron David, Bitsch Bertram. How drifting and evaporating pebbles shape giant planets. I. Heavy element content and atmospheric C/O // . X 2021. 654. A71.

Semenov, D. , Hersant, F. , Wakelam, V. , Dutrey, A. , Chapillon, E. , Guilloteau, St. , Henning, Th. , Launhardt, R. , Piétu, V. , Schreyer, K. . Chemistry in disks - IV. Benchmarking gas-grain chemical models with surface reactions // A&A. 2010. 522. A42.

Shakura N. I., Sunyaev R. A. Black holes in binary systems. Observational appearance. // . I 1973. 24. 337–355.

Shibata Sho, Ikoma Masahiro. Capture of solids by growing proto-gas giants: effects of gap formation and supply limited growth // Monthly Notices of the Royal Astronomical Society. 06 2019. 487, 4. 4510–4524.

Simon Jacob B., Armitage Philip J., Li Rixin, Youdin Andrew N. THE MASS AND SIZE DISTRIBUTION OF PLANETESIMALS FORMED BY THE STREAMING INSTABILITY. I. THE ROLE OF SELF-GRAVITY // The Astrophysical Journal. may 2016. 822, 1. 55.

Tanaka Hidekazu, Ida Shigeru. Growth of a Migrating Protoplanet // Icarus. 1999. 139, 2. 350–366.

Tazzari, M. , Testi, L. , Ercolano, B. , Natta, A. , Isella, A. , Chandler, C. J. , Pérez, L. M. , Andrews, S. , Wilner, D. J. , Ricci, L. , Henning, T. , Linz, H. , Kwon, W. , Corder, S. A. , Dullemond, C. P. , Carpenter, J. M. , Sargent, A. I. , Mundy, L. , Storm, S. , Calvet, N. , Greaves, J. A. , Lazio, J. , Deller, A. T. . Multiwavelength

analysis for interferometric (sub-)mm observations of protoplanetary disks - Radial constraints on the dust properties and the disk structure // A&A. 2016. 588. A53.

Thorngren Daniel P., Fortney Jonathan J., Murray-Clay Ruth A., Lopez Eric D. The Mass-Metallicity Relation for Giant Planets // . XI 2016. 831, 1. 64.

Valletta Claudio, Helled Ravit. An approximation for the capture radius of gaseous protoplanets // . X 2021. 507, 1. L62–L66.

Wyatt Mark C. Evolution of Debris Disks // Annual Review of Astronomy and Astrophysics. 2008. 46, 1. 339–383.

Acknowledgements

- I could not have undertaken this journey without my supervisor Prof. Francesco Marzari, who supported and enabled me to go abroad and conduct my thesis at another institute outside of Italy.
- Further, I would like to express my deepest appreciation to Prof. Bertram Bitsch as he provided me not only with the opportunity for my thesis in his group at one of the world's most renowned institutes, the Max-Planck Institute of Astronomy, but also for his constant guidance and open-door policy during my stay.
- Many thanks to the Max-Planck Institute of Astrophysics, all its members, and Heidelberg, which have not only provided me with an environment suited for the highest level of research to be conducted during my thesis but also given me many beautiful memories and friendships, which made it a wonderful stay and will be an integral part of my future. Thanks to all the participants of the afternoon table tennis- and coffee-break session; Jonas Syed, Eric Rohr, Olga Borodina, Nico Winkel, Arv Hughes, Alex Dimoff, Riccardo Franceschi, and many others, you all kept me sane during my work hours. Special mention goes to Evert for always providing interesting bets and nicely losing them most of the time, as well as for supporting me.
- I am also thankful to the Università Degli Studi Di Padova for my studies over the past two years.
- Special thanks go out to Molly Wells and Marten Scheuck for proofreading my thesis and many fruitful discussions and for being the best humans of all time[5].
- A special thanks also to my wonderful flatmates, Målin and Marten (and honorary ones, Molly and Passy) for the amazing time we had together and for having always made me feel at home.
- Finally, my heartfelt thanks go to my parents for their constant support throughout my entire life and especially during my studies.

[5] *mic drop*